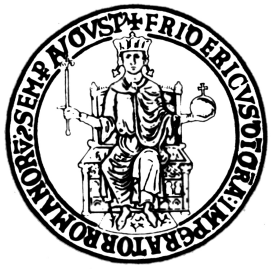

Università degli Studi di Napoli
FEDERICO II

PhD Thesis in
FUNDAMENTAL AND APPLIED PHYSICS
XXI cycle
Coordinator: Pr. Lorenzo Marrucci

Single-Beam 1-D, 2-D And 3-D Patterning Of Liquid Crystal-Polymer Composites With Spatial Light Modulation Based On Computer-Generated Holography

Defended by
Gianluigi Zito

prepared at Physics Department of University Federico II of Naples
Integrated Optics and Nonlinear Optics Teams
defended on January 21, 2009

Advisors:	Pr. Giancarlo Abbate	-	Univ. Federico II of Naples
	Pr. Enrico Santamato	-	Univ. Federico II of Naples
Reviewers:	Pr. Sergio De Nicola	-	CNR - Naples
	Pr. Raffaele Velotta	-	University Federico II of Naples

Thanks to my dear Parents.

The attraction of knowledge would be small if one did not have to overcome so much shame on the way.

The more abstract the truth is that you would teach, the more you have to seduce the senses to it.

People who comprehend a thing to its very depths rarely stay faithful to it for ever. For they have brought its depths into the light of day: and in the depths there is always much that is unpleasant to see.

Half-knowledge is more victorious than whole knowledge: it understands things as being more simple than they are and this renders its opinions more easily intelligible and more convincing.

...F. W. Nitzsche

Contents

Chapter 1

Introduction

Contents

1.1 State of the art of the research

In recent years there has been an increasing interest in the optical properties of complex dielectric materials. A large research effort is dedicated to periodic structures provided of important and interesting properties related to the propagation of light, called Photonic Crystals (PhCs) [Yablonovitch 1987]. Photonic crystals are one of the major recent revolutions in optoelectronics. Analogously to semiconductors, E. Yablonovitch showed how these structures can forbid the propagation of electromagnetic waves because of the existence of a region of frequencies, that is of energies, for which the transport of photons is forbidden in relation of particular direction of propagation and polarization. Such region is known as Photonic Band-Gap (PBG), and the materials furnished of this property are known as photonic band-gap materials. As for instance, a Bragg grating or mirror represents a one-dimensional (1-D) photonic crystal because only a range of light wavelengths for particular direction can propagate through the system. The allowable photonic states are confined and localized only into the regions in which the structure presents defects. The analogy with the physical properties of the electronic transport in semiconductors is complete.

The Yablonovitch proposal was directed to obtain lasing action by means of forbidden energies range in photonic transport. The anomalous reduction of the group velocity close to the edge of the PBG induces a strong enhancement of the spontaneous emission decreasing the threshold of the lasing. In this way it was possible to suppress the spontaneous emission that strongly reduced the efficiency of lasers for telecommunications. This is the first evidence of the huge importance and impact that such kind of materials have for photonic applications. Photonic crystals possess other important properties related to the existence of the PBG, that have been employed to develop photonic devices. So far, lasing has been observed in a lot of systems. Limiting our interest to organic materials, photonic crystals have

been obtained, as for instance, in 1D-patterned liquid crystals-polymers composites doped with particular laser dyes [Matsui 2002] [Strangi 2005]. The possibility to have lasing action has been studied also in complex dielectric materials with a random spatial distribution of the dielectric function. Advances in several research fields have led to a progressive new distinction, of order without periodicity, to properly describe an increasing number of complex systems. Many groups are studying the optical properties of complex dielectric materials with a non-ordered distribution of the refractive index, among which we find also non-periodic dielectric structures, called Quasicrystals (QCs) [Levine 1984], that possess very interesting, yet almost unknown, properties. The classical definition of crystal as periodic lattices provided of translational symmetry has been transferred to the reciprocal space and to the existence of an essential discrete diffraction pattern of light in the far field. Therefore, such kind of materials are crystals like the periodic ones, but with an important generalization related to the symmetries of the structures.

A quasiperiodic system is characterized by the lack of long-range periodic translational order, although the long-range orientational order is preserved. Therefore, quasicrystals exhibit long-range aperiodic order and rotational symmetry not achievable by conventional periodic structures [Steinhardt 1987] [Stadnik 1999]. Since their discovery, quasiperiodic crystals have intrigued scientists from different fields. In the 1998, Chan et al. [Chan 1998], following up the solid-state physics analogy underlying Yablonovich's idea, demonstrated theoretically that two-dimensional (2-D) quasiperiodically-ordered systems could exhibit photonic band-gaps: in this case they are called Photonic Quasicrystals (PhQCs). Like the standard PhCs, photonic QCs may have total (or complete) photonic band-gaps, that is the gap does not depend on the propagation direction of light. This property seems to be related to the presence of sufficiently high statistical symmetry [Zoorob 2000]. Mesoscale quasicrystals, in fact, may possess photonic band-gaps that are more isotropic [Chan 1998] [Zhang 2001] than in conventional photonic crystals and, hence, the PBG becomes more spherical leading to interesting properties of light transmission [Cheng 1999], wave guiding and localization [Jin 1999], increasing the flexibility of these materials for many photonic applications. In fact, the aperiodic translational order gives rise to the existence of many inequivalent defect sites that can be exploited, as for instance, to develop cavity resonators, waveguides, wavelength multiplexer, for the lasing action itself and so on. As for instance, diffraction of optical electromagnetic radiation by periodic structure like Bragg gratings is of increasing importance in an expanding variety of engineering applications in the fields of acousto-optics, integrated optics, holography, optical data processing and spectral analysis [Gaylord 1985] [Eldada 2004]. Furthermore, there has been much research activity pertaining to photonic band-gap (PBG) materials which have potential applications in quantum electronic devices [Agi 1994] [Sigalas 1997], distributed-feedback mirror, microwave antennae substrate, with optical properties which can be exploited to control and guide the propagation of light [Mekis 1996] [Zhang 1999a] [Zhang 1999b]. Sizable spectral gap can exist in a 2-D quasi-periodic arrangement of dielectrics like Penrose lattices [Chan 1998] [Zoorob 2000] [Zhang 2001]. Full

photonic band-gaps are possible in non-crystalline planar 2-D structures with an attractive feature, the high degree of symmetry achievable in quasi-crystal patterns results in a relaxation of the high index contrast required to open up the band gap, leading also to interesting properties of light transmission, wave guiding and localization. These properties make photonic quasicrystals promising in a range of optical devices.

The fabrication techniques of photonic crystals and Bragg gratings lend themselves quite well to the production of 2-D and 3-D structures due to the periodicity that exists in the patterns. Quasicrystal patterns are more difficult to produce since they possess N-fold symmetry about a central feature. In a similar way, complex non periodic spatial modulations in diffraction gratings are difficult to induce. In this direction, holographic fabrication techniques play an important role leading to the possibility of functionalizing dielectric structure in a wide variety. The record of the holographic interference pattern usually takes the form of the spatial modulation of the absorption constant or the refractive index of the medium, or both. Photo-polymer materials yield modulations of the refractive index [Close 1969]. To construct two-dimensional or three-dimensional (3-D) quasicrystals is a very difficult task because conventional methods used in the micro-chip fabrication (such as semiconductor lithography, multi-photon adsorption, template-based techniques, etc.) and also special methods developed for photonic crystals fabrication (such as self-assembling of colloidal micro-spheres or micro-fabrication) are inadequate. Standard two-beams holography produces only sinusoidal modulations in soft matter gratings [Bunning 2000] [Sutherland 1993], whereas patterning of complex structures requires a dual-beam multiple exposure technique [Gauthier 2004], or N laser beams to create a 2-D N-fold quasiperiodic irradiance profile. Both require complex optical setups with drawbacks related to the long term stability and vibrational control of the interference pattern. Previously used to realize periodic photonic crystals [Campbell 2000] [Berger 1997], holographic lithography was recently proposed and used to realize quasicrystals too at the mesoscale in polymer resins [Wang 2003] [Wang 2006], Holographic Polymer Dispersed Liquid Crystals (H-PDLC) [Gorkhali 2005], and holographic plates [Yang 2006]. The holographic lithography is based on the interference pattern of many coherent light beams, that are usually obtained by splitting a single laser beam by suitable grating, prism or dielectric beam splitters [Gorkhali 2006], in a single or multiple exposure process as aforementioned [Gauthier 2004]. Realizing a quasicrystal structure, exhibiting N-fold symmetry, usually requires to control the amplitude and phase of N interfering laser beams, leading to several difficulties, which can limit this technique.

Some research groups [Yang 2006] [Gorkhali 2006] recently have realized PhQCs with holographic technique in organic materials using a multiple-beam interference scheme [Wang 2003] to induce the two-dimensional quasiperiodic structures into a photosensitive substrate, highlighting the advantages of this technique compared to traditional lithographic processes (like e-beam and ion-beam lithography). Moreover, Busch and John [Busch 1999] show the possibility to modulate with a temperature control [Yoshino 1999] or an electric field [Kang 2001] the optical character-

istics of a PhC or a PhQC by using liquid crystals. By adding an active medium, PhQCs can lead to lasing action also in soft matter. First experimental investigation on the laser emission in an organic material has been reported by Notomi et al [Notomi 2004]. They found localized modes that were at variance with the extended modes existing in the PhC-based lasers.

In the last years, together with quasiperiodic, possible optical applications of light propagation in aperiodic media have also deserved a major attention, in order to understand the interplay between the optical properties and the underlying aperiodic arrangement. But it may be envisaged that such structures cannot be realized even in principle by multiple-beam interference. Fibonacci multilayer is an example of aperiodic structure. It shows a delta-like Fourier spectrum characterized by self-similar Bragg-peaks which determine the location and width of the frequency gaps [Fujiwara 1990]. In a recent experiment the propagation of light through porous silicon Fibonacci multilayers has been studied, observing a strong suppressed group velocity for frequencies close to a main band-gap [DalNegro 2003]. Another example of self-similar structure is the Thue-Morse (ThMo) lattice [Macià 2006]. This structure is an example of aperiodic pattern [Kolar 1994], defined by recursive sequences, that cannot be obtained by interference of coherent beams. One-dimensional Thue-Morse gratings are known to exhibit PGB with interesting omnidirectional reflectance [Lee 2006] [Lei 2007]. Very recently, theoretical studies have shown the presence of PBG also in a two-dimensional Thue-Morse structure [Moretti 2007], but experimental realization of photonic structures exhibiting two-dimensional Thue-Morse arrangement has not been reported in the literature until now.

1.2 Proposal of the PhD thesis

The mail goal of this research work is to realize photonic crystals and photonic quasicrystals in organic materials made of liquid crystal and polymer composites. The aim is to exploit soft materials as substrate to be patterned in complex geometries. In this thesis a novel approach for the patterning of complex structures is proposed, in order to functionalize liquid crystal-polymer composites in arrangements with a periodic, quasiperiodic and aperiodic modulation of the dielectric function [Zito 2007] [Zito 2008]. The method is based on the spatial light modulation of the writing laser beam by means of computer-generated holograms (CGHs) for the fabrication either of periodic and quasiperiodic structures with low dielectric contrast modulation, with 1-D, 2-D and even 3-D geometries. In the one-dimensional case, the technique we employed, permitting a large or complete phase separation between the liquid crystal and polymer components, allows the realization of periodic gratings in the Bragg regime, either switchable and passive, that have been already largely employed for photonic and telecommunications applications, but also of structures, either periodic and aperiodic, with novel and interesting properties, as it will be discussed. Two-dimensional and three-dimensional structures have been produced in this work with high rotational symmetry never realized before and

with novel photonic band-gap properties that permit to join the unique behavior of quasicrystals with the advantages of soft matter.

Recently employed for holographic optical tweezers [Grier 1998] [Reicherter 1999] [Liesener 2000], Computer-Generated Holograms (CGHs) permit to create arbitrary 2-D and 3-D configurations of the irradiance distribution, offering nanometer-scale spatial resolution and real-time reconfigurability without any mechanical motion or realignment [Curtis 2002] [Grier 2003]. In this thesis, I demonstrate that computer-generated holography, joined with the advantages furnished by the employment of a programmable Spatial Light Modulator (SLM) [Goodman 1996], may provide an important development of the fabrication processes of photonic structures ensuring at the same time an accurate control and reproducibility of the produced structures, permitting to explore the new research field of disordered matter with unprecedented potential.

The CGH technique has important advantages in comparison with the standard multi-beam holography: it is a single-beam technique that avoids using of complex optical setups, and permits to achieve high resolution dynamical patterns with almost no limits to the pattern design (even not achievable with the interference schemes of standard holography) by real-time configuration of a spatial light modulator. Moreover, pattern with localized defects and channels for cavity or waveguide applications or for other complex photonic devices can be easily introduced, in a single step process, into the structures.

The employed materials exhibit very attracting optical, mechanical, chemical and thermal properties together with flexible processing techniques. The use of liquid crystals, in composites with polymers or infiltrated in patterned structures, allows electrical control of the realized devices [Sutherland 1994] [Caputo 2005]. Combined with holographic fabrication techniques, they can be patterned quite easily into several unique structures, permitting to explore the optical properties in the wide intermediate regime existing between completely ordered and disordered structures. The optics of photonic quasicrystals is an almost unexplored field, promising to yield fascinating new physics as well as exciting photonic applications.

In this work, the SLM-CGH technique has been successfully exploited to realize patterned samples either in the case of 1-D, 2-D and even 3-D structures as aforementioned. Our single-beam technique was developed with three different approaches. Regular patterned samples with good optical contrast were obtained, leading to photonic crystals consisting of functionalization in 1-D periodic structures, as well as 2-D and 3-D structures of novel generation with properties sensitive to the polarization of the incident light, as the periodicity of the grating itself, the diffraction efficiency and the electro-optical response, never realized to our knowledge. Moreover, samples with structures of defects were also produced with a single-step process.

Results of optical and electro-optical characterization of realized samples are presented. Regular but not periodic two-dimensional structures were also obtained, leading to photonic quasicrystals with rotational symmetry up to 23-fold. A particular attention has been aimed to the two-dimensional structures based on substitutional sequences, that is to the gratings realized with aperiodic sequences like the

Thue-Morse that are provided of almost unexplored interesting properties.

A preliminary development of numerical-theoretical models is essential about the photonic band-gaps, transmission and localization properties. The lack of spatial periodicity, and hence of a unit cell, renders impossible the definition of a Brillouin zone, and numerically intractable the study of infinite structures. Besides the finite structure approximation, another method based on the Finite Difference Time Domain (FDTD) algorithm has been used to overcome this problem. Theoretical studies of the transmission spectra of the realized structures are shown. The FDTD simulations demonstrate the importance of the choice of the geometric tiling in the building process of the PhQCs, influencing the characteristics of the photonic band-gap. The PBG dependence on the rotational symmetry for low dielectric contrast quasicrystals is discussed and has permitted to clarify the fundamental role of the tiling geometry above the statistical rotational symmetry.

Realizing photonic quasiperiodic, aperiodic and periodic structures and understanding their optical properties may give an significant contribute to a new research field, presently almost totally unexplored, with great potentialities for the creation and development of innovative reconfigurable photonic devices with unparalleled features.

1.2.1 Outline of the thesis

Chapter 2. In order to clarify the LC role in modulating the dielectric function of the photonic structures made with the SLM-CGH technique and in modulating the diffraction efficiency under the influence of an external electric field, in the first chapter I will briefly present an introduction to the physics of the liquid crystals. The theory of diffraction gratings will de discussed to provide a comprehension of the requirements needed in the fabrication process of such structures. Then, I will introduce a few elements of the physics underlying photonic crystals and quasicrystals, with particular attention paid to the design of the structures by means of the two-beam and multiple-beam holography.

Chapter 3. I will introduce the computer-generated holography, the principles of the spatial light modulation by means of a programmable LC-SLM and the numerical algorithms developed for the holograms generation in a Fourier holographic scheme. The experimental methods developed and adopted in this thesis work will be handled: a) Fourier Holography Scheme (FHS); b) Direct Writing Method (DRM); c) Interference-based Scheme (IS). The structures realized and the electro-optical characterization of the samples will be presented. The FDTD simulations of the transmission spectra and the calculated band diagrams will be showed.

Chapter 4. Finally, the conclusions and perspectives of this research activity will be discussed.

Chapter 2

Theoretical and Experimental Background

Contents

2.1 Liquid Crystals

2.1.1 Liquid Crystal Phases

Liquid Crystals (LC) are materials that present a particular phase of the matter in normal condition of temperature and pressure, just like the solid, the liquid, the gas and the plasma phases. The liquid crystal phase is an intermediate phase between the solid and the liquid.

Solids, liquids, and gases respond to electric and magnetic fields, but the response is minimal even when strong fields are applied. Liquid Crystals, on the contrary, respond to even weak electric and magnetic fields with significant structural changes.

Liquid crystals have been known since 1888 when F. Reinitzer found two melting points in the materials cholesterol benzoate and cholesterol acetate [DeGennes 1993], but it was not until the late 1960's that the development of applications utilizing liquid crystals started. Today liquid crystals displays (LCDs) are very common. Research in this field is paving the way to many other devices exploiting the unique properties of liquid crystals. A wide diversity of new products will see the light on the next future, like rolled up displays, light modulators, switches and other optical components.

The states of matter are distinguishable for the different amounts of order of the material molecules. The solid state consists of a rigid arrangement of molecules: they are constrained to occupy a specific position and they are oriented in a specific way. Unlike the solid state, in the liquid phase the molecules neither occupy a specific average position nor remain oriented in a particular orientation. The amount of order is therefore much less than in a solid. Attractive forces still exist, but the random motion of molecules does not allow the forces between individual molecules to add together.

A solid possesses *positional order* and *orientational order*. When solid melts to liquid, usually, both types of orders are completely lost. However, during this transition can happen that the positional order is lost, but some of the orientational order remains. The liquid crystal phase, in fact, is an example of matter possessing orientational order and not positional order (Figure 2.1).

Liquid Crystals are anisotropic organic material: their constituent molecules are fairly rigid, elongated objects. For pure systems, phase transitions are most easily induced by varying the temperature, these systems are called *thermotropic liquid crystals*; for systems of rods in solution, phase transitions are most easily induced

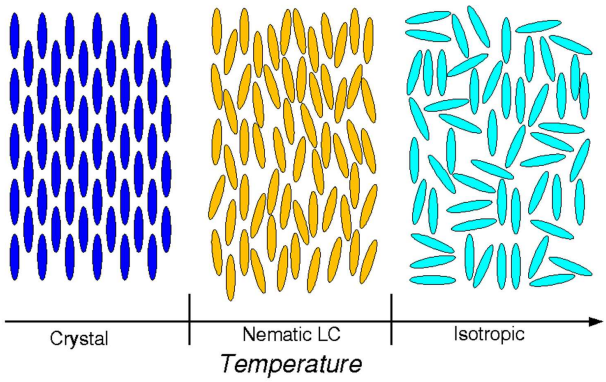

Figure 2.1: The Liquid Crystal phase appears between the Solid and the Liquid: increasing the temperature the positional order is lost, while the orientational remains.

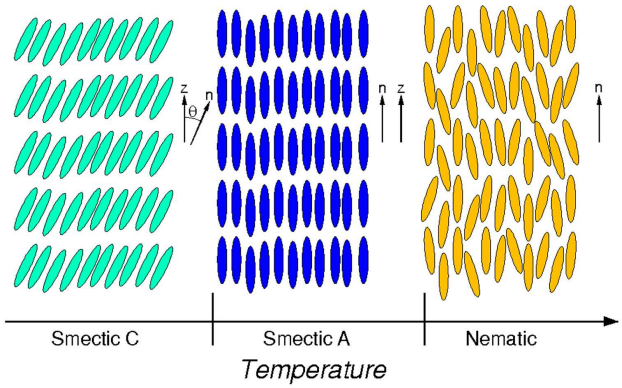

Figure 2.2: Phase sequence for a Liquid Crystal material. The degree of order decreases with increasing the temperature. Liquid crystals materials commonly do not exhibit all the phases shown in figure.

by varying the concentration of rods, these are called *lyotropic liquid crystals*. In the present work, only thermotropic LCs are considered.

The geometrical anisotropy of LC molecules gives rise to various liquid crystal mesophases, all of them characterized by a different degree of positional order. In general, the order of the subsequent phases decreases with increasing the temperature, going from the crystal phase to the isotropic phase passing through the Smectic C, Smectic A and Nematic (Figure 2.2):

- The least ordered liquid crystal phase is the *Nematic* (N) phase where the molecules have no positional order but long range orientational order. Here all the molecules tend to align with their long axes in a preferred direction described by the unit vector $\widehat{n}$ called the *molecular director*. The nematic is a uniaxial medium where the states $\widehat{n}$ and $-\widehat{n}$ are indistinguishable (see Figure 2.2c).

$$\widehat{n} \leftrightarrow -\widehat{n} \tag{2.1}$$

- A higher degree of order is found in *Smectic* liquid crystals. In addition to the orientational order of the director, there is also positional ordering of the molecules in at least one dimension, i.e. the molecules are ordered in layers.

  - In the *Smectic A* phase (SmA) the director is perpendicular to the smectic layers and parallel to the smectic layer normal z (see Figure 2.2b).
  - In the *Smectic C* phase (SmC) the director is tilted with respect to the smectic layer normal (see Figure 2.2b). The angle between z and $\widehat{n}$ is called the tilt angle.

Many other mesophases exist, like the *Smectic B* (SmB) in which the layers are not entirely liquid, and the molecules tend to arrange hexagonally. Liquid crystals materials commonly do not exhibit all this mesophases. Summarizing we can say that for thermotropic liquid crystal material displaying all these phases, the phase sequence with increasing the temperature is

$$Crystalline \rightarrow SmB \rightarrow SmC \rightarrow SmA \rightarrow N \rightarrow Isotropic$$

We can have liquid crystals with chiral molecules: we remind that a chiral object is one which is not superposable on its mirror image. In that case there will be a tendency of forming a helicoidal structure and new mesophases need to be defined:

- A nematic phase with chiral molecules becomes distorted in a helical structure. The director rotates around an axis, named the helix axis, being everywhere perpendicular to it. The pitch of the helix is a full turn through 360°, and, due to the invariance condition of Equation 2.1, the period of the helix is

half of the value of the pitch (Figure 2.3a). Chiral nematics (N*)[1] are called cholesterics[2].

- In the chiral Smectic A (SmA*) there is no helical distortion. In fact, if the molecules were to form a helix with the director perpendicular to the helix axis, the smectic layers should necessarily break, and this will require a big amount of energy. That's why does not usually occur, and the SmA* phase is geometrically indistinguishable from the SmA, but they present different physical properties.

- In the chiral Smectic C (SmC*) helical distortion appears, with the helix axis parallel to the smectic layer normal (Figure 2.3b). In this phase, since molecules are tilted with respect to the smectic layer normal $\widehat{a}$, the system has an other degree of freedom: the direction of the tilt plane, specified from $\widehat{n}$ and $\widehat{a}$.

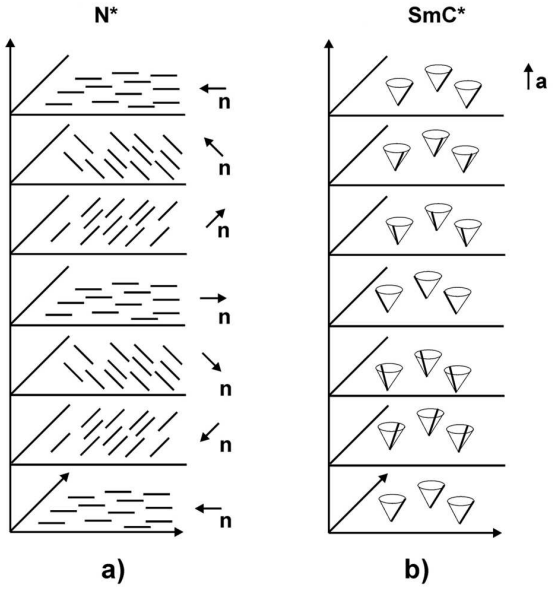

Figure 2.3: Chirality and Liquid Crystals: a) chiral nematic, also called Cholesteric (N*); b) Chiral Smectic C (SmC*).

[1] The * stays for chiral.

[2] If the twisting power is very strong in the cholesteric phase, other phases called blue phases may appear between the cholesteric and the isotropic. In the blue phases there is a twist of the medium in more than one dimension. Liquid crystal appears organized in disclination lines filling the space in a cubic structure. The lattice constant of the blue phases is of the order of the wavelength of visible light, that is why they are called "blue".

2.1.2 Physics of Nematic LCs

As said before, in Nematic Liquid Crystals (NLCs) the centers of gravity of the molecules have no long-range order. However, there is some orientational order, all the rod-like molecules tend to align in a preferred direction described by the *molecular director*.

Let us label **c** the rod axis, and take the average direction of alignment of the molecules **n** along the z-axis. We shall define **c** by its polar angles θ and φ where

$$\begin{aligned} c_x &= \sin\theta\cos\varphi \\ c_y &= \sin\theta\sin\varphi \\ c_z &= \cos\theta \end{aligned}$$

The state of alignment of a nematic can be described by the function $f(\theta,\varphi)d\Omega$, which is the probability of finding rods in a small solid angle $d\Omega = \sin\theta d\theta d\varphi$ around the direction (θ,φ). To describe properly the features of a nematic, $f(\theta,\varphi)$ might have some requirements:

- it must be independent of φ, because of the cylindrical symmetry about **n**;
- $f(\theta) = f(\pi-\theta)$, due to the equivalence between **n** and $-\mathbf{n}$.

Instead of using the full function $f(\theta)$, one prefers to use only one related numerical parameter. The average value

$$\langle\cos\theta\rangle = \langle\mathbf{c}\cdot\mathbf{n}\rangle = \int f(\theta)\cos\theta d\Omega$$

cannot be used: in fact, it vanishes identically because for the second property. The first non-zero multipole is the quadrupole [DeGennes 1993], defined as

$$S = \frac{1}{2}\left\langle\left(3\cos^2\theta - 1\right)\right\rangle = \int f(\theta)\frac{1}{2}\left(3\cos^2\theta - 1\right)d\Omega$$

- If all the molecules are parallel to the z, it means $\theta = 0,\pi$, thus $\cos\theta = \pm 1$ and $S = 1$.
- If they are oriented perpendicular to z, it means $\theta = \pi/2$, and $S = 1/2$.
- If orientations is random, $f(\theta)$ is independent of θ; we would have $\left\langle\cos^2\theta\right\rangle = \frac{1}{3}$ and $S = 0$.

Clearly $f(\theta)$, and so S, critically depends on temperature.

2.1.3 The Continuum Theory

In the previous section we have considered a macroscopically uniform medium, in which $\mathbf{n}$ and S are independent on their position in the space. This approximation is not always true. Let us, now, consider a macroscopically small but microscopically large volume inside the bulk of a liquid crystal. The volume contains a sufficiently large number of molecules so that long-range molecular order and the director are well defined in that region. If we divide the liquid crystal in such small volumes with an orientational direction in each of them we can define this direction at any point in the medium as long as we in fact relate every point with a small region of space. The liquid crystal is then treated as a continuous medium.

At a given temperature T, the $\mathbf{n}(\mathbf{r})$ distribution of a liquid crystal can be found describing by system by its free energy density, imposing the boundary conditions, and minimizing the free energy density. Hence, the main part of the procedure is to find the right expression of the free energy density F_d.

The deformation of the liquid crystal is just a change in molecular orientation, and not in molecular density, i.e. the deformations are gradients in the director field. For most of the situation of interest the distance l over which significant changes of the director field occur are much larger than the molecular dimension a (typically $l \geq 1\mu m$, while $a \sim 20$). So the deformation free energy density F_d may be written in terms of director deformation $\nabla\mathbf{n}$. We expect that:

- F_d goes to zero when $\nabla\mathbf{n} = \mathbf{0}$;
- F_d is a even function in $\mathbf{n}$, because $\mathbf{n} \leftrightarrow -\mathbf{n}$;
- F_d has not linear terms in $\nabla\mathbf{n}$; in fact, they will contradict the previous requirement or they will not respect the cylindrical symmetry;
- F_d has not terms in the form $\nabla\mathbf{u}$, with $\mathbf{u}$ generic vectorial field; in fact these terms would describe only a surface free energy and not the volume free energy (that is because $\int \nabla\mathbf{u}\cdot d\mathbf{r} \equiv \int \mathbf{u}\cdot d\sigma$).

Afterwards these considerations the deformation free energy density may be written in the form

$$F_d = \frac{1}{2}k_{11}\left(\nabla\mathbf{n}\right)^2 + \frac{1}{2}k_{22}\left(\mathbf{n}\cdot\nabla\times\mathbf{n}\right)^2 + \frac{1}{2}k_{33}\left(\mathbf{n}\times\nabla\times\mathbf{n}\right)^2 \tag{2.2}$$

that is the fundamental relation of the continuum theory for nematics. The three constants k_{ii} are elastic constant for splay, twist and bend deformations. All possible deformations of the liquid crystals can be described as a combination of these three basic ones (see Figure 2.4).
Equation 2.2 is a little bit complex for a practical use. A useful approximation is to assume all the elastic constants equal

$$k_{11} = k_{22} = k_{33} = k$$

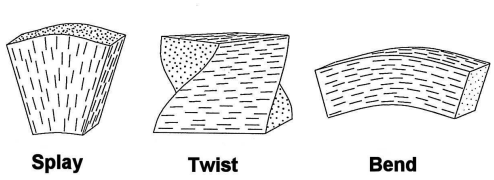

Figure 2.4: The three basic types of elastic deformation in a nematic liquid crystal: splay, twist and bend.

This is called one-constant approximation which gives a more simple form of the free energy density

$$F_d = \frac{1}{2}k\left[(\nabla\mathbf{n})^2 + (\nabla\times\mathbf{n})^2\right] \tag{2.3}$$

Equation 2.3 defining the distortion energies in the bulk of the nematic phase must be, in principle, supplemented by a description of the energies associated with the surface of the sample. In most practical conditions, in fact, the surface forces are strong enough to impose a well-defined direction of the director at the surface; this is what we call strong anchoring.

Instead of minimizing the sum bulk plus surface energies, it is sufficient to minimize only the bulk terms, with fixed boundary conditions for $\mathbf{n}$.

To find the equilibrium condition we have to minimizeF_d with respect to the director deformation $\nabla\mathbf{n}$ and its derivatives, imposing the condition that $|\mathbf{n}|^2 = 1$. Using the Lagrange Multiplier Method, we have to minimize

$$\mathcal{F}_d = \int_V \left\{F_d(n_\alpha, \partial_\beta n_\alpha) - \lambda\,|\mathbf{n}|^2\right\} d\mathbf{r}$$

where λ is a Lagrange Multiplier, and $\partial_\alpha = \frac{\partial}{\partial x_\alpha}$. Assuming the stationary condition under small variations of the director coordinates n_α and their derivatives $\partial_\beta n_\alpha$, we obtain

$$\delta\mathcal{F}_d = \int_V \left\{\frac{\partial F_d}{\partial n_\alpha}\delta n_\alpha + \sum_\beta \frac{\partial F_d}{\partial(\partial_\beta n_\alpha)}\delta(\partial_\beta n_\alpha) - 2\lambda n_\alpha \delta n_\alpha\right\} d\mathbf{r} = 0 \tag{2.4}$$

The second term inside the integral can be calculated inverting the derivation, integrating per parts and letting the surface terms go to zero (strong anchoring hypothesis):

$$\begin{aligned}
\int_V \frac{\partial F_d}{\partial(\partial_\beta n_\alpha)}\delta(\partial_\beta n_\alpha)d\mathbf{r} &= \int_V \frac{\partial F_d}{\partial(\partial_\beta n_\alpha)}\partial_\beta(\delta n_\alpha)d\mathbf{r} \\
&= \frac{\partial F_d}{\partial(\partial_\beta n_\alpha)}\delta n_\alpha\Big]_{\partial V} - \int_V \partial_\beta\left(\frac{\partial F_d}{\partial(\partial_\beta n_\alpha)}\right)\delta n_\alpha d\mathbf{r} \\
&= -\int_V \partial_\beta\left(\frac{\partial F_d}{\partial(\partial_\beta n_\alpha)}\right)\delta n_\alpha d\mathbf{r}
\end{aligned}$$

Substituting in equation 2.4,

$$\delta\mathcal{F}_d = \int_V \delta n_\alpha \left\{ \frac{\partial F_d}{\partial n_\alpha} - \sum_\beta \partial_\beta \left(\frac{\partial F_d}{\partial(\partial_\beta n_\alpha)} \right) - 2\lambda n_\alpha \right\} d\mathbf{r} = 0$$

This must be true for every variations δn_α, so

$$\frac{\partial F_d}{\partial n_\alpha} - \sum_\beta \partial_\beta \left(\frac{\partial F_d}{\partial(\partial_\beta n_\alpha)} \right) = 2\lambda n_\alpha. \tag{2.5}$$

It is usual to define

$$h_\alpha = \frac{\partial F_d}{\partial n_\alpha} - \sum_\beta \partial_\beta \left(\frac{\partial F_d}{\partial(\partial_\beta n_\alpha)} \right),$$

that are the components of the vector $\mathbf{h}$, called *molecular field*. In this way, equation 2.5 establishes that at the equilibrium the director $\mathbf{n}$ is, point by point, parallel to the molecular field $\mathbf{h}$.

Equation 2.5 may also be interpreted in terms of torques: $\mathbf{n}$ is adimensional, whereas $\mathbf{h}$ is a force per unit length over volume. Hence, $\mathbf{h}$ can be related to the density of moment that acts on $\mathbf{n}$. So one can define

$$\tau_{el} = \mathbf{n} \times \mathbf{h}$$

called elastic *torque*. The equilibrium equation become

$$\tau_{el} = \mathbf{0}$$

2.1.4 External Field Effects

Liquid crystals respond to even weak electric and magnetic fields with significant structural changes, showing a redistribution of the molecular director. The ordered structures of anisotropic molecules make the macroscopic physical properties also anisotropic. Because of this anisotropy, the dielectric permittivity and the magnetic permeability depend on the direction in which they are measured, so the electric and magnetic fields are

$$D_i = \varepsilon_{ij} E_j \tag{2.6}$$

$$B_i = \mu_{ij} H_j = (\delta_{ij} + 4\pi\chi_{ij}) H_j \tag{2.7}$$

where $\mu = 1 + 4\pi\chi$.
Because of the cylindrical symmetry around $\mathbf{n}$, the tensors ε_{ij} and χ_{ij} can be written in the form

$$\varepsilon_{ij} = \varepsilon_\perp \delta_{ij} + \varepsilon_{\shortparallel} n_i n_j$$

$$\chi_{ij} = \chi_\perp \delta_{ij} + \chi_{\shortparallel} n_i n_j$$

Introducing this in equations 2.6 and 2.7, we have

$$\begin{aligned} \mathbf{D} &= \varepsilon_{\perp}\mathbf{E} + \Delta\varepsilon(\mathbf{n}\cdot\mathbf{E})\mathbf{n} \\ \mathbf{B} &= (1+4\pi\chi_{\perp})\mathbf{H} + 4\pi\Delta\chi(\mathbf{n}\cdot\mathbf{H})\mathbf{n} \end{aligned}$$

where $\Delta\varepsilon = \varepsilon_{\shortparallel} - \varepsilon_{\perp}$ and $\Delta\chi = \chi_{\shortparallel} - \chi_{\perp}$ are the dielectric anisotropy and the magnetic anisotropy respectively.

The electromagnetic energy density is

$$W = \frac{1}{8\pi}(\mathbf{E}\cdot\mathbf{D} + \mathbf{H}\cdot\mathbf{B})$$

To obtain the total free energy density in presence of external fields, we have to add this term to the deformation free energy density

$$F_{TOT} = F_d + W$$

Because one can express

$$dW = \frac{1}{4\pi}(\mathbf{E}\cdot d\mathbf{D} + \mathbf{H}\cdot d\mathbf{B})$$

F_{TOT} is, therefore, a function of the independent variable $\mathbf{D}$ and $\mathbf{B}$, of the temperature T and the volume V: the equilibrium is reached minimizing F_{TOT} with T, V, $\mathbf{D}$ and $\mathbf{B}$ constant.

In order to work with $\mathbf{E}$ and $\mathbf{H}$ constant, we define the new potential G as the function

$$G = F - \frac{1}{4\pi}(\mathbf{E}\cdot\mathbf{D} + \mathbf{H}\cdot\mathbf{B}) = F - W$$

which is a function of $\mathbf{E}$, $\mathbf{H}$, T and V. Analogously to the situation without fields, we find that the molecular director is everywhere parallel to a molecular field, given by the sum of a distortion term, an electric term and a magnetic one:

$$\mathbf{h} = \mathbf{h}_d + \mathbf{h}_e + \mathbf{h}_m = \mathbf{h}_d + \frac{\Delta\varepsilon}{4\pi}(\mathbf{n}\cdot\mathbf{E})\mathbf{E} + \boldsymbol{\Delta}\chi(\mathbf{n}\cdot\mathbf{H})\mathbf{H}.$$

We can define the *electric torque* and the *magnetic torque*,

$$\begin{aligned} \tau_e &= \mathbf{n}\times\mathbf{h}_e = \frac{\Delta\varepsilon}{4\pi}(\mathbf{n}\cdot\mathbf{E})(\mathbf{n}\times\mathbf{E}) \\ \tau_m &= \mathbf{n}\times\mathbf{h}_m = \Delta\chi(\mathbf{n}\cdot\mathbf{H})(\mathbf{n}\times\mathbf{H}) \end{aligned}$$

At equilibrium

$$\tau_d + \tau_e + \tau_m = \mathbf{0}.$$

Nematic liquid crystals might show both positive and negative value of the dielectric anisotropy:

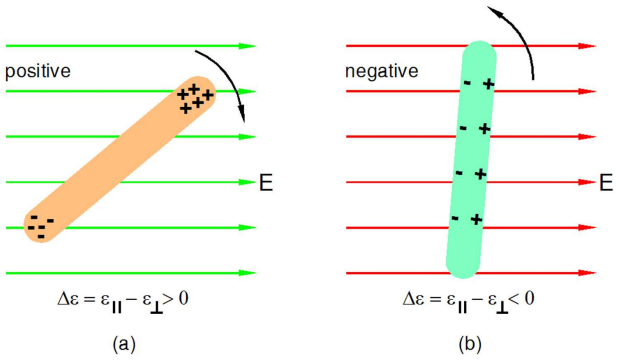

Figure 2.5: Orientation of an electric dipole by an electric field. In (a) the dipole is along the long axis of the molecule whereas in (b) it lies across the long axis. The presence of the electric field causes rotation of the molecule.

- if $\Delta\varepsilon > 0$, the molecular director tends to dispose parallel to electric field, Figure 2.5a;
- if $\Delta\varepsilon < 0$, the molecular director tends to dispose perpendicular to electric field, Figure 2.5b.

The magnetic anisotropy $\Delta\chi$ is almost always positive, and the molecular director tends to align parallel to the magnetic field.

2.1.4.1 Alignment

The term alignment, or texture, refers to the orientation of liquid crystal molecules in the vicinity of a surface. Liquid crystals are usually confined between closely

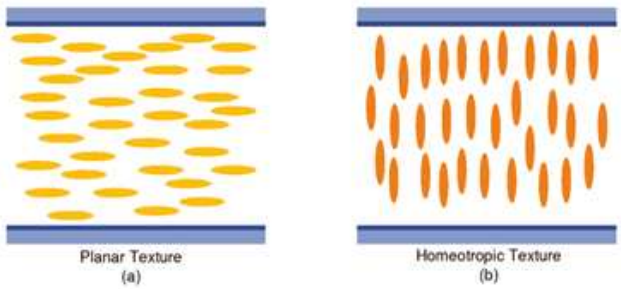

Figure 2.6: LC alignments inside a cell: (a) planar alignment; (b) homeotropic alignment.

spaced plates with an alignment layer that forces the direction of the molecules near the surface:

- planar alignment, the director aligns parallel to the cell surface, see Figure 2.6a.
- homeotropic alignment, the molecular director is perpendicular to the cell surface, see Figure 2.6b;

2.1.5 Freédericksz Transition

Let us consider what happens when a small amount of nematic liquid crystal is placed between two pieces of glass that have been treated to produce alignment of the director parallel to the surface (Figure 2.7a). Near the two glass surfaces, the director is constrained to point in certain direction (parallel to the surface). Supposing that the NLC has positive dielectric anisotropy, $\Delta\varepsilon > 0$, and an electric or magnetic field is applied perpendicular to the glass surfaces: the field tends to orient the director parallel to the field. The molecules near the surface are not free to reorient with the field like the one in the bulk of the cell. The electric or magnetic field thus causes the director to change its orientation in the middle of the cell, with diminishing change closer to the surfaces. This deformed structure is shown in Figure 2.7b. This deformation does not occur gradually as the strength of the field is increased. In fact, if the electric field is strong enough to overcome the elastic torque, the small fluctuations of the director can be amplified by the electric field, resulting in a reorientation of $\hat{\mathbf{n}}$ along $\mathbf{E}$. For fields with strengths below a certain value, the LC remains undeformed. Then, at some threshold value of the field, the deformation begins. The geometrical transition from an undeformed structure to a deformed one, in function of the electric field, is called *Freédericksz transition.*

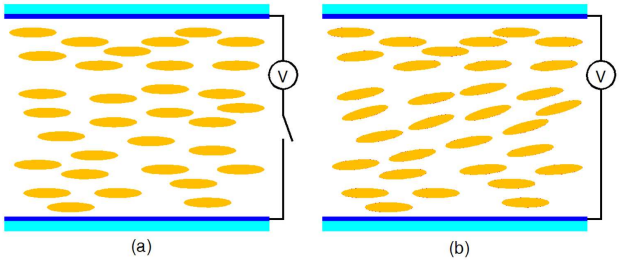

Figure 2.7: Freedericksz transition: cell has planar alignment. When the field is below the threshold level the liquid crystal orientation is given by the alignment (a); above the threshold the field tends to align the director perpendicular to the surfaces (b).

The presence of a threshold value E_0 in this reorientation process is known as *Freédericksz effect*: for $E < E_0$ no reorientation is observed; for $E > E_0$ reorientation begins, starting from the center of the sample, where the restoring torque exerted by the elastic forces is weaker (Figure 2.7). The dependence of the angular orientation of the molecular director on the electric filed is shown in Figure 2.8.

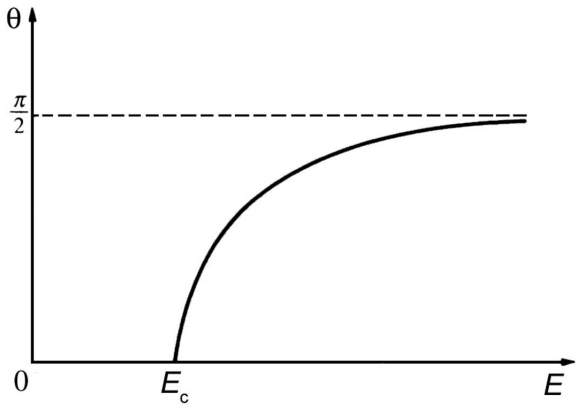

Figure 2.8: Freedericksz transition.

The value of E_0 can be derived by a simple argument [DeGennes 1993]. Let us consider the director configuration $\hat{\mathbf{n}}$ correspondent to a small perturbation $\delta\mathbf{n}$ of the undistorted configuration $\hat{\mathbf{n}}_0$

$$\hat{\mathbf{n}} = \hat{\mathbf{n}}_0 + \delta\mathbf{n}, \tag{2.8}$$

with $\delta\mathbf{n}$, orthogonal to $\hat{\mathbf{n}}_0$ and parallel to $\mathbf{E}$, only depends on z (where the z-axis is normal to the boundaries, as in Fig. 2.7). For this slightly distorted configuration, the elastic free energy density becomes

$$F_d = \frac{1}{2} k_i \left(\frac{\partial \delta\mathbf{n}}{\partial z} \right)^2, \tag{2.9}$$

where k_i represents the splay, twist or bend elastic constant according to the case considered, as shown in Fig. 2.4. Analogously the electric contribution to the free energy density becomes, apart from a factor independent of $\delta\mathbf{n}$,

$$F_E = -\frac{\Delta\varepsilon}{8\pi} E^2 \delta\mathbf{n}^2. \tag{2.10}$$

Assuming strong anchoring at the boundaries, we have that $\delta\mathbf{n}$ must be null at $z = 0$ and $z = d$, where d is the sample thickness. Hence, we can expand $\delta\mathbf{n}$ in a Fourier series

$$\delta\mathbf{n} = \sum_{\nu=1}^{\infty} \delta n_\nu \sin \frac{\nu\pi z}{d}. \tag{2.11}$$

Inserting this expression in the total free energy density $F_d + F_E$ and integrating over the thickness d, one obtains (per unit surface)

$$\mathcal{F} = \frac{d}{4} \sum_{\nu=1}^{\infty} \delta n_\nu^2 \left[k_i \left(\frac{\nu\pi}{d} \right)^2 - \frac{\Delta\varepsilon}{4\pi} E^2 \right]. \tag{2.12}$$

As the system moves towards a stable state, the free energy $\mathcal{F}$ describing the deformed state must be negative for some values δn_ν. The deformation mode that requires the weakest field to be induced is the one with $\nu = 1$; this mode can be excited by any electric field respecting the inequality

$$\frac{\Delta\varepsilon}{4\pi}E^2 > k_i\left(\frac{\pi z}{d}\right)^2. \tag{2.13}$$

The minimum of such values is the sought threshold field

$$E_{0i} = \frac{\pi}{d}\sqrt{\frac{4\pi}{\Delta\varepsilon}k_i}. \tag{2.14}$$

with $i = 1$ if the alignment passes from the planar to the homeotropic, $i = 2$ if the alignment remains planar but orthogonal to the initial one, $i = 3$ for the passage from homeotropic to planar. As expected, the first deformation mode corresponds to a higher distortion in the center of the sample. For higher electric fields, higher modes are excited and the distortion moves closer to the boundaries.

It can be demonstrated that when the strong anchoring assumption is no more valid (weak surface anchoring), reorientation occurs even at the boundaries, and the threshold field may decrease.

It is interesting that the field is proportional to d^{-1}, so if we consider that the voltage to apply is $V = Ed$, one has that the critical voltage is independent to the cell thickness d:

$$V_c = \sqrt{\frac{4\pi^3}{\varepsilon_a}k_i}.$$

2.1.6 Reorientation Dynamics

The reorientation configuration interesting for the present work is the one corresponding to a bend distortion of a homeotropically aligned sample. Studying dynamics in this geometry requires some care, for two different reasons: first, bend distortion is always accompanied by a splay distortion (and vice versa); second, bend and splay distortions inevitably involve a flow process coupled with the director rotation (backflow effect)[3]. This effect will be neglected.

In this assumption and for infinite anchoring energy, the equation of motion of the director is expressed through the balance of elastic, electric and viscous torques

$$\left(k_1\cos^2\theta + k_3\sin^2\theta\right)\frac{\partial^2\theta}{\partial z^2} + (k_3 - k_1)\sin\theta\cos\theta\left(\frac{\partial\theta}{\partial z}\right)^2 + \\ + \frac{\Delta\varepsilon}{4\pi}E^2\sin\theta\cos\theta = \gamma_1\frac{\partial\theta}{\partial t}. \tag{2.15}$$

Here, z is a coordinate normal to the boundaries, θ is the angle between the director and the z-axis, γ_1 is the rotational viscosity; the inertial term ($I\frac{\partial^2\theta}{\partial t^2}$) has also been

[3]Backflow effects are absent in the pure twist deformation. For this reason, this is the case more often studied in literature.

disregarded. In the one-constant ($k_1 \sim k_3$) and small angle approximations, a simplified expression is obtained

$$k_3 \frac{\partial^2 \theta}{\partial z^2} + \frac{\Delta\varepsilon}{4\pi} E^2 \left(\theta - \frac{2}{3}\theta^3 \right) = \gamma_1 \frac{\partial \theta}{\partial t}. \tag{2.16}$$

Given the boundary conditions $\theta(0) = \theta(d) = 0$, we can expand the solution in a Fourier series. For small reorientations, i.e. for electric fields just over the threshold, we can neglect higher harmonics and look for solutions in the form

$$\theta(z,t) \simeq \theta_m(t) \sin \frac{\pi z}{d}. \tag{2.17}$$

Substituting in Eq. 2.16, multiplying both sides by $\sin \frac{\pi z}{d}$ and integrating over the thickness d, one arrives at

$$\left(1 - \frac{E_0^2}{E^2}\right) \theta_m - \frac{1}{2}\theta_m^3 = \frac{4\pi\gamma_1}{\Delta\varepsilon E^2} \frac{d\theta_m}{dt}, \tag{2.18}$$

where Eq. 2.14 has been used.

If the initial director configuration is undistorted (but still subjected to thermal fluctuations) and an electric field is applied at $t = 0$, the solution of Eq. 2.18 is

$$\theta_m^2(t) = \frac{\theta_m^2(\infty)}{1 + \left(\frac{\theta_m^2(\infty)}{\theta_m^2(0)} - 1 \right) \exp\left(-\frac{2t}{\tau_E} \right)}, \tag{2.19}$$

where $\theta_m(\infty)$ represents the steady state value of θ_m, $\theta_m(0)$ is the amplitude of the initial director fluctuations and τ_E is the reorientation time constant under the influence of the electric field

$$\tau_E = \frac{\gamma_1}{\frac{\Delta\varepsilon}{4\pi} E^2 - k_3 \frac{\pi^2}{d^2}} = \frac{\gamma_1 d^2}{k_3 \pi^2} \frac{1}{\left(\frac{E^2}{E_0^2} - 1 \right)} = \frac{4\pi\gamma_1}{\Delta\varepsilon \left(E^2 - E_0^2 \right)}. \tag{2.20}$$

On the other hand, when the director, initially in some distorted configuration $\theta(z,0)$, reorients itself under the only action of the restoring elastic forces, putting $E = 0$ in Eq. 2.16 (term in θ^3 can also be neglected) leads to the solution

$$\theta(z,t) \simeq \theta_0 \sin \frac{\pi z}{d} \exp\left(-\frac{t}{\tau_0} \right). \tag{2.21}$$

Here θ_0 is the maximum deformation angle in the initial director profile, whereas τ_0 is the restoring time constant

$$\tau_0 = \frac{\gamma_1 d^2}{k_3 \pi^2}. \tag{2.22}$$

In the case of larger initial deformation, higher harmonics should be taken into account. However, the time constant corresponding to the n-th harmonic results to be

$$\tau_{0,n} = \frac{\gamma_1 d^2}{k_3 \pi^2 (2n+1)^2} = \frac{\tau_0}{(2n+1)^2}. \tag{2.23}$$

This means that higher order distortions decay much faster than the fundamental mode and can thus be disregarded after a relatively short time.

2.1.7 Interaction with Light: Propagation in Anisotropic Media

The optical properties of liquid crystals are one of the most interesting and certainly the most beautiful features of the phase. How LCs effect light is also the basis for just about all the applications of liquid crystals. Two aspects are extremely relevant:

- due to anisotropy, light propagates in different way with respect to the molecular director orientation;
- light itself can reorient the liquid crystal, because light is an electro-magnetic field, and this reorientation of the LC modify the propagation of light giving arise to non-linear optical effect. This situation will not be discussed in this thesis.

Let us consider a plane wave $e^{i(\mathbf{kr}-\omega t)}$ linearly polarized, where ω is its frequency, $\mathbf{k} = \frac{\omega}{c} n\mathbf{s}$ the wave vector, and n the refractive index of the medium, and $\mathbf{s}$ the unit vector normal to the wave front. The Maxwell equantions are

$$\mathbf{k} \times \mathbf{H} = -\frac{\omega}{c}\mathbf{D} \tag{2.24}$$

$$\mathbf{k} \times \mathbf{E} = \frac{\omega}{c}\mathbf{B} \tag{2.25}$$

$$\mathbf{k} \cdot \mathbf{D} = 0 \tag{2.26}$$

$$\mathbf{k} \cdot \mathbf{B} = 0 \tag{2.27}$$

where the constitutive equations are

$$D_i = \varepsilon_{ij} E_j \tag{2.28}$$

$$B_i = \mu_{ij} H_j \tag{2.29}$$

To study the optical properties of the medium we can neglect the effects due to the magnetic permeability, in fact $\mu_{ij} \sim 1\delta_{ij}$, and equation 2.29 becomes

$$\mathbf{B} = \mathbf{H} \tag{2.30}$$

From equations 2.26, 2.27 and 2.30 descends that $\mathbf{D}$, $\mathbf{H}$ and $\mathbf{k}$ make a tern of orthogonal vector. Equation 2.28 establishes that $\mathbf{D}$ is not in general parallel to $\mathbf{E}$, and so the Poynting vector, proportional to $\mathbf{E} \times \mathbf{H}$, is not parallel to $\mathbf{k}$. In other words, in anisotropic media the energy flux, which determines the propagation direction is not oriented in the same direction as the wave front propagation.
From equations 2.24 and 2.25, using also equation 2.30, we get

$$\frac{\omega^2}{c^2}\mathbf{D} = -\mathbf{k} \times (\mathbf{k} \times \mathbf{E}) = k^2\mathbf{E} - \mathbf{k}(\mathbf{k} \cdot \mathbf{E})$$

that, using equation 2.28, after same algebra, becomes

$$\sum_j (k_i k_j + \frac{\omega^2}{c^2}\varepsilon_{ij} - k^2\delta_{ij}) E_j = 0$$

This is a three equations system with three unknown quantities. It has non-null solutions only if

$$\det(k_i k_j + \frac{\omega^2}{c^2}\varepsilon_{ij} - k^2\delta_{ij}) = 0$$

Letting $\mathbf{p} = n\mathbf{s}$,

$$\det(p_i p_j + \varepsilon_{ij} - n^2\delta_{ij}) = 0 \tag{2.31}$$

Equation 2.31, called *Fresnel Equation*, has solutions $\pm\mathbf{n}_1$ and $\pm\mathbf{n}_2$, where the sign + and − correspond to the two propagation directions. For an arbitrary direction, there are two independent wave with phase velocity c/n_1 and c/n_2.

2.1.7.1 Uniaxial Media

Commonly the tenson ε_{ij} is real (for transparent material like LC) and symmetric [Born 1980]. The reference system in which this tensor ε_{ij} is diagonalizable defines the *princial axis* of the system. If one element of the diagonal is different from the other two that are egual, the medium is said to be *uniaxial*. The axis relative the diagonal element different from the other two is called the *optic axis*, because the optical properties of the material are invariant under rotations around this axis. If all the diagonal elements are different, the medium is *biaxial*.

Nematic LC are uniaxial, and the optic axis is the molecular director.

Let us take z parallel to the optic axis, the tensor ε_{ij} of a NCL is

$$\varepsilon_{ij} = \begin{pmatrix} \varepsilon_\perp & 0 & 0 \\ 0 & \varepsilon_\perp & 0 \\ 0 & 0 & \varepsilon_{\shortparallel} \end{pmatrix} \tag{2.32}$$

The propagation direction of the wave is given by the unit vector $\mathbf{s} = \mathbf{s}(\theta, \varphi)$. Because of the symmetry around z, φ can be chosen $\varphi = 0$, that means we are considering a wave propagating in the plane$x - z$. Under these conditions $\mathbf{s} = (\sin\theta, 0, \cos\theta)$, introducing in equation 2.31 with the 2.32, we get the new Fresnel equation

$$(n^2 - \varepsilon_\perp)(\varepsilon_\perp\varepsilon_{\shortparallel} - n^2\varepsilon_{\shortparallel}\cos^2\theta - n^2\varepsilon_\perp\sin^2\theta) = 0$$

which has the two solutions

$$n_o = \sqrt{\varepsilon_\perp} \tag{2.33}$$

$$n_e(\theta) = \frac{n_o n_e}{\sqrt{n_e^2\cos^2\theta + n_o^2\sin^2\theta}} = \sqrt{\varepsilon_{\shortparallel}} \tag{2.34}$$

Corresponding to these solutions there are two values of the wavevector:

$$k_1 = \frac{\omega}{c}n_o$$

$$k_2 = \frac{\omega}{c}n_e(\theta)$$

A linearly polarized light wave propagating perpendicular to the optic axis and its **E**-vector parallel to the optic axis sees the refractive index n_e: the wave is called *extraordinary* wave. If the **E**-vector is perpendicular to the optic axis, the wave sees the refractive index n_o the wave is *ordinary*. If the E-vector makes some angle with the optic axis, the wave is split up into two waves, which simultaneously propagate through the medium with different speeds. Hence, an optically anisotropic medium is said to be birefringent, and the birefringence is

$$\Delta n = n_{\shortparallel} - n_{\perp}$$

In liquid crystals the birefringence is typically $0.1 \div 0.2$, an extremely high value compared with other materials.

2.1.8 Polymer Dispersed Liquid Crystals (PDLC)

2.1.8.1 Introduction

Polymer Dispersed Liquid Crystals (PDLCs) consist in a dispersion of liquid crystal droplets embedded in a polymeric matrix. As they share many features with the related holographic-PDLCs, this section provides a brief overview on their morphological, optical and electro-optical properties. For a more thorough analysis see [Simoni 1997] and [Sutherland 1993].

2.1.9 Morphology

PDLCs are realized from a homogeneous mixture of a liquid crystal and fluid prepolymer. Polymerization can be obtained in different ways: thermally, by solvent evaporation or by optical curing, the latter being the method also used for holographic-PDLCs (HPDLCs) (details will be discussed in 3.1.6). As liquid crystal is not very soluble in polymer, polymerization produces the phase separation of LC and the formation of small nematic droplets. Droplet dimension is typically about a few microns, even though it can vary in the range $0.01 \div 20\mu m$, depending on the material properties and the preparation procedure.

An important issue is the alignment of the LC director inside each droplet. The topic is quite complex and have been object of deep study. Many different configurations are possible, critically depending on the droplet dimension, on its ellipticity, and on the values of LC elastic constants. Some of the most common geometries are radial (Figure 2.9b) and axial, corresponding to normal anchoring to the surfaces, and bipolar (Figure 2.9a), corresponding to tangential anchoring.

The LC director alignment can be synthetically described by introducing a droplet director $\mathbf{N}_d$, representing the average orientation of the liquid crystal director $\hat{\mathbf{n}}$ in each droplet, and a droplet order parameter S_d, describing the geometrical fluctuations of $\hat{\mathbf{n}}$ with respect to $\mathbf{N}_d$ in the droplet volume V_d

$$S_d = \frac{1}{2}\left\langle 3\left(\mathbf{N}_d \cdot \hat{\mathbf{n}}\right)^2 - 1 \right\rangle_{V_d}. \tag{2.35}$$

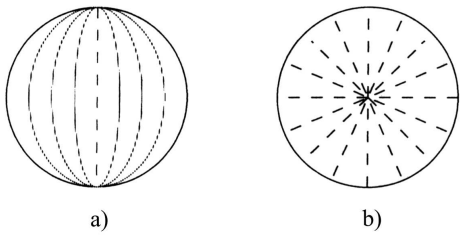

Figure 2.9: Two possible director configurations in liquid crystal droplets: a) bipolar; b) radial.

2.1.10 Optical Properties

As the diameter of the LC droplets is comparable or larger than the light wavelength, PDLCs exhibit a strong light scattering and appear cloudy on visual inspection. The amount of scattered light is proportional to the index mismatch between the polymeric matrix and the droplets, that can be as high as 0.1, due to the high birefringence of the liquid crystal. When no electric field is applied, the droplets directors are randomly oriented, and the index mismatch changes from droplet to droplet depending on their orientation. In fact, droplets are optically anisotropic, with the optical axis given by the droplet director. Therefore one can introduce an extraordinary refractive index of the whole droplet, n_{ed}, defined as the average index experienced by a light wave polarized along $\mathbf{N}_d$ and traveling in a direction normal to it. Analogously, one can define a droplet ordinary refractive index n_{od}, defined as the average index experienced by a light wave traveling in a direction parallel to $\mathbf{N}_d$ and with any transversal polarization. These values depend in a complicated way on the droplet shape and on the liquid crystal alignment inside the droplet. Calculations can be worked out in the case of spherical bipolar droplets (Figure 2.9a), with the following results:

$$n_{ed}(S_d) = \frac{n_o n_e}{\sqrt{n_e^2 + \frac{1}{3}\left(n_o^2 - n_e^2\right)(2S_d + 1)}}, \tag{2.36a}$$

$$n_{od}(S_d) \simeq \frac{2}{\pi} n_o F\left(\frac{\pi}{2}, \frac{\sqrt{\frac{2}{3}\left(n_e^2 - n_o^2\right)(1 - S_d)}}{n_e}\right). \tag{2.36b}$$

In these equations n_o and n_e represent the ordinary and extraordinary LC refractive indices respectively, and F is the complete elliptic integral of the first kind, defined as

$$F\left(\frac{\pi}{2}, m\right) = \int_0^1 \frac{dx}{\sqrt{(1 - x^2)(1 - m^2 x^2)}}. \tag{2.37}$$

As expected, Eqs. 2.36 reduce to n_e and n_o for uniform director alignment along the droplet axis ($S_d \longrightarrow 1$).

2.1.11 Switching Properties

When an electric field is applied, for instance by means of an external voltage, all the droplet directors tend to align themselves parallel to the field, provided the liquid crystal own a positive dielectric anisotropy. If the droplet ordinary refractive index is chosen to match the polymer refractive index, incident light experiences an optically homogeneous materials and no scattering is observed: the PDLC structure becomes transparent.

Discussing the Freédericksz effect, it has been observed that the threshold field is proportional to d^{-1}; as a consequence, the voltage $V = Ed$ necessary to reorient an ordinary homogeneous liquid crystal cell does not depend on the cell thickness. This is not the case for PDLCs: in this materials the electric field E_0 needed to switch the sample is not inversely proportional to the sample thickness, but to the average radius of the droplet R. As for the droplet refractive indices, exact calculations involve assumptions on the droplet shape and the LC alignment. The model proposed by [Reshetnyak 1996] predicts that, in the case of a quasi-ellipsoidal droplet with small radius of curvature, the reorientation of $\mathbf{N}_d$ under an applied electric field is described by the equation

$$\theta(E) = \frac{1}{2}\arctan\left(\frac{2u\sqrt{1-u^2}}{2u^2 - 1 + (E/E_0)^2}\right), \tag{2.38}$$

in which θ is the angle between $\mathbf{E}$ and $\mathbf{N}_d$, E_0 is the critical field for switching, and $u = \cos\theta_0$ with θ_0 being the value of θ for $E = 0$. The critical field is inversely proportional to the length of the droplet major axis and increases as the droplet aspect ratio increases.

2.2 1-D Holographic Diffraction Gratings

In the following section I will introduce some theoretical important elements in relation to the 1-D diffraction structures that have been produced during this research work.

A switchable diffraction grating is a key component for the realization of several devices used in the chain of optical communication networks, such as switches, Add-and-Drop systems, beam deflectors, routers [Gaylord 1985] [Morthier 1997].

Modern transport networks not only provide the physical transfer of information, but must do it in an efficient way, with the flexibility to change information quickly and appropriately among a broad number of interconnections.

Bragg Diffraction Filters are the basic element of several electro-optical devices (examples are reported in Figures 2.10 and 2.11): depending on its pitch Λ and its refractive index n, a Bragg grating will select a wavelength corresponding to the Bragg wavelength, $\lambda_B = 2n\Lambda$. For instance, if we send to a Bragg grating a wavelengths group it will transmit all of them except λ_B, if the grating works in reflection. Hence, a reflective Bragg grating works exactly as a selective mirror (see Figure 2.10a). If the Bragg grating works in transmission, the Bragg wavelength will

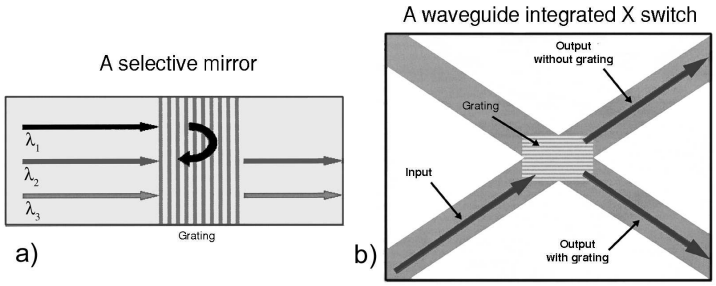

Figure 2.10: Bragg gratings for optical devices: a) a selective wavelength mirror; b) a switch.

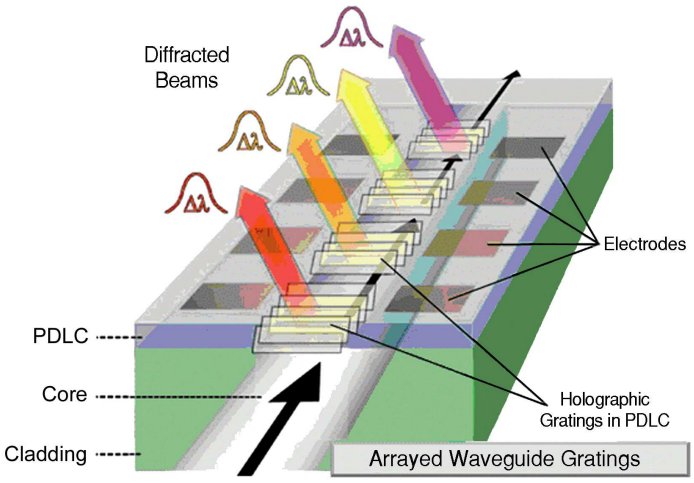

Figure 2.11: A succession of tunable Bragg gratings integrated in a waveguide acts as an optical multiplexing/de-multiplexing device.

be diffracted of a certain angle (given by the Bragg condition $\sin\vartheta_B = \lambda(2\Lambda)^{-1}$): driving somehow the grating parameters, like the refractive index, this angle can be modulated, and the grating can act like a switch (see Figure 2.10b).

One of the easiest way to realize an optical multiplexing or demultiplexing device is to integrate one or several switchable gratings in a guiding system such as a fiber or a waveguide [Domash 2000]: as you can see in Figure 2.11 every grating acts on a wavelength, which can be, as instance, added or removed from the wave-packet.

Laser-induced formation of diffraction gratings in liquid crystal-polymer composites is an item of increasing interest, both from a fundamental and technical point of view, for several reasons: their large electro-optical effect, the large scale integrability and their optical transparency (low losses). Standard two-beam holography consists in inducing a 1-D periodic modulation of the refractive index contrast into a photosensitive material by transferring the irradiance distribution produced by the interference of two plane waves (usually a single laser beam divided into two paths after being properly expanded). In this section a short outline on holographic gratings will be given. Details of the recording process will be discussed in the section 3.1.6.

In a conventional recording technique, such as photography, a three dimensional scene is recorded by an optical system on a light sensitive surface. The system records the intensity distribution in the original scene, but all information on the relative phases of the light waves from different points is lost. What we have is only a two-dimensional image of the scene.

In order not to lose this information, the main idea of holography is to record both the amplitude and the phase of the light scattered by the object. Since, typically, recording media respond only to light intensity, it is necessary to convert the phase information into variations of the light irradiance. This is done by using coherent illumination, like laser light. The final product that we have is a hologram recorded on a flat surface, which may reproduce a three-dimensional image after reconstruction [Goodman 1996].

Theory of optical holography is discussed in details by [Hariharan 1984]. Here, the different types of holographic gratings that can be recorded by an interference pattern of laser light will be briefly discussed [Arns 1998].

2.2.1 Classification of the Holographic Gratings

Holographic gratings can be classified in different typologies, each one characterized by a proper geometry and efficiency.

A first characterization can be done with respect to the effect that the grating may have on the incident light, modulating its phase profile or amplitude:

- a grating showing a periodic variation of the refractive index, that is a periodic dielectric function, produces a phase modulation of the incident ray, that is a *phase grating*;

- a periodicity in the absorption coefficient produces a modulation of the incident light amplitude, and we talk about *amplitude grating*.

A second characteristic having relevant consequences in the grating features is the thickness of the recording medium. We might have:

- *thin holograms*, when the thickness of the recording material is small compared with the average spacing of the interferential fringes;
- *thick holograms* or *volume holograms*, if the medium thickness is bigger than the spacing of the fringes.

Theoretically, both of this geometries can be designed with the fringes perpendicular (*transmission gratings*) or parallel (*reflection gratings*) to the grating plane. But when the grating thickness is negligible, like in thin gratings, the only configuration we might have is with the fringes perpendicular to the grating plane (see Figure 2.12). Based on these three classifications, we can have six types of holograms:

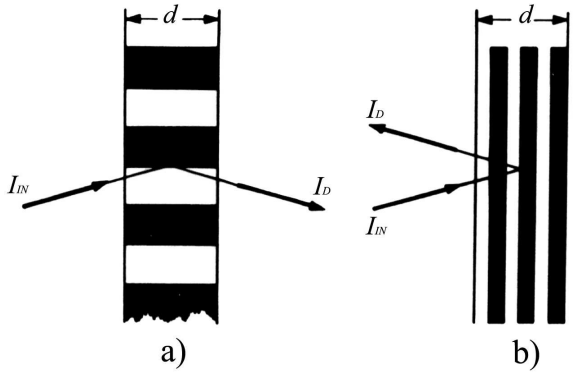

Figure 2.12: Holographic Gratings: (a) in transmission and (b) in reflection.

- thin phase holograms, working in transmission;
- thin amplitude holograms, working in transmission;
- thick phase holograms, working in transmission;
- thick phase holograms, working in reflection;
- thick amplitude holograms, working in transmission;
- thick amplitude holograms, working in reflection.

These geometries yield to different diffraction efficiencies of the granting [Hariharan 1984]. Moreover, different thickness gratings, typically, work in different diffraction regimes: thin holograms in the Raman-Nath regime, whereas volume grating in the Bragg regime. Afterwards, criteria to distinguish gratings typologies will be useful (see [Gaylord 1985] for details).

The distinction between these two regimes can be related to the parameter Q [Kogelnik 1972] defined by the relation

$$Q = \frac{2\pi\lambda d}{n_0\Lambda^2}$$

where Λ is the grating pitch, n_0 the average refractive index, and where d measures the thickness of the grating.

- If $Q < 1$, the grating thickness is small compared to the grating spacing and we talk about *Raman-Nath regime*. The diffraction maxima are given by the equation

$$\sin\vartheta_m = m\frac{\lambda}{\Lambda} \pm \sin\vartheta_i \tag{2.39}$$

  where m is the diffraction order, ϑ_i is the angle of incidence, and ϑ_m is the angle of the m-order diffracted ray, both with respect to the normal to the grating plane. The sign of $\sin\vartheta_i$ is $-$ if the two rays stay on the same side of the normal to the grating, and $+$ otherwise. Such a thin grating diffracts the incident wave into a large number of orders.

- If $Q > 1$, we talk about thick grating. Equation 2.39 still occurs, but the diffracted intensity is maximum only when the incidence angle and the first diffracted order are coincident. In such situation, we have

$$\sin\vartheta_B = \frac{\lambda}{2\Lambda},$$

  known as the *Bragg condition*. For such gratings, light may be completely transmitted into the zero order or diffracted into the first order.

The latter case permits to realize an active Bragg grating, as a volume phase grating, working in transmission, that represents a basic device for many electro-optical applications [Morthier 1997]. The 1-D periodic structures produced in this thesis manifest this kind of behavior as it will be further discussed in 3.1.

2.2.2 Thin Holograms

If the thickness of the recording material is small compared with the average spacing of the interference fringes, the grating obtained can be classified as a thin hologram. As said before, it can work only in transmission.

Let Λ be the grating pitch, with the z-axis perpendicular to the surfaces of the medium and the x-axis perpendicular to the fringes. Let consider the grating infinite

along the y-axis. Such a hologram exhibits a spatially varying complex amplitude transmittance:

$$T(x) = \tau(x)e^{-i\phi(x)},$$

where $\tau(x) = |T(x)| \in [0, 1]$. If incident light is a plane wave, that is

$$E(x, z) = E_0 e^{-i\mathbf{kr}},$$

with wavevector $\mathbf{k} = k_x\hat{\mathbf{x}} + k_z\hat{\mathbf{z}}$, the transmitted wave will be a plane wave too given by

$$E(x, z) = \tau(x)E_0 e^{-i(\mathbf{kr}+\phi(x))}. \tag{2.40}$$

In an *amplitude hologram*, we can assume $\phi = const$, whereas $\tau(x)$ varies over the hologram. If we assume that the resulting amplitude transmittance is linearly related to the intensity of the interference pattern, the amplitude transmittance of the grating can be written as

$$\tau(x) = \tau_0 + \Delta\tau \cos Kx, \tag{2.41}$$

where τ_0 is the average amplitude transmittance of the grating, $\Delta\tau$ is the amplitude of the spatial variation of $\tau(x)$ and

$$K = \frac{2\pi}{\Lambda}$$

is the grating wave-vector. Expanding the relation 2.41, equation 2.40 becomes

$$E(x, z) = E_0 e^{-ik_z z}\left[\tau_0 e^{-ik_x x} + \frac{\Delta\tau}{2}\left(e^{-i(k_x+K)x} + e^{-i(k_x-K)x}\right)\right]. \tag{2.42}$$

The diffracted field appears as the superimposition of three waves (diffraction orders), with wave-vector $\mathbf{k}_n$, propagating in three distinct directions and connected from a relation expressing the momentum conservation:

$$\mathbf{k}_n = \mathbf{k} + K\hat{\mathbf{x}}.$$

From equation 2.42, we find that the intensity of the first diffracted order is $|E_0|^2\left(\frac{\Delta\tau}{2}\right)^2$. Since $\tau(x)$ is limited to the range $[0, 1]$, the maximum value is reached for $\Delta\tau = 1/2$, that means the maximum amplitude in each of the diffracted orders is one fourth of incident amplitude, so that the peak diffraction efficiency is

$$\eta_{\max} = \frac{1}{16} = 6.25\%\,.$$

In a *phase hologram* we can assume $\tau(x) = 1$, so that the complex amplitude transmittance is $T(x) = e^{-i\phi(x)}$. If the phase shift produced by the recording medium is linearly proportional to the intensity in the interference pattern, we have

$$\phi(x) = \phi_0 + \Delta\phi \cos Kx,$$

and equation 2.40 becomes

$$E(x,z) = E_0 e^{-i\mathbf{kr}} e^{-i\phi_0} e^{-i\Delta\phi\cos Kx}. \tag{2.43}$$

The last factor can be expanded as a Fourier series,

$$e^{-i\Delta\phi\cos Kx} = \sum_{n=-\infty}^{\infty} i^n J_n(\Delta\phi)\, e^{inKx}$$

where J_n is the Bessel function of first species and order n. Introducing it into equation 2.43, it becomes

$$E(x,z) = E_0 e^{-ik_z z} e^{-i\phi_0} \sum_{n=-\infty}^{\infty} i^n J_n(\Delta\phi)\, e^{-i(k_x x - nKx)}.$$

Such a modulation diffracts the incident light into a large number of diffraction orders with intensity $|E_0|^2 J_n^2(\Delta\phi)$. According to the properties of the Bessel function, the maximum diffraction efficiency η is

$$\eta_{\max} = J_1^2(\Delta\phi) \simeq 33.9\%\,.$$

2.2.3 Thick Gratings: The Coupled-wave Theory of Kogelnik

In 1969, Herwig Kogelnik published the coupled wave theory [Kogelnik 1969], analyzing the diffraction of light by thick gratings. This theory can predict the maximum possible efficiencies of the various thick holograms. Let consider a coordinates system (see Figure 2.13) in which the z-axis is perpendicular to the surfaces of the recording medium and the x-axis is in the plane of incidence, while the fringe planes are oriented perpendicular to the plane of incidence. The grating vector $\mathbf{K}$ is perpendicular to the fringe planes forming an angle ψ with the z-axis:

- $\psi = 0°$ in transmission gratings;
- $\psi = 90°$ in reflection gratings.

The volume record of the holographic interference pattern usually takes the form of a spatial modulation of the absorption coefficient, or of the refractive index $n(\mathbf{r})$ of the medium, or both. For the sake of simplicity, here the analysis is restricted to the holographic record of sinusoidal fringe patterns (that is the typical irradiance distribution achievable by two-beam holography in a single-step process). The grating is assumed dielectric, non magnetic and isotropic (anisotropy will be discussed later on). Hence, once the recording process has taken place, the resulting modulation may be described at the first order by the following relations:

$$\begin{aligned} n &= n_0 + n_1 \cos \mathbf{K}\cdot\mathbf{x}, \\ \alpha &= \alpha_0 + \alpha_1 \cos \mathbf{K}\cdot\mathbf{x}, \end{aligned}$$

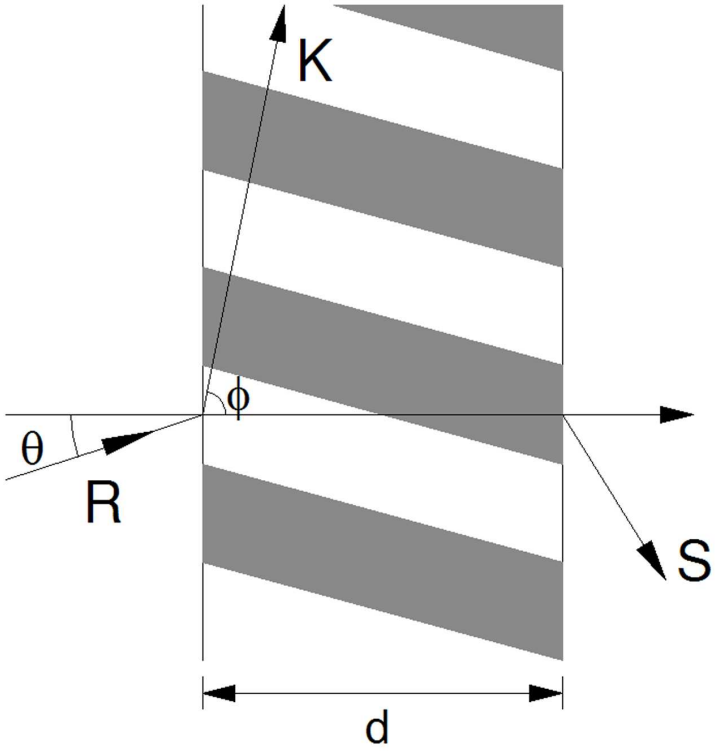

Figure 2.13: Model of a thick hologram with slanted fringes.

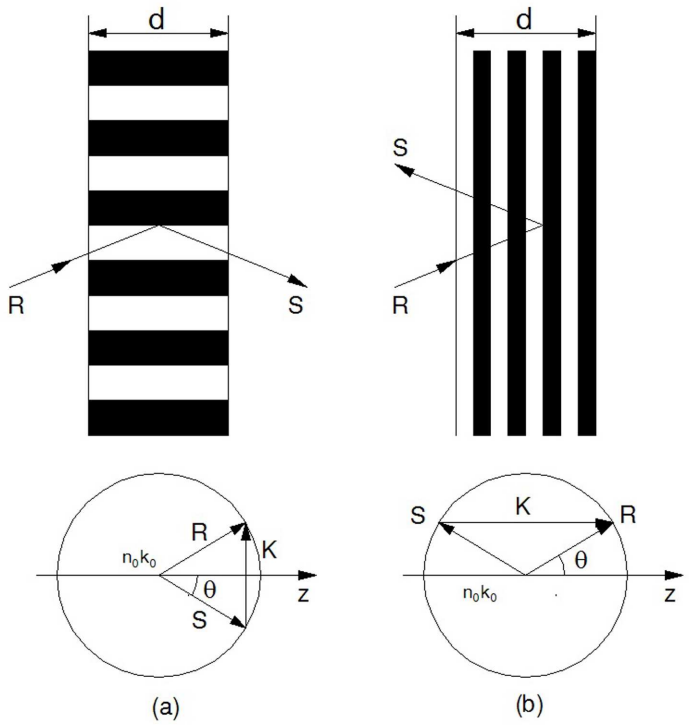

Figure 2.14: a) Volume transmission, b) reflection gratings and their associated vector diagrams for Bragg condition.

where $\mathbf{x}$ represents the radius vector $\mathbf{x} = (x, y, z)$; whereas n_0 is the average refractive index; α_0 is the average absorption coefficient; n_1 and α_1 are the amplitudes of the spatial modulations of the index and absorption coefficient, respectively. Let assume monochromatic light incident at (or next to) the Bragg angle. With regard to the light polarization, firstly let suppose s-polarized light (perpendicular to the plane of incidence). If the medium thickness is large enough, only two waves in the grating need to be taken into account: the incoming reference wave R and the outgoing signal wave S. Only these two waves obey to the Bragg condition, hence the other diffraction orders result severely attenuated and can be neglected. Wave propagation in the grating is described by the scalar wave equation

$$\nabla^2 E + k^2 E = 0 \tag{2.44}$$

where E is the complex amplitude $E(x, z)$ of the y-component of the electric field, which is assumed to be independent of y and to oscillate with an angular frequency ω; k is the spatially varying propagation constant in the grating, related to n and α. Let assume that the actual spectral absorption, as well as the relative variations in the refractive index of the medium, are small (reasonable approximations for the experimental situation) so that

$$\begin{aligned} n_0 k_0 &\gg \alpha_0 \\ n_0 k_0 &\gg \alpha_1 \\ n_0 &\gg n_1, \end{aligned}$$

where $k_0 = 2\pi/\lambda$ and λ represents the free-space wavelength. Under the above conditions, the propagation constant obeys to the relation

$$k^2 = \beta^2 - 2i\alpha\beta + 4\kappa\beta \cos \mathbf{K} \cdot \mathbf{x}, \tag{2.45}$$

where $\beta = n_0 k_0 = 2\pi n_0/\lambda$ is the average propagation constant and κ is the coupling constant, defined as

$$\kappa = \frac{\pi n_1}{\lambda} - i\frac{\alpha_1}{2}.$$

The coupling constant is the central parameter in the coupled-wave theory as it describes the coupling between the reference wave R and the signal wave S. If $\kappa = 0$, there is no coupling and, therefore, there is no diffraction. The amplitudes of the spatial modulations n_1 and α_1 correspond to a grating coupling the two waves R and S; they yeald to an exchange of energy between them. As a result of this energy interchange, or because of an energy loss from absorption, the complex amplitudes $R(z)$ and $S(z)$ vary along the z direction. The total electric field in the grating results in a superposition of these two fields:

$$E = R(z)e^{-i\rho\cdot\mathbf{x}} + S(z)e^{-i\sigma\cdot\mathbf{x}}, \tag{2.46}$$

where ρ and σ are the propagation vectors for the two waves. The quantity ρ is assumed to be equal to the propagation vector of the free-space reference wave as

the coupling is neglected, whereas σ, determined by the grating, is related to ρ and to the grating vector $\mathbf{K}$ by the expression

$$\sigma = \rho - \mathbf{K} \tag{2.47}$$

that describes the conservation of momenta. Figure 2.15a shows the vectors of interest and their orientation:

$$\rho = \begin{pmatrix} \rho_x \\ \rho_y \\ \rho_z \end{pmatrix} = \beta \begin{pmatrix} \sin\vartheta \\ 0 \\ \cos\vartheta \end{pmatrix}$$

$$\sigma = \begin{pmatrix} \sigma_x \\ \sigma_y \\ \sigma_z \end{pmatrix} = \beta \begin{pmatrix} \sin\vartheta - \frac{K}{\beta}\sin\psi \\ 0 \\ \cos\vartheta - \frac{K}{\beta}\cos\psi \end{pmatrix}$$

The vectorial relation 2.47 is shown in Figure 2.15: the general case is shown in Figure 2.15a, where the Bragg condition is not full filled; figure 2.15b shows the same diagram for incidence at the Bragg angle ϑ_0. In this special case, the magnitudes of both ρ and σ are equal to the free propagation constant $n_0 k_0$, and the Bragg condition, becoming

$$\cos(\psi - \vartheta_0) = \frac{k}{2n_0 k_0},$$

is satisfied.

Fixed the wavelength, the Bragg condition may be broken by angular deviations $\Delta\vartheta$ from the Bragg angle ϑ_0. Analogously, for fixed angle of incidence, detuning takes place for changes $\Delta\lambda$ with respect to the Bragg wavelength λ_0. Differentiating the Bragg condition, we obtain

$$\frac{d\vartheta_0}{d\lambda_0} = \frac{K}{4\pi n_0}\sin(\psi - \vartheta_0),$$

that relate the angular selectivity to the spectral selectivity of a thick hologram grating: small changes in the angle of incidence or the wavelength have similar effects. High performance devices, typically, should have a large selectivity and large diffraction efficiency. Kogelnik introduced the parameter of dephasing ζ for evaluating the effects of deviations from the Bragg condition (from equation 2.47):

$$\zeta \equiv \frac{\left(\beta^2 - \sigma^2\right)}{2\beta} = K\cos(\psi - \vartheta) - \frac{K^2}{4\pi n_0}\lambda. \tag{2.48}$$

A Taylor series expansion of equation 2.48 yields the following expression of ζ for small deviation $\Delta\vartheta$ and $\Delta\lambda$ from the Bragg condition,

$$\zeta = \Delta\vartheta K\sin(\psi - \vartheta_0) - \Delta\lambda\frac{K^2}{4\pi n_0}.$$

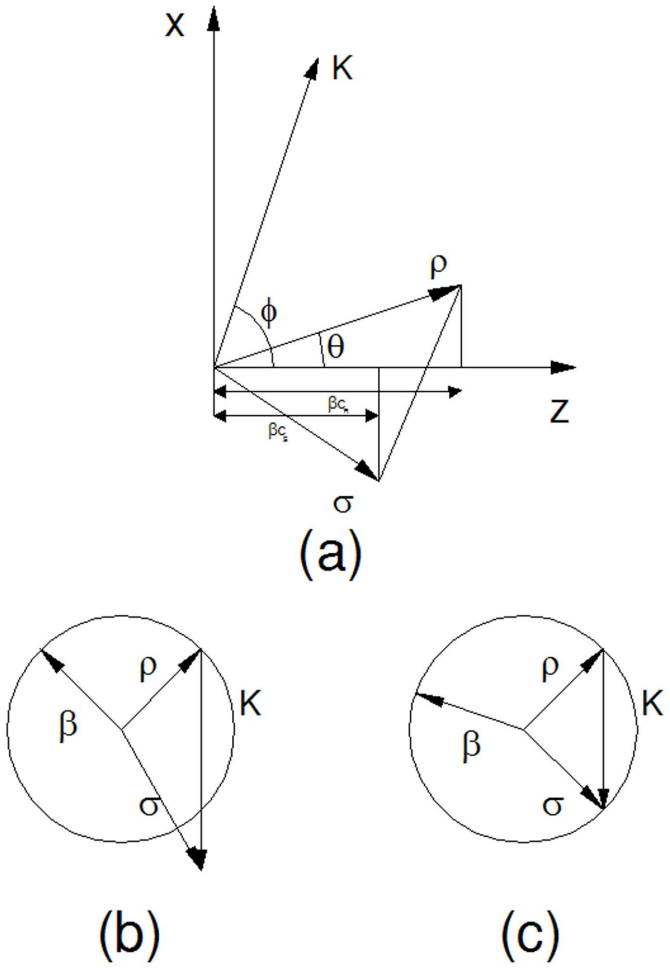

Figure 2.15: Vector diagrams: a) the relation between the propagation vector and the grating vector; b) conservation of the momentum near at the Bragg condition; c) conservation of the momentum for Bragg incidence condition.

The coupled-wave equations may be derived from equations 2.44 and **??**, after substitution of the relations 2.46 and 2.47. Comparing the terms involving equal exponentials ($e^{-i\rho\cdot\mathbf{x}}$ and $e^{-i\sigma\cdot\mathbf{x}}$) we obtain

$$\begin{cases} R'' - 2iR'\rho_z - 2i\alpha\beta R + 2\kappa\beta S = 0 \\ S'' - 2iS'\sigma_z - 2i\alpha\beta S + \left(\beta^2 - \sigma^2\right) S + 2\kappa\beta R = 0, \end{cases}$$

where the primes indicate differentiation with respect to z. Assuming small a small energy interchange between S and R, as well as for energy absorption in the medium, the second differentials R'' and S'' can be neglected [Kogelnik 1969]. The coupled-wave equation can be written in the form:

$$\begin{cases} c_R R' + \alpha R = -i\kappa S \\ c_S S' + (\alpha + i\zeta)\, S = -i\kappa R, \end{cases} \tag{2.49}$$

where c_R and c_S (see Figure 2.15) stand for the expressions

$$\begin{aligned} c_R &= \frac{\rho_z}{\beta} = \cos\vartheta \\ c_S &= \frac{\sigma_z}{\beta} = \cos\vartheta - \frac{K}{\beta}\cos\psi. \end{aligned}$$

The coupled-wave equations 2.49 show that the amplitude of a wave changes along z because of coupling to the other wave ($\kappa R, \kappa S$) or absorption ($\alpha R, \alpha S$). For deviations from the Bragg condition, S is forced out of synchronism with R, due to the dephasing term ζS and the interaction decreases.

The general solution of the coupled-wave equations is

$$R(z) = r_1 e^{\gamma_1 z} + r_2 e^{\gamma_2 z} \tag{2.50}$$

$$S(z) = s_1 e^{\gamma_1 z} + s_2 e^{\gamma_2 z}, \tag{2.51}$$

where r_i and s_i are constants which depend on the boundary conditions. If we insert equations 2.50 and 2.51 into 2.49, we find

$$\begin{cases} (c_R\gamma_i + \alpha)\, r_i = -i\kappa s_i \\ (c_S\gamma_i + \alpha + i\zeta)\, s_i = -i\kappa r_i. \end{cases} \tag{2.52}$$

The boundary conditions for a *transmission grating* are $R(0) = 1$ and $S(0) = 0$. From equations 2.50 and 2.51 it follows immediately that

$$\begin{cases} r_1 + r_2 = 1 \\ s_1 + s_2 = 0. \end{cases}$$

Combining these relations with equations 2.52, we find

$$s_1 = -s_2 = -i\frac{\kappa}{c_s\,(\gamma_1 - \gamma_2)}$$

obtaining the following expression for the amplitude of the outgoing signal:

$$S(d) = i\frac{\kappa}{c_s\left(\gamma_1 - \gamma_2\right)}\left[e^{\gamma_2 d} - e^{\gamma_1 d}\right].$$

This is a general expression valid for all types of thick transmission holograms including the case of off-Bragg incidence, lossy gratings and slanted grating. Further details may be found in [Kogelnik 1969].
For a *reflection grating* the boundary conditions are $R(0) = 1$ and $S(d) = 0$. Hence,

$$\begin{cases} r_1 + r_2 = 1 \\ s_1 e^{\gamma_1 d} + s_2 e^{\gamma_2 d} = 0 \end{cases}.$$

The relation for s_1 and s_2 can be written in the form

$$\begin{aligned} s_1\left[e^{\gamma_2 d} - e^{\gamma_1 d}\right] &= \left(s_1 + s_2\right)e^{\gamma_2 d} \\ s_2\left[e^{\gamma_2 d} - e^{\gamma_1 d}\right] &= -\left(s_1 + s_2\right)e^{\gamma_1 d}. \end{aligned}$$

Summing equations 2.52 for $i = 1$ and $i = 2$,

$$-i\kappa\left(r_1 + r_2\right) = -i\kappa = \left(s_1 + s_2\right)\left(\alpha + i\zeta\right) + c_S\left(\gamma_1 s_1 + \gamma_2 s_2\right),$$

we, finally, arrive at the result for the amplitude $S(0)$ of the outgoing signal of a reflection hologram,

$$S(0) = \left(s_1 + s_2\right) = -i\kappa\frac{1}{\alpha + i\zeta + c_S\frac{\gamma_1 e^{\gamma_2 d} - \gamma_2 e^{\gamma_1 d}}{e^{\gamma_2 d} - e^{\gamma_1 d}}}.$$

The diffraction efficiency η is defined as

$$\eta = \frac{|c_S|}{c_R} S S^*,$$

where S is the complex amplitude of the outgoing signal for a reference wave R incident with unit amplitude (S is equal to $S(d)$ for transmission holograms and equal to $S(0)$ for reflection holograms). In other words η describes the fraction of the incident light power that is diffracted into the signal wave. If the fringes are not slanted, that is $\psi = 0$ and $c_S = c_R$, the diffraction efficiency becomes

$$\eta = SS^* = |S|^2.$$

2.2.4 Volume Transmission Phase Gratings

In lossless phase gratings $\alpha_0 = \alpha_1 = 0$ and the coupling constant is $\kappa = \pi n_1/\lambda$. Diffraction is caused by spatial variation of the refractive index, the amplitude is then

$$S(d) = -ie^{-i\chi}\frac{\sin\sqrt{\Phi^2 + \chi^2}}{\sqrt{1 + \frac{\chi^2}{\Phi^2}}},$$

where

$$\Phi = \frac{\pi n_1}{\lambda}\frac{d}{\cos\vartheta} \text{ and } \chi = \frac{\zeta d}{2\cos\vartheta}.$$

At the Bragg angle $\zeta = 0$, so that $\chi = 0$ and

$$S(d) = -i\sin\Phi.$$

The diffraction efficiency is then

$$\eta = |S|^2 = \sin^2\Phi = \sin^2\frac{\pi\Delta n d}{\lambda\cos\vartheta}.$$

As the thickness d or the variation of the refractive index n_1 increases, the diffraction efficiency increases until the modulation parameter $\Phi = \pi/2$. At this point $\eta = 1 = 100\%$ (see Table 2.1) and all the energy goes into the diffracted light. When Φ increases beyond this point, the energy is back-coupled into the incident wave and η decreases.

If $\alpha_0 \neq 0$, that is the case of a lossy phase grating, the diffracted amplitude at the Bragg angle is

$$S(d) = -ie^{-\frac{\alpha_0 d}{\cos\vartheta}}\sin\Phi.$$

The additional exponential term decreases the maximum diffraction efficiency.

2.2.5 Volume Transmission Amplitude Gratings

In an amplitude grating we can assume $n_1 = 0$, whereas the absorption coefficient varies with amplitude α_1 around its mean value α_0. In this case, the coupling constant $\kappa = -i\alpha_1/2$, and the diffracted amplitude is

$$S(d) = -e^{-\frac{\alpha_0 d}{\cos\vartheta}}e^{-i\chi}\frac{\sinh\sqrt{\Phi_\alpha^2+\chi^2}}{\sqrt{1+\frac{\chi^2}{\Phi_\alpha^2}}},$$

where

$$\Phi_\alpha = \frac{\alpha_1 d}{2\cos\vartheta} \text{ and } \chi = \frac{\zeta d}{2\cos\vartheta}.$$

For incidence at the Bragg angle, $\chi = 0$ and the diffraction efficiency can be written as

$$\eta = e^{-\frac{2\alpha_0 d}{\cos\vartheta_0}}\sinh^2\frac{\alpha_1 d}{2\cos\vartheta_0}.$$

The diffracted amplitude increases with α_1, but since negative values of the absorption are excluded, $\alpha_1 \leq \alpha_0$. Therefore, the highest diffraction efficiency is obtained when $\alpha_1 = \alpha_0$, for $\alpha_1 d\cos\vartheta_0 = \ln 3$ (see Table 2.1),

$$\eta = \frac{1}{27} = 0.037 = 3.7\%\,.$$

2.2.6 Volume Reflection Phase Gratings

In reflection holograms the recorded fringe planes are parallel to the surfaces of the recording medium, and the signal appears as a reflection of the reference wave (see Figure 2.14). In a lossless phase grating $\alpha_0 = \alpha_1 = 0$ and the coupling constant is $\kappa = \pi n_1/\lambda$. The diffracted amplitude is given by the expression

$$S(0) = i\left[\left(i\frac{\chi_r}{\Phi_r}\right) + \sqrt{1 - \frac{\chi_r^2}{\Phi_r^2}}\coth\sqrt{\Phi_r^2 - \chi_r^2}\right]^{-1}$$

where

$$\Phi_r = \frac{\pi n_1 d}{\lambda\cos\vartheta} \text{ and } \chi_r = \frac{\zeta d}{2\cos\vartheta}$$

The diffraction efficiency can be written as

$$\eta = \left[1 + \frac{1 - \frac{\chi_r^2}{\Phi_r^2}}{\sinh^2\sqrt{\Phi_r^2 - \chi_r^2}}\right]^{-1}$$

For a wave incident at the Bragg angle, $\chi_r = 0$,

$$\eta = \tanh^2\frac{\pi n_1 d}{\lambda\cos\vartheta_0}$$

so it increases asymptotically to $\eta = 1 = 100\%$ (see Table 2.1) as the value of Φ_r increases.

2.2.7 Volume Reflection Amplitude Gratings

Finally, let consider $n_1 = 0$, whereas α_1 and α_0 are finite. The amplitude of the diffracted wave is then

$$S(0) = -\left[\frac{\chi_{r\alpha}}{\Phi_{r\alpha}} + \sqrt{\left(\frac{\chi_{r\alpha}}{\Phi_{r\alpha}}\right)^2 - 1}\coth\sqrt{\chi_{r\alpha}^2 - \Phi_{r\alpha}^2}\right]^{-1},$$

where

$$\Phi_{r\alpha} = \frac{\alpha_1 d}{2\cos\vartheta} \text{ and } \chi_{r\alpha} = \frac{\alpha_0 d}{\cos\vartheta_0} - i\frac{\zeta d}{2\cos\vartheta_0}.$$

If the incident wave is at the Bragg angle, $\zeta = 0$ and $\chi_{r\alpha}/\Phi_{r\alpha} = 2\alpha_0/\alpha_1$, so

$$S(0) = -\left[\frac{2\alpha_0}{\alpha_1} + \sqrt{\frac{4\alpha_0^2}{\alpha_1^2} - 1}\coth\left(\frac{d}{\cos\vartheta_0}\sqrt{\alpha_0^2 - \alpha_1^2/4}\right)\right]^{-1}.$$

When the modulation is maximum, $\alpha_1 = \alpha_0$ and the maximum diffraction efficiency is (see Table 2.1)

$$\eta = \frac{1}{\left(2 + \sqrt{3}\right)^2} = 0.072 = 7.2\%\,.$$

	Modulation	
Type	Phase	Amplitude
Thin Transmission	33.9%	6.25%
Volume Transmission	100%	3.7%
Volume Reflection	100%	7.2%

Table 2.1: Maximum theoretical diffraction efficiency for different types of grating

2.2.8 Validity of the theory

The maximum diffraction efficiencies acbievable with the six types of gratings studied are summarized in Table 2.1.

Kogelnik's coupled-wave theory is applicable under several assumptions that makes the analysis possible: the spatial modulation of the refractive index and the absorption coefficient is sinusoidal; there is as a slow energy interchange and only a small absorption loss per wavelength between the two coupled waves; there is the same average index for the region inside and outside the gratings boundaries (otherwise there is a reflection and transmission contribution at the boundaries following the Snell law); incident light is near at the Bragg angle; only two diffraction orders are retained in the analysis (satisfying Bragg condition exactly or approximately). The results here shown (for $s-$polarized light) can be easily be applied to the case of a $p-$polarized incident light (parallel to the plane of incidence) [Kogelnik 1969], substituting the new expression

$$\kappa_{\shortparallel} = -\kappa \cos 2\left(\vartheta_0 - \psi\right)$$

for the coupling constant κ in the equations above.

More accurate approximations for the theory of diffraction gratings in the case of volume holograms may be found in [Gaylord 1985]. It can be demonstrated that the conditions to be fullfilled for thick gratings are:

$$Q = \frac{K^2 \lambda d}{2\pi n} > 1$$

and

$$\nu = \frac{\lambda^2}{\Lambda^2 n \sigma} \geqslant 10,$$

where $\sigma = \Delta n$ for dielectric gratings and $\sigma = \Delta\alpha\lambda/2\pi$ for absorption gratings. If the two conditions aforementioned are not strictly fullfilled, then the behavior of the diffraction grating may be intermediate between the Bragg and Raman-Nath regimes: in this case a numerical approach must be used.

The coupled-wave theory is widely used to describe thick isotropic gratings. However, an extension of the theory to optically anisotropic materials is needed in the case of a strong polarization dependent behavior or when more accurate results are desired. In fact, the Bragg diffraction is strongly affected by the optical

anisotropy. The main reason lies in the difference between the energy propagation direction and the wave-front normal. The advent of materials with strong birefringence in the fabrication of volume diffraction gratings, such as liquid crystals, ordered polymers or organic crystals, requires generalization of Kogelnik's theory. This was done, as for instance, by Montemezzani and Zgonik in 1997 [Montemezzani 1997]. However, here we won't enter into details of this theoretical model. In fact, the diffraction gratings analyzed in this thesis will be volume transmission phase gratings in which the refractive index modulation is achieved by means of a modulation of the relative concentration of two components: the liquid crystals droplets and polymeric matrix in which the first are embedded (see 2.1.6 and 2.1.8). Due to the dynamics of the grating formation in the optical curing process, the anisotropic component, that is the LC droplet, is usually isotropically oriented into the grating volume and, hence, the average effect is only a refractive index modulation given by the optical contrast (between the average refractive index of the LC droplet and the polymer index) modulated with the concentration variation (details are discussed in the next section).

2.3 1-D Diffraction Gratings in Soft Matter

In this thesis I will present several 1-D diffraction gratings realized with soft matter and produced with a novel single-beam technique based on Computer-generated holography and spatial light modulation (see 1.2). In this section I want to introduce the consolidated technology of soft matter-based one-dimensional gratings that I used for the fabrication of not only 1-D, but also 2-D and 3-D structures, obtaining interesting and original results. I will also discuss, briefly, the typical interference-based technique of two-beam holography, that will result useful for the comprehension of some basic elements and principles of the new fabrication approach explored in this thesis.

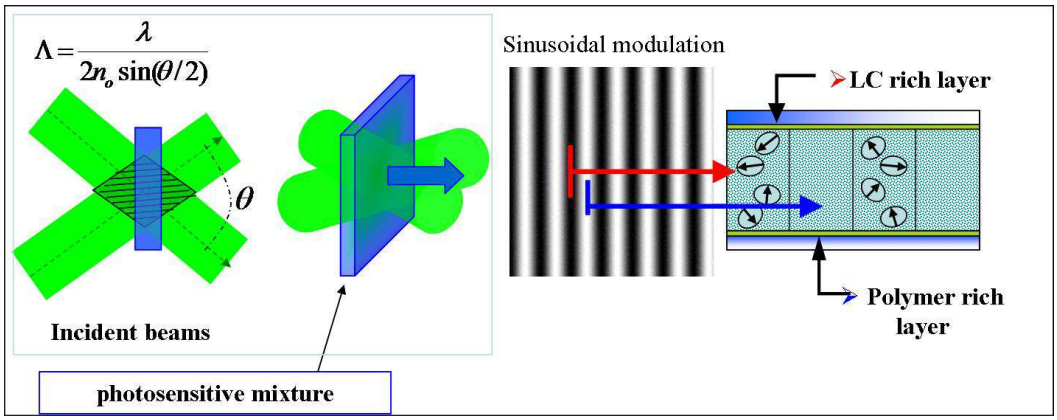

Figure 2.16: Scheme of a two-beam interference inducing a typical H-PDLC grating.

Liquid crystal-polymer composites are suitable media for holographic recording. The first holographic LC-polymer gratings, better known as holographic-PDLCs (H-PDLCs), were realized by Sutherland et al. in 1993 [Sutherland 1993]. H-PDLCs are produced by curing, under a laser interference pattern, an isotropic photosensitive liquid mixture of pre-polymeric material and liquid crystal. The result of the recording process, based on an inhomogeneous polymerization effect, is a grating consisting of a periodic distribution (due to the periodicity of the interference irradiance) of small LC droplets embedded in a polymeric matrix, as schematically represented in Fig. 2.16: layers of LC droplets (LC rich regions), with higher concentrations and larger radii, are found in correspondence of the dark fringes of the curing pattern; homogenous polymer slices (polymer rich regions), possibly containing a small amount of non phase separated LC (with smaller radii), in correspondence of the bright fringes. Because of the difference in the refractive index between the polymer and the randomly oriented droplets, the spatial modulation of the LC content produces a modulation in the average refractive index. The resulting optical phase grating can be easily switched off by applying an external voltage, as depicted in Fig. 2.17: the droplet directors $\hat{\mathbf{n}}$ (along with the molecules have an extraordinary index n_e) align themselves along the electric field $\mathbf{E}$ (in the case of a positive dielectric anisotropy, as discussed in 2.1.6) and the refractive index modulation disappears, provided that the polymeric index n_p is chosen to match the droplet ordinary refractive index $n_o \simeq n_p$. However, the main structural features (i. e. degree of phase separation, LC alignment inside the droplets, droplet size, shape and orientation) influence the optical properties of the gratings. These are dependent on the production parameters of the fabrication process, that are the physical and chemical properties of each single component, their concentration in the initial mixture, the curing parameters (light intensity, exposure time, sample temperature), and sample geometry (grating spacing and thickness) [Veltri 2004].

H-PDLCs are very attractive for many different optical applications. Their major reason of interest is evidently connected with the electrical (or even thermal) control of the diffractive properties. In addition, H-PDLCs can reach very high diffraction efficiencies (over 90%) and show relatively fast response times (few milliseconds or even less) [Bunning 2000]. Furthermore, the scattering losses are very low if compared to ordinary PDLCs [Simoni 1997]. Indeed, the average dimension of LC droplets in H-PDLC gratings falls well into the submicron range (typically $\sim 100nm$), whereas is about few microns in PDLCs. Finally, another appealing feature of H-PDLCs is their simple and flexible production technique: with a standard holographic set-up and a fast one-shot exposure both refraction and transmission gratings can be realized, with grating spacings varying from many microns down to few hundreds of nanometers. The materials used in the photo-sensitive mixture are cheap and well known to the industry in a profusion of different varieties, permitting an accurate tailoring of all the main chemical and physical properties.

Recently, two new variants of H-PDLCs, characterized by a complete separation of the LC phase, have been independently developed. Umeton's group at the University of Calabria (Cosenza, Italy) first patented what they called *POLICRYPS*

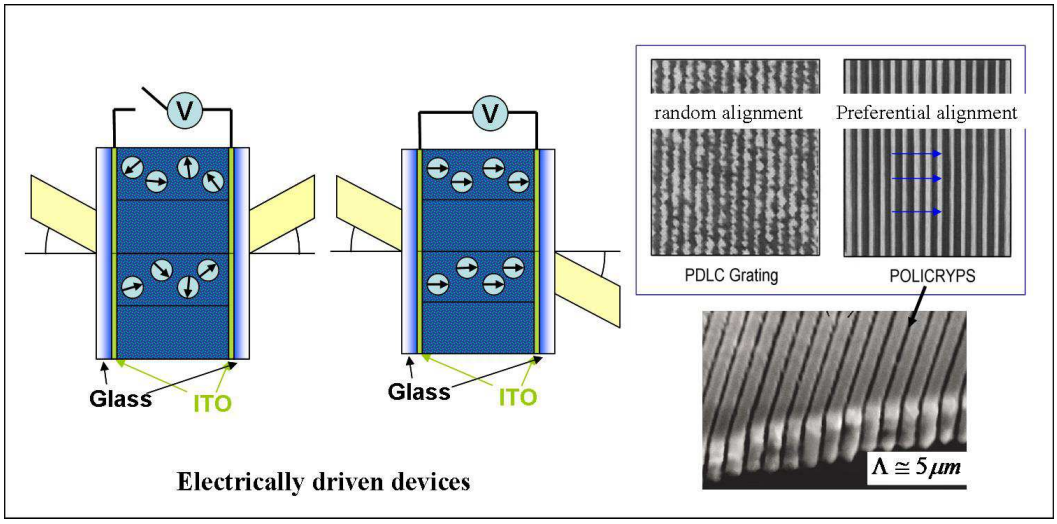

Figure 2.17: Active holographic grating scheme (left); polarizing microscope images of typical experimental gratings achievable: H-PDLC and POLICRYPS structures (inset: detail by SEM image).

(polymer - liquid crystal - polymer slices) gratings [Caputo 2005]. Few years later Stumpe's group at the Fraunhofer Institute for Applied Polymer Research (Postdam, Germany) presented a patent for the somehow similar *Poliphem* (polymer - liquid crystal - polymer holograms electrically manageable) gratings [Sakhno 2004]. In both types of gratings the droplet nucleation is inhibited so that their morphology simply consists of alternate homogeneous films of polymer and liquid crystal. This peculiar microscopic structure affects the grating macroscopic properties in many positive ways, as it will be discussed later on. In the SEM (Scanning Electron Microscopy) images of Fig. 2.17 the difference between a H-PDLC and a POLICRYPS grating of similar pitch is shown: the latter shows a very homogenous structure in which a total phase separation between the liquid crystal and the polymer is evident. It is worth noticing, here, that the anisotropic behavior of the LC content can be neglected also in POLICRYPS (for which this approximation is even better), provided that intermediate states between off- and on-state, during the very fast transient, are not considered.

2.3.1 Production Procedure and Two-beam Holography

Although the writing intensity pattern is produced with the CGH-SLM technique developed in this thesis instead of other holographic approaches, the optical curing process and the structure formation are common to all the holographic techniques. Materials, sample preparation, formation dynamics and morphology are now described. Information provided comes from the experience developed during this work, complemented with several interesting published data; a very useful review

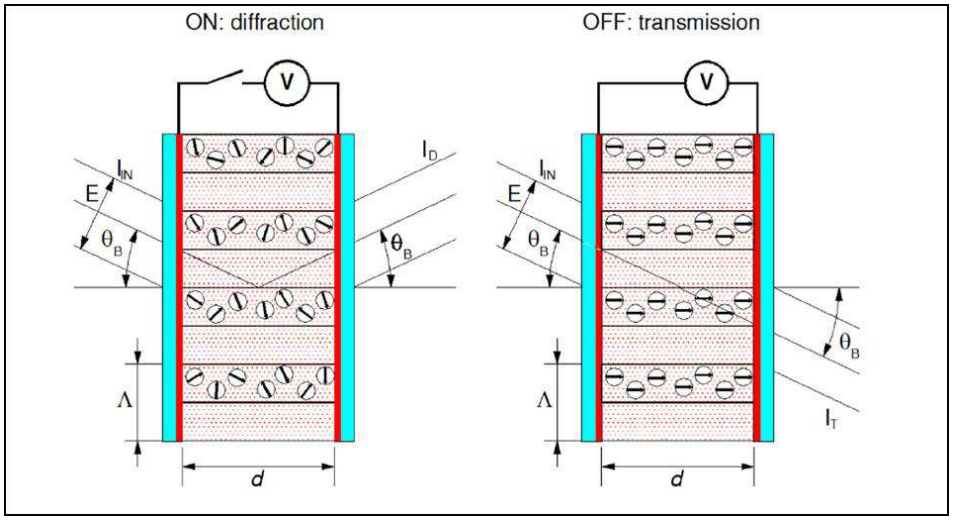

Figure 2.18: Schematic representation of H-PDLC transmission gratings.

on these topics is [Bunning 2000]. Information given for H-PDLCs are generally valid for all kinds of LC-polymer gratings realized in this work.
H-PDLC gratings have been widely produced with a typical holographic apparatus; a general scheme is shown in Fig. 2.19. As in all holographic applications, the mechanical stability of the optical table and the absence of any source of vibrations are crucial, especially when working on small length scales (spacings $\lesssim 0.5\mu m$). Anyway, this drawback is completely alleviated by CGH-SLM technique as discussed in 3.1. A laser is used as coherent light source; its wavelength must fall into the mixture sensitiveness region, typically in the ultraviolet (UV) or blue-green range. In most cases, the UV or visible lines of an Ar-ion laser $(351, 476, 488, 514nm)$ or the second harmonic of a Nd:YAG laser $(532nm)$ are used (this is the case for CGH-SLM technique). The laser beam, after being spatially filtered and expanded (plane wave approximation) is divided into two beams of equal power. By means of mirrors, the two branches are recombined over the sample (see Fig. 2.16), producing a 1-D interference pattern whose intensity profile $I(x)$ inside the sample is given by

$$I = (I_1 + I_2)[1 + V\cos(\frac{2\pi}{\Lambda}x)], \tag{2.53}$$

where the visibility of the fringes V has been defined as

$$V = \frac{2\sqrt{I_1 I_2}}{I_1 + I_2}, \tag{2.54}$$

whereas the grating pitch Λ of the interference is related to the free-space wavelength λ and to the average refractive index n of the sample mixture by

$$\Lambda = \frac{\lambda}{2n\sin(\theta/2)}, \tag{2.55}$$

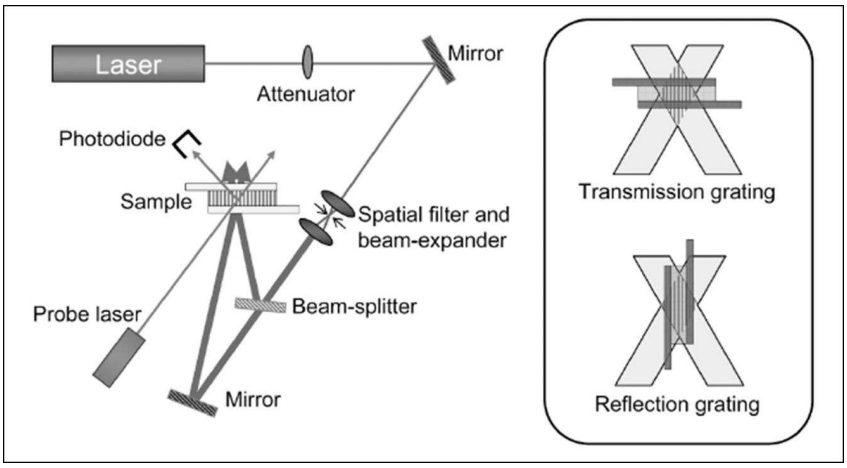

Figure 2.19: Holographic set-up for grating recording and real-time measurement of the diffraction efficiency (main picture). The grating geometry, in transmission or in reflection, is fixed by the sample orientation with respect to the interference pattern (inset).

in which the angle θ between the incoming beams usually represents the unique experimental variable.

A typical H-PDLC sample consists in a small amount of photosensitive syrup, sandwiched between two ITO (Indium Tin Oxide) coated glass slabs (see Fig. 2.17). If the syrup is fl uid enough, it can be injected into the pre-assembled cell by capillarity; if necessary, operation can be done at an increased temperature. In general, the glass slabs do not undergo any special treatment, apart from an accurate cleaning; in particular, no alignment layer is used. The sample thickness d, usually in the range of $(5 - 50\mu m)$, is set by MYLAR spacers placed at the sides of the cell or by silica spacers.

The main parameters involved in the curing process are the writing beam intensity and the exposure time. Typical values are respectively $10 \div 100 mW/cm^2$ and $30s \div 5min$. However, a still wider variation is reported in literature depending on the adopted mixture; in general optimum values have to be found empirically. Usually a second laser, with low intensity and a wavelength well outside the monomer sensitiveness range, e.g. a He-Ne laser, is used to monitor the grating growth. The probe beam impinges on the sample at the correspondent Bragg angle and the power of the outgoing diffracted beam is measured by a photodiode. This real time measurement is important to stop the curing when the highest diffraction efficiency is reached.

According to the method described above, H-PDLC recording appears straightforward. However, some care is needed to realize high quality gratings, particularly with regard to some issues. Most H-PDLC gratings have to undergo high voltages (even over $20V/\mu m$) to be switched. Ionic impurities remained not reacted at the

end of the curing process may diffuse under the effect of the electric field, heating the sample, short-circuiting the electrodes and eventually damaging the grating. Resolution and grating quality. As a general rule, shorter is the grating pitch, greater is the influence of vibrations. Reductions over $100 \div 200nm$ are made difficult by the intrinsic molecular resolution of the polymer. Moreover, a vibration-free curing leads to neater separation between the polymer-rich and the LC-rich regions. That is one of the reasons why, in my opinion, the CGH-SLM technique provides high quality gratings: because the writing beam is free from vibrations.

2.3.2 Sample Preparation

A typical H-PDLC syrup contains the following components: monomer (prepolymer), liquid crystal, photo-initiator, and other optional additives, thoroughly mixed into a homogenous solution under darkroom conditions. The main features concerning the different components are now discussed.

Component	**Typical Concentration** (w/w)
Monomer	$30\% \div 60\%$
Liquid crystal	$30\% \div 50\%$
Photo-initiator + co-initiator	$\lesssim 1\% \div 2\%$
Reactive solvent	$5\% \div 30\%$ (usually $\sim 10\%$)
Surfactant	$5\% \div 10\%$ (optional)

Table 2.2: Typical component concentrations in a H-PDLC mixture.

Monomers are the main component of H-PDLC mixtures, with a typical weight concentration of $30 \div 60\%$ (Tab. 2.2). Usually, multifunctional monomers that undergo a free radical addition polymerization are used, because of their fast growth rate. A fast polymerization and a highly cross-linked network are important to get very small LC droplets (typically $\sim 100nm$) and, consequently, a negligible light scattering. Two monomer parameters are particularly important in this regard: functionality, i.e. the number of C-C double bonds, and viscosity, which is related to the monomer molecular weight. Some studies on the monomer functionality [Pogue 2000] [DeSarkar 2003] have shown that the higher is the monomer functionality, the larger are the amount of phase separated LC, the average droplet size, and the anisotropy of the LC domains.
Other important factors to be considered are: high miscibility with liquid crystal in the monomer state and poor miscibility in the polymer state, chemical inertness with liquid crystal, existence of suitable photoinitiators, good optical properties (transparency and refractive index), good adhesion to the substrates, elasticity (to improve the electro-optical properties), and mechanical stability.
Among monomers, the most widely used in H-PDLC applications is the *dipentaerythritol hydroxy pentaacrylate* (DPHPA). A different class of monomers are the commercially available Norland Optical Adhesives (NOA), photosensitive mixtures

of polyfunctional thiols and allenes. They are characterized by a slower curing rate and generally need a high intensity exposure ($> 100 mW/cm^2$) in order to obtain small droplets. However, they are not much suitable for visible curing. These drawbacks have generally limited the use of these polymers as H-PDLC materials. However, NOA resins also own a number of interesting features (reduced shrinkage, less viscosity, better adhesion and elastic properties reducing the switching voltage). Recently, a mixture of NOA-65, $BL037$ liquid crystal ($30\% w/w$) and Irgacure 1173 (UV initiator) ($0.1\% w/w$) has been successfully exploited to produce reflection H-PDLC gratings [Natarajan 2003]. Most interestingly, NOA resins are the monomer used to produce both types of non-droplet gratings: POLICRYPS [Caputo 2005] and POLIPHEM [Sakhno 2004].

Liquid crystals used in H-PDLC gratings are in large majority nematics liquid crystals, with a positive dielectric anisotropy. They enter the H-PDLC syrup in a $30\% \div 50\%$ weight fraction (Tab. 2.2). The choice of the liquid crystal is connected with a number of chemical and physical parameters: miscibility in the monomer and immiscibility in the polymer; high dielectric anisotropy and low rotational viscosity, to obtain low switching voltages and fast response times; high birefringence, to get high refractive index modulation, hence high diffraction efficiency, and an ordinary refractive index matching the polymer refractive index, to achieve a good transmission state (off state of Fig.2.18); finally, a wide nematic range, to guarantee a stability with temperature. Two main families of nematic LCs, both provided by Merck, have been used in this thesis work for HPDLCs, as well for more complex structures (as discussed later on): the first one, known as BL-series and including the very common $E7$ and $CB5$, consists of mixtures of cyanobiphenyls and higher aromatic homologues; the second one, known as TL-series, are mixtures of chloro and fluoro substituted mesogens. TL-series LCs are transparent in the UV, show better electrical properties, but have a limited solubility in monomers.

In order for the polymerization reaction to take place, monomers need to react with free radicals. Photoinitiators (PIs) are molecules producing free radicals when exposed to light. Usually a small amount, $\lesssim 1\% \div 2\%$ by weight (Tab. 2.2), is enough to trigger the polymerization reaction. Two main mechanisms are possible: one, in which photon absorption induces the split of the PI molecule into two free radical molecules, and another one, which also involves a co-initiator (CI) molecule. In this case, the photoinitiator, excited by photon absorption, reacts with the coinitiator, which is an electron donor; the reaction results in the CI radical production. This kind of process has been the main optical curing method exploited for the fabrication of the structures produced with the CGH-SLM technique in this work.

A good photoinitiator must show high absorption at a suitable laser wavelength. Usually, two main wavelength ranges are used, one in the UV and another one in the blue-green region of the visible spectrum. In the case of visible curing, the initiator system used in this work has been the PI-CI combination of Rose Bengal (RB) and N-Phenyl Glycine (NPG). Figure 2.20 shows their absorption spectra. In particular, rose bengal shows a strong absorption peak around $550nm$, well suitable for green light laser curing (the $532nm$ Nd:YAG second harmonic have been used).

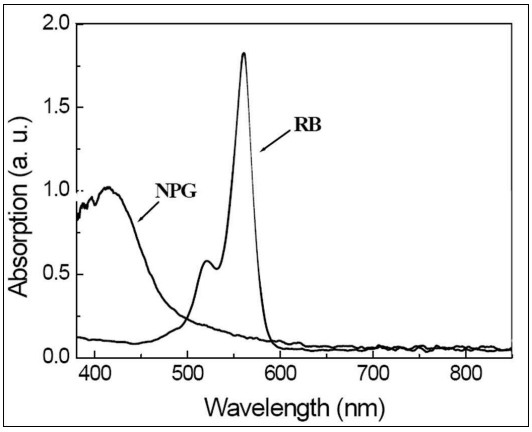

Figure 2.20: Rose Bengal (RB) and N-Phenyl Glycine (NPG) absorption spectra.

In almost all acrylate-based H-PDLC recipes, N-vinyl pyrrolidinone (NVP) is added to the mixture as reactive diluent, usually in a 10% weight fraction (Tab. 2.2). NVP is needed to decrease the monomer viscosity and obtain a homogeneous mixture with liquid crystal and photoinitiator. However, NVP is a mono-functional monomer, even though characterized by a low reactivity, so can play a role in the polymerization process, terminating the free-radical addition reaction and limiting the size of the polymer chains. Moreover, because of its high affinity for oxygen, increasing the NVP concentration can result in reducing the inhibition effect of oxygen, thus enhancing the gelation rate. Experimentally, an increased amount of NVP produced smaller and more isotropic droplets, thus reducing the scattering losses.

In H-PDLCs the average dimension of LC droplets is usually done as small as possible ($\lesssim 100nm$) in order to reduce the light scattering. The drawback is that the smaller are the LC domains, the larger is the field needed to reorient the droplet director and switch the grating off. Experimentally, the addition of surfactant to the photosensitive mixture has proved to significantly reduce the switching field (up to 75% lower). Non reactive long chain aliphatic acids, namely octoanoic acid, have been added at this purpose in a 10% weight concentration (Tab. 2.2) in a few cases. These molecules operate at the polymer-LC interface and reduce the surface anchoring of the nematic droplets. Nevertheless, the role of this component has not been yet clarified completely in this work. Further research is needed.

2.3.3 Formation Dynamics

The mechanisms involved in the grating formation are directly connected with the grating morphology and, hence, with the final optical and electro-optical properties of H-PDLCs. The main experimental approach to the problem is the real-time measurement of the diffraction efficiency during the optical curing. The sample is illuminated with a probe laser source (at $632nm$) so that the diffraction efficiency

may be monitored real-time by measuring the diffracted light at the expected Bragg angle with a photodiode. A growth in the diffraction efficiency corresponds to a growth of the refractive index modulation, indicating the appearance of a diffraction grating. The theory of the complex formation dynamics is beyond the scope of this thesis. Even though a full comprehension of the process is still far to be reached, a brief and general account on the topic is necessary to better understand the relations between curing parameters and morphology, as well as the difference between ordinary H-PDLCs and non-droplet gratings. In general, the real-time measurement of the diffraction efficiency shows the following three-stage structure:

1. The first stage consists in a short inhibition period, the exposure does not produce any refractive index modulation due to the presence of unwanted inhibitors, like oxygen or other molecules (that avoid the unintentional polymerization).

2. When all the inhibitors have reacted, the polymerization begins and a measurable diffraction efficiency is experienced.

3. Under a prolonged exposure, the diffraction efficiency reaches a steady state or start to decrease, due to the onset of strong scattering losses (LC droplets become larger) and to an excessive refractive index modulation, drawing the grating to the overmodulation regime ($\Phi > \pi/2$), as discussed in Sec. 2.2.4.

The polymerization begins and proceeds faster in the highly irradiated regions (bright regions). Consequently, in proximity of those areas the local concentration of monomers decreases, due to the monomer consumption, while the local LC concentration increases, due to the LC molecules reduction as expelled by the polymer network. As a result, a monomer diffusion from the dark to the bright areas and a LC counter-diffusion in the opposite direction occur. Obviously, the diffusion/counter-diffusion rates decrease as the polymer network is growing, until the polymer gelation prevents any further diffusion and fix a configuration in which polymer rich regions (in the bright areas) are separated by LC rich regions (in the dark areas), as shown in Fig. 2.16. Here the high local concentration of LC and the low solubility of the LC in the polymer cause the liquid crystal to phase separate in the form of nematic droplets. Usually, first an isotropic concentration of the with no modulation grating appears, and only later the droplet formation gives rise to a phase-modulated grating. Controlling the onset of the phase separation is crucial to determine the final morphology of the grating. By acting on the phase-separation dynamics is possible to achieve a non-droplet grating, as discussed in the sext section. On the other hand, also the writing pattern may have an important role in deciding the morphologic properties of a grating. After polymerization has occurred, usually, a shrinkage of the polymeric stripes is evident due to larger strength of the molecular bindings in the polymer. Consequently, the gratings may present a non symmetric but periodic dielectric modulation (even if irregularities may be present). This problem can be faced by employing not equally parted monomer-LC mixtures. CGH-SLM technique, instead, may provide asymmetric intensity patterns in order to compensate

the problem of shrinkage, as actually have been done in this work. Moreover, in the one-dimensional structures produced with the CGH-SLM technique, the behavior we verified may be considered intermediate between an H-PDLC and non-droplet grating. That is why, in the next section, I will introduce the characteristics of POLICRYPS in order to provide a better comprehension of the phenomenological aspects of the structures realized in this thesis.

2.3.4 Non-droplet Gratings

The approach proposed by Umeton's [Caputo 2005] and Stumpe's [Sakhno 2004] groups is based on developing LC-polymer gratings in which the formation of LC droplets is completely avoided. Of particular interest is the realization of gratings integrated in planar waveguides, in order to realize different kind of photonic devices. Although POLICRYPS and POLIPHEM are realized according to different patented procedures, they share the same peculiar morphology: a periodic stack of homogeneous LC films and polymer layers, sharply separated from each other, as schematically shown in Fig. 2.21. Such non-droplet structure affects the grating

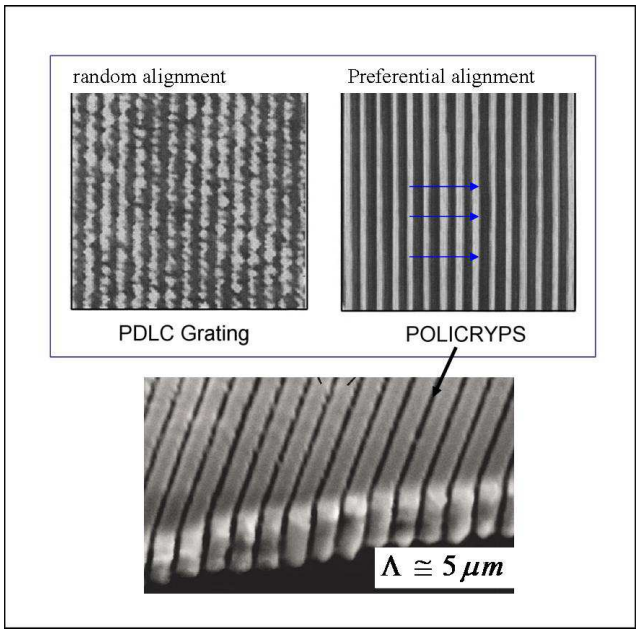

Figure 2.21: Polarizing microscope images of H-PDLC and POLICRYPS gratings [Caputo 2004].

properties in many positive ways: the scattering losses are strongly reduced, due to the absence of incoherent reflections, in both transmission and diffraction state; the switching voltage is much lower, as the dimension of the LC domains is not fixed by the droplet size but by the grating spacing; higher refractive index modulations are achievable, hence higher diffraction efficiencies can be obtained with the same

grating thickness. Moreover, these gratings manifest a behavior strongly dependent on the light polarization. As a matter of fact, they only work with p-polarized light. This can be well understood observing the picture in Fig. 2.21. The LC molecules align themselves orthogonally to the polymer slices, unless an electric field is applied across the cell. Because the polymer and the LC ordinary and extraordinary refractive indices (respectively n_p, n_o and n_e) are chosen in such a way that $n_p \simeq n_o < n_e$, incident p-polarized light experiences an index modulation and is thus diffracted. When an electric field is applied, LC director reorients, still remaining in the plane of incidence; eventually, for a certain angle, the effective LC refractive index (Eq. 2.34) experienced by p-polarized light matches the polymer index and diffraction is no more observed. Conversely, an s-polarized beam does not experience any index modulation across the cell, both with and without electric field.

The basic idea behind POLICRYPS gratings is to prevent the formation of the nematic phase during the curing process. This result is accomplished by heating the sample over the nematic-isotropic transition temperature, while the curing takes place. Indeed, the diffusion of liquid crystal molecules is much easier when they are in the isotropic phase; as a consequence an almost complete redistribution of LC and monomer can be obtained. At the end of the process, the grating is slowly cooled down to the room temperature, permitting a complete and uniform alignment of the liquid crystal director and achieving a highly ordered structure. In Fig. 2.21 a POLICRYPS observed under a polarizing optical microscope is compared with a standard H-PDLC grating with the same spacing and prepared by the same materials: the difference in sharpness and resolution is striking. Microscope observation of gratings between crossed polarizers also provides a direct verification of the LC alignment inside the sample. Besides the high curing temperature, Norland resins also play an important role in determining the special morphology of the POLICRYPS. Indeed, due to the NOA delayed gelation point, LC molecules are not constrained in small droplets, but can coalesce to form large regular mono-domains.

Differently, POLIPHEM are cured at room temperature. Here the special mono-domain morphology is the result of an accurate and specific choice of curing regime and syrup components [Sakhno 2004].

The crucial role of these kind of structures suggests the importance of the new technique developed in this work that permitted to achieve novel kind of structures with the typical features of the aforementioned non-droplet gratings.

2.4 Photonic Crystals

2.4.1 A brief Introduction to Photonic Crystals

Photonic Crystals (PhCs) represent a novel and very important technology for the fundamental study of physical phenomena (as for instance the superprism effect [Serbin 2006]) like the control of light propagation and emission in 1-D, 2-D and 3-D dielectric structures (Fig. 2.22) and for the realization of miniaturized devices like integrated optical interconnections with high curvature and low losses, optical

transistors, low threshold lasers, electromagnetic cavities, optical fibers with low core index, biological sensors, wave-guides, power divisors, narrow band filters for Wavelength Division Multiplexer (WDM), Light Emission Diod (LED) with high external efficiency and mirrors with very high reflectance (see [Joannopoulos 1995] and also [Verlag 2009]). See also [Chan 2005] for details of fabrication with holographic lithography. Telecommunications devices have reached higher performances

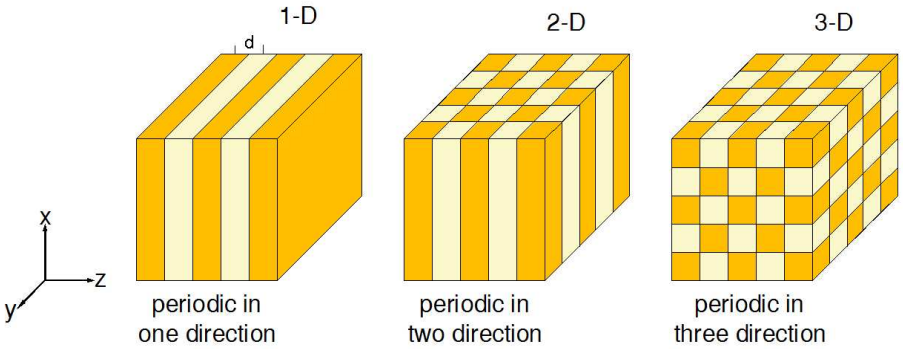

Figure 2.22: Simple examples of one-, two, and three-dimensional photonic crystals. The different colors represent materials with different dielectric constants.

by the employment of photonic circuits because they permit to process a huge quantity of data very fast. The advent of PhCs permits to increase further and further the achievable potential thanks to the better integration possibilities, comparable to the VLSI technology of semiconductors, on a micrometer and sub-micrometer scale.

In 1987, Yablonovitch, in a novel work about the control of light emission in LEDs, demonstrated the possibility of altering and controlling the properties of propagation and confinement of light by means of periodic dielectric structures able to induce, under suitable conditions, the formation of a Photonic Band-Gap (PBG) among the allowed propagation states in the crystal (see [Yablonovitch 1987]). Because of the periodic arrangement of its atoms and molecules, a crystal presents a periodic potential to an electron propagating through it. The lattice might introduce band-gaps into the energy structure of the crystal, so that electrons are forbidden to propagate with certain energies in certain directions. In analogy a band-gap may appear in the spectrum of propagating electromagnetic modes in periodic structures, in which the periodic *potential* is due to a lattice of macroscopic dielectric media instead of atoms. Let us consider, as for instance, a periodic structure in which the period is given by alternated low and high homogenous dielectric regions. If the dielectric contrast is large enough, then it will be possible that propagation is forbidden in a frequency range and for certain directions, giving rise to a complete band-gap if any direction is prohibited for TE (transverse electric) or TM (transverse magnetic) polarization. A photonic device already in common use is the *quarter wave-stack*: a mirror composed of alternating layers of different dielectric materials capable to maximize the width to mid-gap ratio $\Delta\omega/\omega_m$ up to $\sim$ 70%.

Light of the proper wavelength is scattered at the layer interfaces and the multiply-scattered waves may interfere destructively inside the material, and the light is almost completely reflected. In other words, the structure is a 1-D PhC and propagation is forbidden at certain wavelengths, causing reflection, because these fall into the photonic band-gap. As well as the stack, the 1-D reflection and transmission gratings may be thought as PBG materials, in fact for one-dimensional structures a small amount of periodicity is needed to open a band-gap even for very low dielectric contrast ($\Delta\varepsilon/\varepsilon \sim 0.08$ produces a 2.65% gap) (see [Joannopoulos 1995]) for all the details about the quarter-wave stack and 1-D PhCs).

The band diagram depends on the symmetry of the structure, the refractive indices, the number and geometry of layers, that is on the fabrication parameters as well as on the propagation direction and polarization of the electromagnetic modes.

In 1989, Yablonovitch realized the first PhC consisting in a face centered cubic (FCC) structure of silica in air (holes) that showed a PBG in the microwave range due to its characteristic sizes. In fact, to realize a PhC in the optical range, say in the IR at $1.55\mu m$ (the telecom wavelength), great efforts have been made: roughly speaking, the mid-gap wavelength must be close to the lattice constant of the photonic crystal.

The great potential of PhCs, however, is related to the possibility of introducing controlled defects into the structure, so that allowed states might appear inside the band-gap between the so called dielectric band (valence band) and air band (conduction band). In [Braun 2006] you can find a review about the state of the art of defects into PhCs. The defects consist of region of different material and/or different size that break the symmetry of the lattice.

They can be point-like or linear defects, the latter being an array of point defects. An electromagnetic field of the proper frequency results localized into the point-like defect that acts as a cavity resonator with perfect reflecting walls because light cannot propagate throughout the structure. In a 1-D grating the defect may be obtained simply varying the size of a single layer, producing, as for instance, a spectral filter. By means of linear defects in a 2-D or 3-D lattice, the light may be localized along a particular path, propagating without loss even in presence of high curvatures, because the physical principle exploited is not the total internal reflection (as in optical fibers and waveguides) but the existence of a PBG lattice external to the pathway. In this way integrated optical interconnections, waveguides and fibers way be realized with sub-micrometric spatial resolution.

The external efficiency may be improved in LED favoring the emission only of the optical modes that possess a good external coupling by avoiding the problem of total internal reflection and increasing the efficiency from 4% to 97%. Moreover, this reduces the thermal dissipation favoring the integration.

2.4.2 Lasing Effect

The laser emission may be improved consenting to realize low threshold devices ($< 100\mu A$) of very small dimensions and provided of high spectral purity. Within

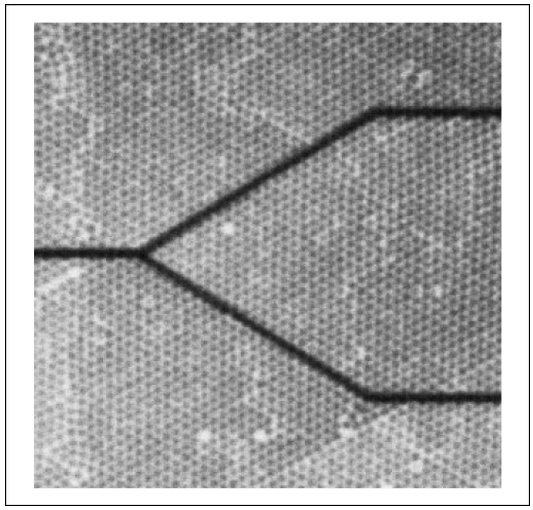

Figure 2.23: Example of a 2-D PhC made of a triangular close-packed configuration that permits to achieve a large complete PBG; a linear Y-channel is realized into the crystal to allow the controlled propagation of wave-guidedmodes [Braun 2006].

the band-gap, the wave is evanescent and decays exponentially, so that the density of states (DOS) within the gap vanishes in large structures. Since the rate of spontaneous emission is proportional to the DOS, spontaneous emission is suppressed within the gap. This enhances the integrability due to the lower power dissipation.

Let us consider the most simple photonic crystal, a one-dimensional system consisting of alternating layers of material with dielectric constants, ε_a and ε_b, and layer thicknesses a and b (Fig. 2.22). The refractive indices are

$$n_a = \sqrt{\varepsilon_a}, \text{ and } n_b = \sqrt{\varepsilon_b}.$$

Let us assume that the material is dispersion-less and lossless, periodic in the z direction, and homogeneous in the transverse $x-y$ plane. Let us index all the wavefunctions along this plane by their propagation vector $k_{\shortparallel}$, whereas k_z represents the wave vector in the z direction. In the layering direction, because of the periodicity, wavefunctions are Bloch waves and stop-bands may exist. Let us consider a light propagating normal to the plane, $k_{\shortparallel} = 0$. The time-independent Maxwell's equation is in the scalar form,

$$\frac{\omega^2 \varepsilon(z)}{c^2}\psi(z) + \frac{d^2}{dz^2}\psi(z) = 0,$$

where $\varepsilon(z)$ is a function with period $d = a + b$. The wavefunction $\psi(z)$ represents the electric or magnetic field and has the Bloch form

$$\psi(z) = e^{izK} u_k(z),$$

where $K = |\mathbf{K}|$ is the modulus of the Bloch wavevector and u_k is a periodic function

of period d. The dispersion relation $\omega(k)$ is determined by the equation

$$\cos Kd = \cos(k_a a)\cos(k_b b) - \frac{1}{2}\left[\frac{k_a^2 + k_b^2}{k_a k_b}\right]\sin(k_a a)\sin(k_b b) \tag{2.56}$$

(for further calculations see [Joannopoulos 1995]), where

$$k_a = \frac{n_a \omega}{c}, \text{ and } k_b = \frac{n_b \omega}{c}.$$

We can identify two conditions. If the right member of equation 2.56 has an absolute value less than or equal to the unity, the value of K is real, so propagating modes are allowed. Band-edge state occur when $Kd = m\pi$, so that $\cos(Kd) = \pm 1$. At the band edges the wavefunctions are standing waves. Inside the band-gap, equation 2.56 yields to a complex wavevector K, corresponding to a decaying wave. The density of states (DOS) diverges because the band-edge is approached as an inverse square root and vanishes inside the band-gap. The standing waves at the lower and upper edges have the same value of K but are mutually orthogonal.

The density of states may de defined as

$$\text{DOS} \propto \frac{dk}{d\omega},$$

that is the reciprocal of the group velocity. The DOS has its largest value at modes closest to the edges of the band, where the line is the narrowest and the dwell time is the greatest. This reflects the accumulation of energy inside the sample. Thus, the band-edge resonance is favorable for lasing.

2.4.3 Photonic Crystals Fabrication Techniques

Materials typically involved for the PhC fabrication are SiO2, Si3N4, AlGaAs, GaAs, that are all well known technologies of the high frequency electronics (see again [Joannopoulos 1995] for their band diagrams). The fabrication techniques are multiple: lithography (e-beam, deep x-rays), chemical etching (RIE, CAIBE), epitaxy, deposition.

On the other hand, the employment of soft materials instead of hard ones, may give very important advantages both for the control of tunable devices and for the flexibility of low cost and high performance production techniques, among which we find holography and holographic lithography, as discussed in Sec. 3.1.6. In fact, as two-beam holography has been used successfully for the realization of one-dimensional PhCs. Other holographic approaches have found large employment for the fabrication of more complex PhCs devices (just to cite two important papers, see [Berger 1997] and [Campbell 2000]).

2.5 Photonic Quasicrystals

2.5.1 A brief Introduction to Quasicrystals

Before 1984 the rules of classical crystallography were strictly limited to the crystalline structures with a translational periodicity. According to this theory, the ex-

istence of both rotational and translational symmetries results in a geometrical constraint that limits lattice structures to only two-, three-, four-, and sixfold symmetries to fill up the entire space. It was assumed to be impossible for other symmetries to form crystalline structures. In 1984, Shechtman and coworkers [Shechtman 1984] reported on rapidly quenched samples of several transition-metal aluminum alloys that produced electron-diffraction patterns with sharp spots [Stephens 1986], and crystals with icosahedral symmetry were shown to exist [Steinhardt 1987]. The notion of quasicrystals originated. The discovery of quasiperiodic crystals stimulated the scientific community in search of extraordinary properties in these unusual crystals. In classical crystallography theory, when the rotational symmetry and translational symmetry are considered simultaneously, an infinite crystal structure has only one-, two-, three-, four-, or sixfold symmetry to fill up the entire space. However, a quasi-lattice with forbidden rotational symmetry for periodic crystals such as fivefold symmetry in the plane and icosahedral symmetry in three dimensions, can also fill up the entire space forming an infinite structure. These kinds of new-ordered lattices lack an overall absolute translational symmetry, exhibit multifold symmetries similar to those having two-, three-, four-, and sixfold and exhibits interesting properties.

The unit cells repeat along its symmetry axis and overlap each other in a complex manner to fill up the entire space. Locally, their environment demonstrates an overlapping translation and a multifold symmetry. This local overlapping periodicity acts as a superimposed Bragg grating and gives rise to multiple forbidden PBG frequencies. Quasicrystals are structures exhibiting long-range aperiodic order and rotational symmetry [Levine 1984] [Stadnik 1999]. They may possess photonic bandgaps (PBG) [Chan 1998] [Zhang 2001] that are more isotropic than in conventional photonic and, hence, the PBG becomes more spherical leading to interesting properties of light transmission [Cheng 1999], wave guiding and localization [Jin 1999], increasing the flexibility of these materials for many photonic applications.

Some consider quasi-crystal lattice structures as the intermediate state between crystal and amorphous solids. If so, well-controlled defects can be introduced in the photonic lattice and can be applied to many applications of PBG materials based on highly localized defect states in the PBG. Moreover, the aperiodicity gives rise to the existence of many inequivalent defect localizations, permitting a large versatility. Others consider quasicrystals as highly ordered structures like crystals but with quasiperiodic or distributed periodic rather than discrete periodic lattice points. In many ways these lattice structures exhibit properties analogous to conventional crystal lattice structures; particularly, quasicrystals have diffraction patterns consisting of sharp Bragg peaks in disallowed crystallographic patterns. Today the crystal definition has been displaced from the real space to the reciprocal space including all structures possessing essentially discrete patterns, like the periodic crystals as well as non-periodic or quasiperiodic crystals. The standard crystallographic methods cannot be used directly to determine the structure of the quasicrystal owing to the lack of periodicity. Many different types of structure have been proposed and

explained. Penrose tiling, a 2D lattice with pentagonal orientational symmetry and a non-periodic tiling[Elser 1986] developed by R. Penrose, is an example of a quasi-lattice, a term first used by Mackay and Quinquangula [Mackay 1981] (see Fig. 2.24). Burkov [Burkov 1991] explained a decagonal quasicrystal as a layered structure with every layer being a 2D quasicrystal. Quasicrystal systems, such as eightfold (octagonal) [Jin 1999] [Cheng 1999] (see Fig. 2.26), ten-fold (decagonal) [Burkov 1991] [Jin 2000], and twelve-fold (dodecagonal) [Gauthier 2005] [Zoorob 2000] symmetric photonic quasicrystals (see Fig. 2.25), have been shown to exist in nature. Explaining the quasi structure is not trivial, and there is no consistent classical theory to explain all types of 2-D and 3-D quasi structure and their resulting diffraction behaviors.

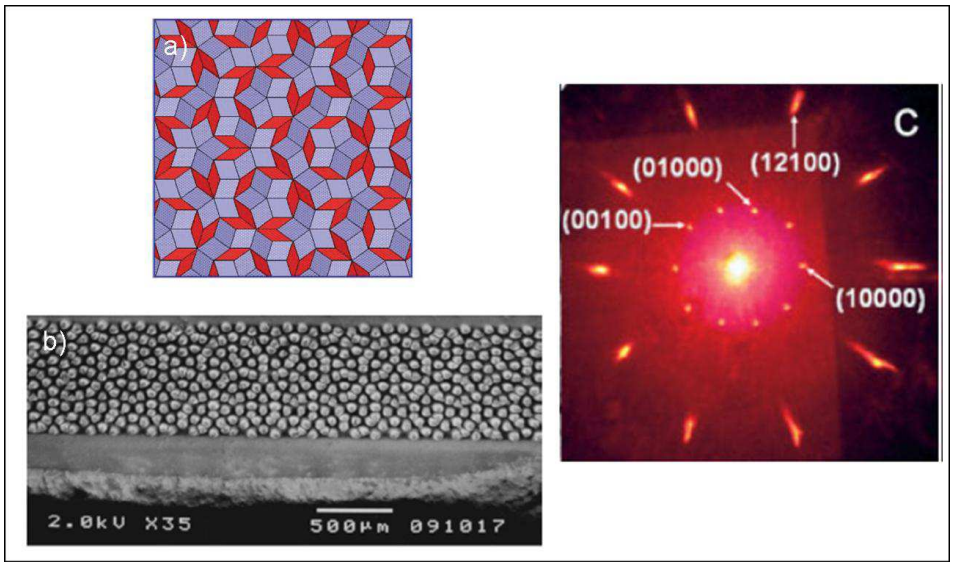

Figure 2.24: a) Penrose tiling with rhombuses; b) experimentally, at the vertices of the unit-tile the rods of dielectric materials are placed forming a PhQC [Hase 2002]; c) the structure produces a tenfold centrosymmetric diffraction pattern [Wang 2003].

2.5.2 Photonic Quasiperiodic Structures

In the same decade, marking a landmark in photonics, photonic crystals with periodic arrangements of materials were conceived by Yablonovitch and John, as discussed in the previous sections. Naturally, suggested by the underlying PhC idea, quasi lattices on the optical scale have intrigued scientists greatly, and much attention has been devoted to the properties and fabrication of photonic quasi-crystals.

Typically, to achieve a complete PBG in PhCs, materials with refractive index substantially higher than $n = 2.0$ should be employed. In contrast, the Photonic Quasicrystal (PhQCs) is an example of PBG material, which does not require high refractive indices to obtain complete PBG. Photonic quasicrystals are artificial di-

electric inhomogeneous media, where scattering centers are located in the vertices of a quasi-periodic tiling of space [Suck 2002]. PhQCs have neither true periodicity nor translational symmetry, but have a quasi-periodicity that exhibits long-range order and orientational symmetry, as aforementioned, so that 2-D PhQCs may have high-order rotational and mirror symmetries not achievable by conventional PhCs. Recent studies about quasicrystals with 8-fold, 10-fold (decagonal or Penrose [4]) and 12-fold symmetries have demonstrated that, in general, most of the PhQCs have wide complete band-gaps and small threshold value of refractive index for opening a complete gap. Therefore, the PBG exists not only in periodic structures, but also in non-periodic structures such as quasicrystalline arrangement of dielectrics. Chan et al. [Chan 1998] studied and discussed theoretically the PBG in 2-D octagonal aperiodic photonic quasicrystals. They found the existence of spectral gaps in these quasiperiodically arranged dielectric system. However, they found that in the octagonal system, the TE and TM spectral gaps usually do not overlap for a reasonable value of the dielectric constant. Recently, Zoorob et al. [Zoorob 2000] claimed that they found absolute photonic gaps in 12-fold symmetric quasicrystals that were realized with small air-holes in a silicon nitride or glass waveguide substrate (Fig. 2.25). This is a rather surprising result since both silicon nitride and glass have fairly low refractive indices. The result will have important consequences. Not only that glass

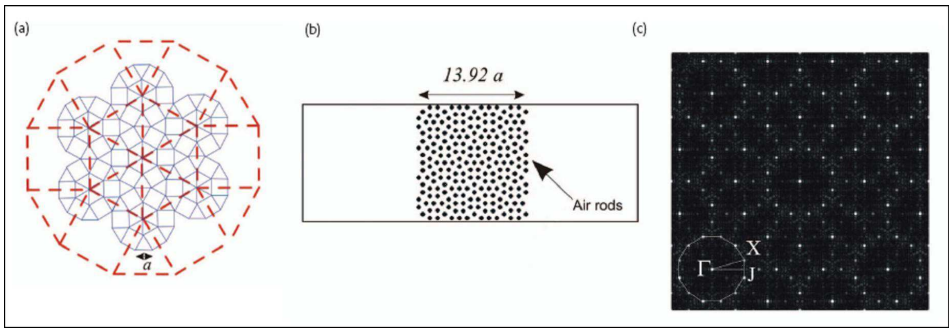

Figure 2.25: a) Square-triangle tiling geometry of a 12-fold pattern; b) scheme of the related structure obtained locating the dielectric rods at the vertices of the tiling with pitch a; c) diffraction pattern demonstrating the 12-fold rotational symmetry: the dashed dodecagon shows the supercell corresponding to the Brillouin zone [Zoorob 2000].

is a very common material and is transparent in optical frequencies, the fact that the refractive index of glass is only about 1.45 implies that absolute photonic gaps can be achieved with many available materials. Since photonic quasicrystals have higher rotational symmetries than ordinary crystals, they have the optimal conditions for forming a complete isotropic PBG even in soft materials like polymers.

The possibility to exploit polymers and other soft materials is a very important

[4]Due to the properties of the diffraction pattern, a 5-fold, that is a Penrose structure, possesses a 10-fold rotational symmetry. Then, with regard to the rotational symmetry, they are equivalent.

issue because of the enormous and compelling advantages of using a flexible and versatile cheap technology, together with the employment of a holographic technique able to realize both large-area and high quality structures (Fig. 2.26c).

2.5.3 Quasicrystals Fabrication Techniques

To construct two-dimensional or three-dimensional quasicrystals is a very difficult task because conventional methods used in the micro-chip fabrication (such as semiconductor lithography, multi-photon adsorption, template-based techniques, etc.) and also special methods developed for making photonic crystals (such as self-assembling of colloidal micro-spheres or micro-fabrication) are inadequate. Compared with conventional fabrication techniques for photonic crystals and quasirystals such as microfabrication, Holographic Lithography (HL) provides a more feasible and convenient way for fabrication of simple or complicated periodic PhCs and aperiodic lattices on the optical wavelength scale. Then, previously used to realize periodic photonic crystals [Campbell 2000] [Berger 1997], holographic lithography was recently proposed and used to realize quasicrystals too at the mesoscale in polymer resins [Wang 2003] [Wang 2003], Holographic Polymer Dispersed Liquid Crystals (H-PDLC) [Gorkhali 2005], and holographic plates [Yang 2006] (an example of the structure is reported in Fig. 2.26).

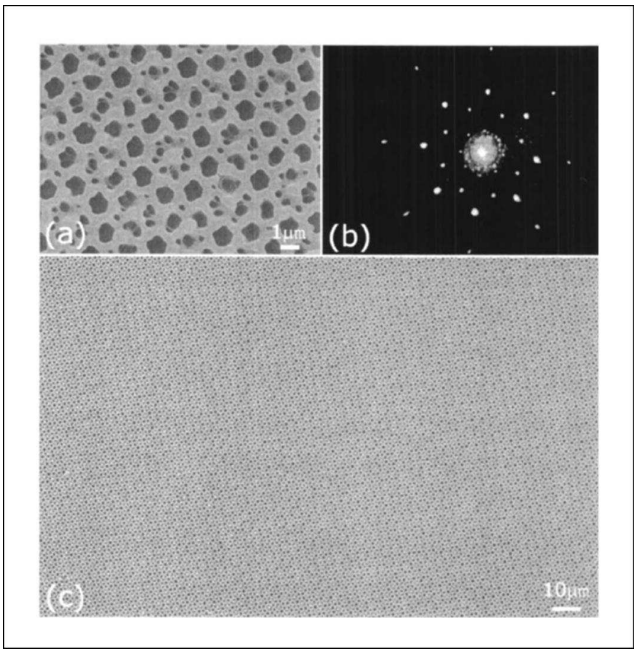

Figure 2.26: a) Example of a 8-fold quasicrystal made in polymer using HL; b) the related diffraction pattern showing an 8-fold rotational symmetry; c) large area 8-fold PhQC [Wang 2003].

The holographic lithography is based on the interference pattern of many co-

herent light beams, that are usually obtained by splitting a single laser beam by suitable grating, prism or dielectric beam splitters [Gorkhali 2006], in a single or multiple exposure process [Gauthier 2004]. In the holographic fabrication of 2-D five-fold symmetric photonic quasi crystals, Wang et al. [Wang 2006] and Gorkhali et al. [Gorkhali 2005] have presented an association between symmetry order and laser beams, implying that the order of symmetry and number of beams should be identified. That is, the higher the order of symmetry, the greater the number of beams needed. However, experimental feasibility is questionable, requiring to control the amplitude and phase of N interfering laser beams, when the symmetry order is too high, since great complexity is introduced by additional beams because of excessive initial phases, wave-vector differences, and other destabilizing factors. Moreover, when the number of laser beams is even and larger than 3, sophisticated adjustment is inevitable to avoid modulating stripes throughout the whole sample [Mao 2006]. Gauthier and Ivanov have reported an interesting dual beam multiple exposure HL method [Gauthier 2004], which can reduce the complexity of interference patterns in the multiple beam single-exposure process. However, the strong background caused by each exposure to one another will reduce the contrast of the interference pattern formed in the sample. Moreover, precise mechanical rotation at the same axis should be guaranteed especially for large-area photonic quasi crystals. Therefore, a combination of minimum laser beams and one-step HL is required in the fabrication of large-area photonic quasicrystals.

Moreover, quasi-periodic structures may be envisaged that cannot be realized even in principle by multiple-beam interference. PBGs have been observed in optical multilayers stacked according to a Fibonacci sequence, a one-dimensional quasi-periodic structure not achievable with HL, when an incident light was normal to the layers [Kohmoto 1987] [Gellermann 1994]. The Thue-Morse structure is another example of aperiodic pattern [Macià 2006], defined by recursive sequences, that cannot be obtained by interference of coherent beams. One-dimensional Thue-Morse gratings are known to exhibit PGB with interesting omnidirectional reflectance [Kolar 1994] [DalNegro 2004]. Theoretically studies about 2-D Thue-Morse gratings, defined mathematically by recursive procedure, have shown the presence of PBG [Moretti 2007].

Introducing a defect inside a PhQC with HL has not been yet experimentally demonstrated to my knowledge. Laser writing technique has been used in this sense, permitting to write point-by-point the desired structure (see, as instance, [Zhou 2007]).

2.5.4 Multiple-beam Holography

In this work, several kind of quasicrystals, both quasiperiodic and aperiodic, have been produced, with high rotational symmetry and novel arrangements without the need for sophisticated control of the multiple-beam scheme: but with a single-beam approach. The possibility to introduce defects in a single-exposure process has also been proven. These results demonstrate the great potential of the CGH-SLM tech-

nique. The designing of the several structures realized makes use of the principles of the multiple-beam interference in order to achieve in a straightforward calculation the holograms needed for the writing process and to reconstruct holographically the multiple-beam arrangement desired, although with a single-beam as discussed in Sec. 3.1. In order to clarify some important aspects of the CGH method, in this Section I will introduce the theoretical principles of multiple-beam holography. As

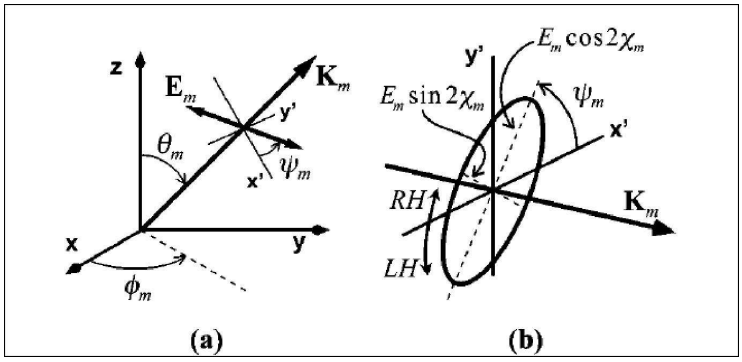

Figure 2.27: Coordinate system and holographic parameter definitions: a) propagation angles and b) polarization angles.

with conventional holography, interference patterns resulting from more than two laser beams depend on both the propagation and polarization parameters of each beam, and must therefore be chosen such that the desired optical lattice is created. Let us calculate the most general expression of the intensity profile $I(\mathbf{r})$ formed by N coherent plane waves, based on arbitrary irradiance, propagation, polarization, and phase of each beam.

The electric field vector of the $m-th$ wave with complex amplitude can be written in phasor notation as

$$\mathbf{E}_m = \mathbf{e}_m E_m[\exp(i\mathbf{K}_m \cdot \mathbf{r} + i\delta_m)], \tag{2.57}$$

where E_m is the real amplitude, $\mathbf{r}(x, y, z)$ is the position vector,$\mathbf{K}_m$ is the propagation vector, and δ_m is the absolute phase. Express $\mathbf{K}_m$ in spherical coordinates system defined in Fig. 2.27, such that

$$\mathbf{K}_m = \frac{2\pi}{\lambda}(\cos\phi_m \sin\theta_m, \sin\phi_m \sin\theta_m, \cos\theta_m), \tag{2.58}$$

where θ_m and ϕ_m are the polar and azimuthal angles, and λ is the wavelength. The polarization of the $m-th$ wave can be completely described in terms of the orientation and ellipticity angles ψ_m and χ_m, respectively (Fig. 2.27). Without loss of generality, it is possible to define the complex electric field vector, given by

$$\mathbf{e}_m = \mathbf{R}(\theta_m, \phi_m)\mathbf{J}_m(\psi_m, \chi_m), \tag{2.59}$$

that is as the rotation of its Jones vector, defined as

$$\mathbf{J}_m(\psi_m,\chi_m) = (\cos\psi_m\cos\chi_m, \sin\psi_m\cos\chi_m,0)+i(-\sin\psi_m\sin\chi_m, \cos\psi_m\sin\chi_m,0), \tag{2.60}$$

from its local reference to the global coordinates by using the following rotation matrix:

$$\mathbf{R}(\theta_m,\phi_m) = \begin{bmatrix} \cos\phi_m\cos\theta_m & -\sin\phi_m & \cos\phi_m\sin\theta_m \\ \sin\phi_m\cos\theta_m & \cos\phi_m & \sin\phi_m\sin\theta_m \\ -\sin\theta_m & 0 & \cos\theta_m. \end{bmatrix} \tag{2.61}$$

The general polarization state described by the Jones vector is elliptical and it reduces to the special cases of p-polarization (TM) or s-polarization (TE) for $\chi_m = 0$ (both) and $\psi_m = 0$ or $\psi_m = \pi/2$. The intensity is defined as the vector product of the total electric field $\mathbf{E}_{tot} = mathbfE_1 + mathbfE_2 + ... + mathbfE_N$ with itself. The volumetric intensity profile of coherent waves can therefore be expressed in terms of the sum of vector products as follows:

$$\begin{aligned} I(\mathbf{r}) &= \mathbf{E}^*_{tot}\cdot\mathbf{E}_{tot} \\ &= \Re\left(\sum_{l,m=1}^{N}\mathbf{E}^*_l\cdot\mathbf{E}_m\exp[i(\mathbf{K}_l-\mathbf{K}_l)\cdot\mathbf{r}+i(\delta_l-\delta_m)]\right). \end{aligned} \tag{2.62}$$

The above equation, after algebraic manipulation, leads to the preferable form:

$$\frac{I(\mathbf{r})}{I_{tot}} = 1+\sum_{l<m=1}^{N}[V_{lm}\cos(\mathbf{G}_{lm}\cdot\mathbf{r}+\delta_{lm})+W_{lm}\sin(\mathbf{G}_{lm}\cdot\mathbf{r}+\delta_{lm})], \tag{2.63}$$

whereas $\delta_{lm} = \delta_l - \delta_m$ are the phase mismatch related to each couple of beams, whereas $\mathbf{G}_{lm} = \mathbf{K}_l - \mathbf{K}_m$ are the relative differences of the wave vectors and represent the fundamental vectors of the reciprocal lattice of the structure. It can be produced by positioning the unit cells or "atoms" (dielectric rods as for instance) at the constructive interference points $\bar{\mathbf{r}}$ defined by the Bragg's diffraction condition $\mathbf{G}_{lm}\cdot\bar{\mathbf{r}} = 2n\pi$, with n integer. The quantity $I_{tot} = \sum_1^N E_m^2$ is the total intensity whereas V_{lm} and W_{lm} are the intensity contrasts defined as

$$V_{lm} = 2E_lE_m\Re(\mathbf{e}^*_l\cdot\mathbf{e}_m)I^{-1}_{tot}, \tag{2.64}$$

$$W_{lm} = -2E_lE_m\Im(\mathbf{e}^*_l\cdot\mathbf{e}_m)I^{-1}_{tot}. \tag{2.65}$$

Equation 2.63 fully describes the intensity profile of N coherent beams in the most general terms possible, encompassing the interference of elliptically polarized beams. Notice that since each plane wave is represented by seven parameters $(\lambda, E_m, \theta_m, \phi_m, \psi_m, \chi_m, \delta_m)$, the irradiance profile depends on at most $6N+1$ variables. However, in many important cases, the number of independent unknowns affecting the volumetric morphology of $I(\mathbf{r})$ can be as low as $4N$. From equation 2.63 it is possible to generate all the periodic 2-D and 3-D Bravais lattices with an optical resolution and finding the relationships between the wave parameters and

the unit cells of the patterns to be designed. Moreover, quasiperiodic arrangements may be achieved acting on the parameters of the irradiance. The strict requirement to obtain two-dimensional interference patterns is that the difference vectors $\mathbf{G}_{lm}$ must be coplanar. All five 2-D Bravais lattices can be formed by $N = 3$ beams. For $N > 3$ other interesting crystal and quasicrystal patterns can result. Forming 3-D volumetric structures is possible by controlling the propagation and polarization of a low number of coherent beams to create all fourteen Bravais lattices. The strict requirement for intensity variations in three dimensions is that the difference vectors $\mathbf{G}_{lm}$ must be noncoplanar, which implies that $N \geq 4$. If the set of $\mathbf{G}_{lm}$ lie on a lattice, the irradiance profile is periodic. For example, if they lie on a body-centered cubic (bcc), the optical interference forms a face-centered-cubic lattice (fcc), and the vectors $\mathbf{G}_{lm}$ can be considered as the reciprocal wave vectors of the periodic structure. Otherwise, the irradiance profile is a 3-D aperiodic structure, a quasiperiodic crystal. Several irradiance profiles are shown in Fig. 2.28 calculated using Eq. 2.63

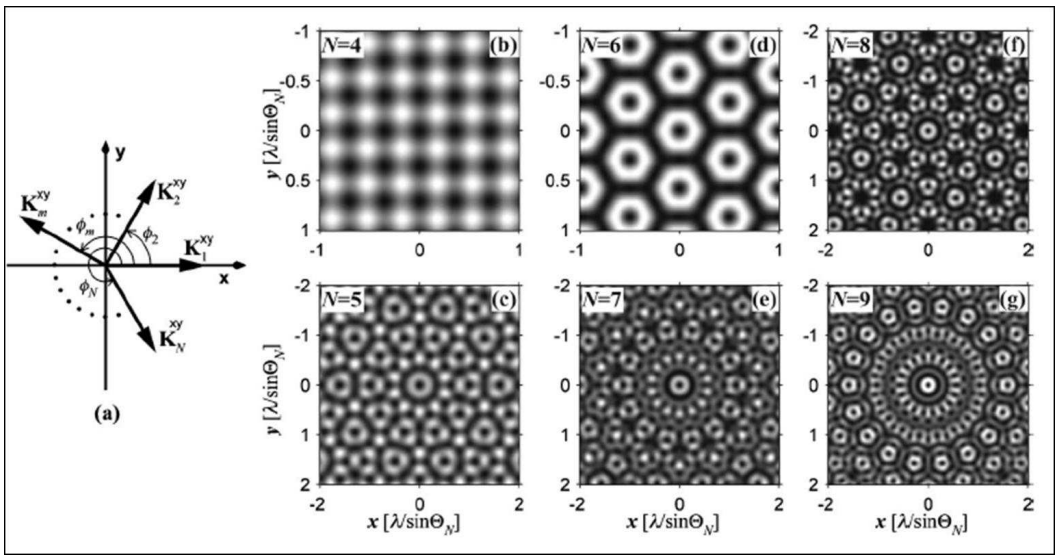

Figure 2.28: The family of 2-D interference profiles that results with N beams equally spaced around the azimuth. Beam geometry is shown in (a) and the resulting optical patterns for $N = 4$ through 9 are shown in (b) through (g), respectively.

for $4 < N < 9$, assuming $\delta_{lm} = 0$, $\psi_m = \pi/2$, and $\chi_m = 0$ for all l and m. Notice that the irradiance profiles for $N = 4$ and 6 are periodic, leading to square and triangular lattices, where the primitive basis of this triangular lattice is a hexagon with a center circle removed. However, the patterns for $N = 5$, 7, 8, and 9 are quasiperiodic. In most cases, like those quasiperiodic profiles in Fig. 2.28, the M-fold rotational symmetry about a central point is forbidden from the point of view of periodic crystal description, since the 2-D or 3-D profiles exhibit a reciprocal lattice of a higher dimension than the physical dimension. To better understand, let us consider a solid where its dielectric profile $\rho(\mathbf{r})$ can be expanded by a countable

Fourier series, that is

$$\rho(\mathbf{r}) = \sum \rho(\mathbf{k}) \exp(i\mathbf{k} \cdot \mathbf{r}),$$

where the summation is over the $\mathbf{k}$ that belong to a finite set of vectors, say $\mathcal{L}$, and where $\rho(\mathbf{k})$ are the set of Fourier coefficients defined over the set of wave vectors $\mathbf{k}$. Crystals are generally quasiperiodic when there exists a finite number $\mathcal{D} < \mathcal{L}$ of wave vectors that can span all the rest through linear combinations. When the entire set $\mathcal{L}$ can be spanned by $\mathcal{D}$ wave vectors through integral linear combinations, then $\mathcal{D}$ is called the rank or the indexing dimension of the crystal. Periodic crystals can be seen as a special case, occurring when the rank $\mathcal{D}$ is equal to the physical dimension. In all of these cases, the diffraction pattern of $\rho(\mathbf{r})$ contains discrete Bragg peaks that can each be indexed by a set of $\mathcal{D}$ integers. In the case of 2-D and 3-D periodic crystals, a set of two and three integers, respectively, describes positions on the lattice, while five or more are required for 2-D and 3-D quasiperiodic crystals. Using these insights, we can see that holographic fabrication of quasiperiodic optical patterns involves arranging the difference vectors $\mathbf{G}_m$ along the set of $\mathcal{D}$ directions (that is the $\mathbf{k}$) arising from the desired quasiperiodic crystal pattern. Note that the quasiperiodic patterns in Fig. 2.28 are only a few of the 2-D possibilities and that 3-D quasiperiodic optical patterns can also be generated when $N > 5$ and their difference vectors are noncoplanar.

Summarizing, the fabrication of photonic crystals and quasicrystals require the design of the proper multiple-beam geometry and the control of the parameters involved in the interference pattern. For further readings on this topic see Escuti and Crawford [Escuti 2003]. By acting on them, it is possible to generate in the case of periodic crystals, at least in principle, the desired structure with the suitable unit cell in order to satisfy the required PBG conditions. The designing in the case of quasiperiodic structures is more complex because the number of parameters involved increases with the number of the beams needed to achieve the desired N-fold rotational symmetry. Moreover, if the periodic structures possessing a PBG are known, the relation between the quasiperiodic dielectric distribution, and hence the construction parameters, with the consequent PBG properties (if a PBG exists!) are yet unknown with the exception of a few cases experimentally and theoretically studied in literature. In this work this relation will be examined with interesting results as discussed in the experimental chapter.

Let us now consider some particular two-dimensional periodic and quasiperiodic irradiance profiles that will be used as the starting point for the development of several holograms used to design and fabricate the structures achieved during this thesis work. Let us begin with the case of $N = 3$, by which periodic patterns with square and triangular tiling may be obtained. The interference of three noncollinear $\mathbf{K}_m$ always results in a 2-D intensity profile since the difference vectors are always coplanar. It's convenient to align the XYZ coordinate system such that the polar propagation angles are all equal and that one of the reciprocal wave vectors, e.g. $\mathbf{G}_{23}$ is parallel to the Y axis. This is illustrated in Fig. 2.29. The set of $\mathbf{G}_{lm}$ forms a triangle. It can be shown that when $N = 3$ any variation in the relative phase

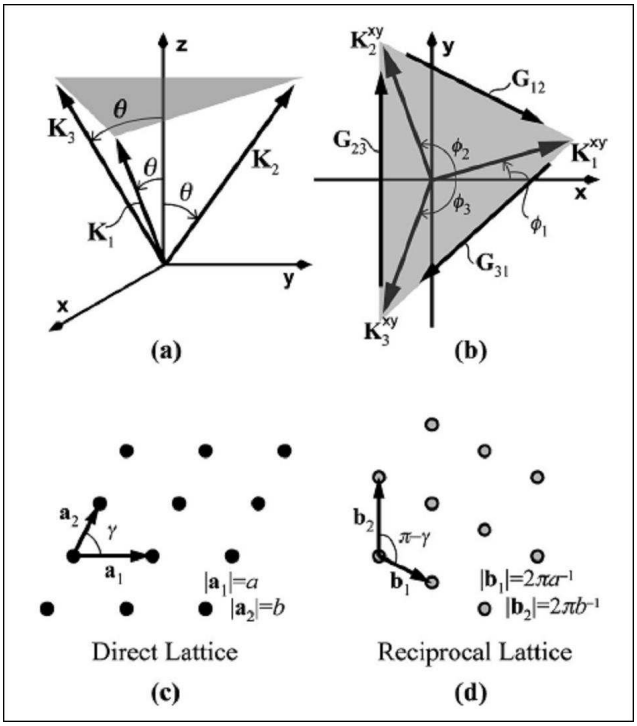

Figure 2.29: Crystallographic notation for 2-D optical lattices formed by three coherent beams: (a) beam geometry in perspective, (b) beam geometry within the XY-plane showing reciprocal wave vectors, (c) resulting direct lattice, and (d) associated reciprocal lattice.

between beams (δ_{lm}) leads only to a translational shift of $I(\mathbf{r})$ within the plane, and can therefore be neglected without loss of generality. Note that with these conventions, we find the conditions typically employed in a three-beam experiment, that is the parameters involved become $\theta_1 = \theta_2 = \theta_3 = \theta$ and $\phi_2 = -\phi_3$. In this way the intensity profile depends only on x and y and the $\mathbf{G}_{lm}$ vectors lie completely within the XY plane, as illustrated in Fig. 2.29-(b). From the 2-D intensity function $I(x, y)$, it is evident that the maximum-intensity points form a lattice, and that any couple of difference vectors are linearly independent so that may be defined as the fundamental vectors of the reciprocal lattice: $b_1 = \mathbf{G}_{12}$ and $b_2 = \mathbf{G}_{23}$. The lattice constants and angle may be expressed in terms of the propagation angles in the holographic setup. The direct and reciprocal lattices for this geometry with the related parameters are shown in Figs. 2.29(c)-(d), respectively, where it is to verify that

$$a = |\mathbf{a}_1| = \frac{\lambda}{|\sin\theta(\cos\phi_1 - \cos\phi_2)|}, \tag{2.66}$$

$$b = |\mathbf{a}_2| = \frac{\lambda}{2|\sin\theta\sin\phi_2\sin(\frac{\phi_1+\phi_2}{2})|}, \tag{2.67}$$

$$\gamma = \cos^{-1}(\frac{\mathbf{a}_1 \cdot \mathbf{a}_1}{ab}) = \frac{\phi_1 + \phi_2}{2}. \tag{2.68}$$

In Fig. 2.30, the family of five 2-D Bravais lattices achievable with a 3-beam interference is shown, among which the square and triangular pattern have been calculated. On the right of each irradiance profile the structure achievable with optical curing of a photosensitive polymer is depicted: the approximated polymer morphology is computed by applying a threshold to the irradiance profile at the maxima positions.

Let us now consider the case of a multiple-beam process leading to quasiperiodic morphologies. For the sake of simplicity let suppose that the polarization of the beams are linear and the relative phase differences are all equal to zero, that are the conditions typically met in a multi-beam experiment (see [Wang 2003] [Wang 2006] [Gorkhali 2005]).

In Fig. 2.31 the irradiance profiles for five-, seven-, and ninefold quasi patterns, with the configurations of the propagation vectors and the polarization vector diagrams, are presented. The polar angle θ, measured from the z axis, determines the scale of variation of the profile. Larger is θ, smaller is the modulation in units of λ, supposed to be equal for each beam as in the previous calculations. Also in this case, the azimuth angles of the beams are supposed to be all equal dividing the solid angle in equal parts depending on the number N of the bemas, that is $\phi_m = \phi = \frac{2\pi}{N}$ $(m = 0, .., N)$. The patterns consist of 2-D quasiperiodic structures stacked along the vertical direction, forming continuous high- and low-intensity channel-like distributions. It can be demonstrated that by adding another beam with propagation vector along the z axis, the homogeneity along the third direction is broken giving rise to a modulation also in that direction and hence to a 3-D structure. The N beams are arranged in a conical formation such that the ends of all the wave

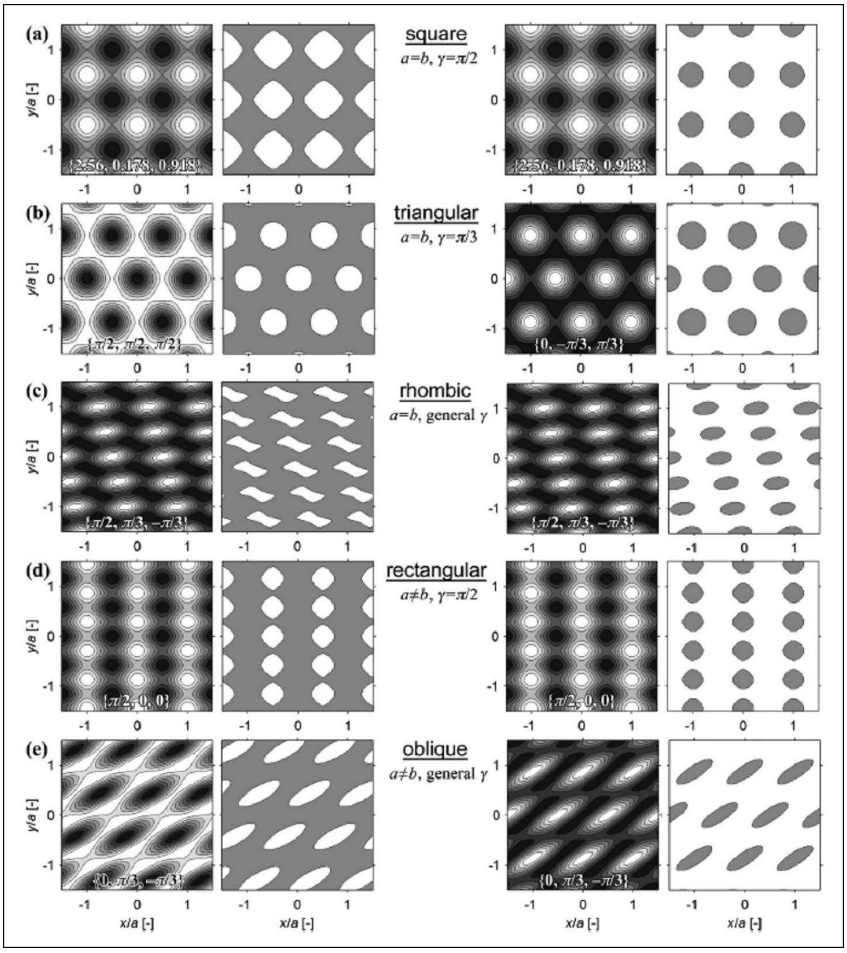

Figure 2.30: The family of five 2-D Bravais lattice textures formed with three coherent beams. The polarization orientation angle ψ_m for each case is shown within each profile (units of radians). The lattices are shown with a dark unit cell on the left and a bright unit cell on the right; the associated solid gray plots represent the approximated polymer morphology resulting by applying a threshold to the irradiance profile.

vectors lie on the same plane to create a 2-D quasi-interference pattern. Figure 2.31-(a) shows the wave vectors $\mathbf{K}_m$ of the beams and the corresponding reciprocal vector geometries $\mathbf{G}_{lm}$ for five-, seven-, and ninefold quasi designs (represented by the dashed line or the edges of the polygon), forming the basis vectors in the reciprocal lattice space. The irradiance profiles generated by p-polarized and s-polarized beams are shown in Fig. 2.31-(b) and 2.31-(c), respectively. The color gradient in the images represents the resulting intensity, in which red and blue represent the constructive and destructive interference regions, respectively. The wave vectors are

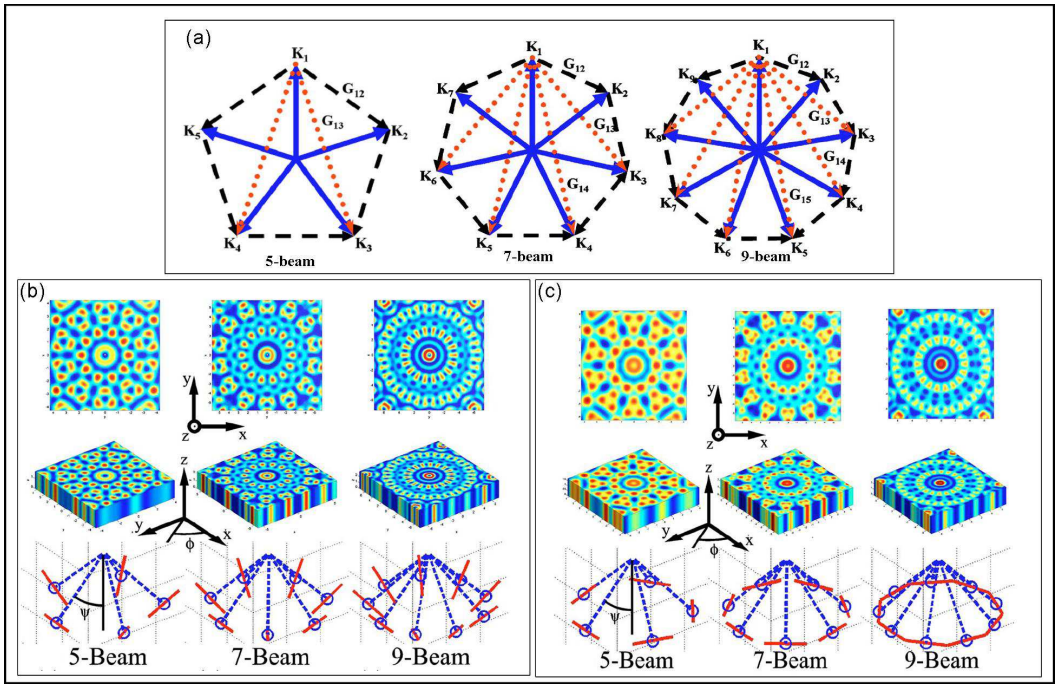

Figure 2.31: (a) Geometrical relationship between wave vectors ($\mathbf{K}_m$ solid lines), first-order reciprocal lattice vectors ($\mathbf{G}_{lm}$ with $m = l + 1$ dashed lines), and higher-order reciprocal lattice vector ($m = l + 2$ dotted lines) for five-, seven-, and ninefold quasi designs; (b)-(c) In-plane (top) and 3-D view (middle) of the intensity profiles for 5-, 7-, and 9-fold symmetry quasi structures generated by interfering p-polarized beam and s-polarized beam vectors (bottom), respectively.

not coplanar, but all the reciprocal lattice vectors are coplanar. For odd N, there are $2N$ first-order reciprocal vectors formed, considering both vectors pointing in the positive and negative directions. Hence the fivefold Penrose beam configuration results in a decagonal phase exhibiting tenfold symmetry. The dotted line vectors inside the polygon show a set of higher-order reciprocal lattice vectors, which are formed by the combination of first-order vectors. Again, the number of primitive wave vectors in each higher-order set is $2N$; for example, ten second-order vectors that have the same length as $\mathbf{G}_{13}$ can be drawn connecting vertices of the pentagon

in Fig. 2.31-(a). All other higher-order reciprocal vectors that are not primitive wave vectors are formed by the combination of more first-order vectors.

The reciprocal lattice vectors determine the resulting structure formed in real space and hence the diffraction pattern. In the quasiperiodic structure is not possible to determine a unit cell as for periodic crystals, nevertheless it is possible to define a similar self-repeating sub-structure as unitary cell at least to a first approximation. The repeating patterns in the quasi structure overlap in such a manner that the resulting distribution has strong density-distributed periodicity giving rise to sharp Fourier peaks, and then to an essentially discrete diffraction pattern into the far filed. The diffraction peaks have an N-fold symmetry. These peaks represent all the primitive reciprocal lattice vectors. The total number of primitive reciprocal vectors is equal to the number of ways N points (ends of each wave vector) can be connected, given by 20, 42, 72 permutations for five-, seven-, and ninefold structures, respectively. The Fourier transforms show the same number of peaks. The peaks due to each order are arranged in separate circles and have $2N$ peaks that correspond to the number of primitive wave vectors in each order. The diffraction pattern $F(u, v)$ may be derived from the lattice generated by the intensity profile $I(\mathbf{r})$ of equation 2.63 as

$$F(u,v) = \frac{1}{N^2} \sum_{u=0}^{N-1} \sum_{v=0}^{N-1} I(\mathbf{r}) \exp(-2\pi i \frac{ur\cos\theta + vr\sin\theta}{N}), \tag{2.69}$$

where $x = r\cos\theta$ and $y = r\sin\theta$, whereas

$$I(\mathbf{r}) = \sum_{l,m=1}^{N} E_l^* E_m \exp(i\mathbf{G}_{lm} \cdot \mathbf{r}) \tag{2.70}$$

represents the intensity distribution given from the interference of N beams equally polarized and with the same initial phases so that $\delta_{lm} = 0$ and equally spaced around the azimuth so that $\mathbf{G}_{lm} = \mathbf{K}_l - \mathbf{K}_m$ where each $\mathbf{K}_m$ assumes the following expression (derived from the equation 2.58):

$$\mathbf{K}_m = \frac{2\pi n}{\lambda}[\cos(\frac{2\pi m}{N})\sin\theta, \sin(\frac{2\pi m}{N})\sin\theta, \cos\theta]. \tag{2.71}$$

The symmetry of the diffraction pattern reflects clearly that of the quasi lattice, exhibiting N-fold rotational and mirror symmetries. The 2-D quasi structure repeating in the third dimension results in additional mirror symmetry. Therefore, the Penrose intensity pattern may be constructed by five symmetric beams resulting in a decagonal (10) point group. The seven- and ninefold patterns result in tetradecagon (14) and octadecagon (18) point groups, respectively. This property is evident in the diffraction patterns generated by the structures and that can be calculated by a 2-D Fast Fourier Transform (FFT) routine simulating the far filed diffraction projection (eq. 2.69) of the 2-D quasiperiodic lattices, as shown in Fig. 2.32 (bottom insets).

The pitch corresponding to the reciprocal lattice vectors $\mathbf{G}_{lm}$ may be calculated using Bragg's law as described in the previous section. The magnitudes of the basic

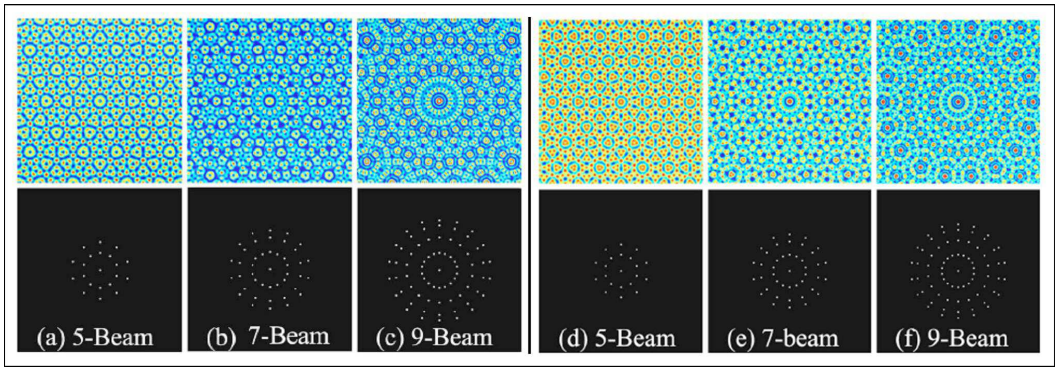

Figure 2.32: Intensity profiles for five-, seven-, and ninefold symmetry quasicrystals formed by (a)-(c) *p*-polarized and (d)-(f) *s*-polarized beams. Corresponding Fourier transforms illustrating the expected diffraction pattern (bottom).

reciprocal vectors in the diffraction patterns are related to sensible lengths of the crystal structures, such as a tile side [Kaliteevski 2001], so that by the observation of the experimental diffraction light is possible to acquire information about the quasi lattice. This is typically what ca be done also in the case of periodic structures. Moreover, by inverting the expressions in equation 2.66, it is possible to derive the values of the interference parameters that are required to design the desired 2-D structures, but this situation is clearly more complex in the case of a quasiperiodic profile.

We will see that the CGH-SLM technique completely alleviates the drawback of an accurate control of the parameters involved in the multiple-beam process, permitting, moreover, an high reproducibility of the designed writing distributions.

Chapter 3

A Single-beam Technique: Spatial Light Modulation based on Computer-Generated Holography

In the previous Chapter I described and discussed the theoretical framework and the experimental context in which the present thesis work may find its proper collocation, so that the unraveled issues could help the comprehension of the arguments that I'm going to discuss. In the introductive chapter I clarified the role, the context and the importance of the research activity here developed. In this research activity, the single-beam computer-generated holography has been exploited to functionalize liquid crystal-polymer composites in arrangements with a periodic and quasiperiodic dielectric modulation. This work, in fact, is aimed to the preparation and development of a novel fabrication technique of soft matter-based devices. The results obtained are promising. Now I will introduce the computer-generated holography, the principles of the spatial light modulation by means of a programmable liquid crystal Spatial Light Modulator (LC-SLM) and the numerical algorithms coded for the holograms generation in a Fourier holographic scheme. The experimental methods developed and adopted in this thesis work will be handled: a) Fourier Holography Scheme (FHS); b) Direct Writing Method (DRM); c) Interference-based Scheme (IS). The structures realized and the electro-optical characterization of the samples will be presented. Finally, the numerical simulations of the transmission spectra by means of the Finite Difference Time Domain algorithms, the band diagrams and analysis will be showed. The technique and the results obtained have been presented in two recent papers [Zito 2007] [Zito 2008]. A third has been accepted and is in printing. The recent paper of Karimi [Karimi 2007], of which I am coauthor, highlights the SLM capability to generate the desired optical field for beam shaping.

3.1 Computer-Generated Holography (CGH)

3.1.1 Introduction to the Spatial Light Modulation by CGH

Largely employed for holographic optical tweezers (see, as for instance, [Grier 1998] [Reicherter 1999] [Liesener 2000]), beam shaping and wavefront correction, Computer-Generated Holograms (CGHs) permit to create arbitrary 1-D, 2-D and even 3-D (see [Haist 1997] and [Sinclair 2004]) configurations of single-beam irradiance distribution by modulating the phase and/or amplitude profile of the laser

beam impinging on a Diffractive Optical Element (DOE), which is designed as a CGH (see [Soifer 2002] for the details about applications of CGHs). The DOE is essentially an optical element, like a simple glass lens, in which the template is structured so that the phase or amplitude profile results changed in a suitable manner. In this way it can modify the optical properties of the incident beam. In fact, after propagation and diffraction, the beam results to be spatially modulated in a given region of space. By designing the DOE in a suitable and precalculated phase (or amplitude) profile, the beam assumes the desired configuration, both in phase and amplitude or regarding its intensity distribution. The physical principle relies on optical holography (see [Hariharan 1984]). The object to be reconstructed by means of the hologram is in this case the desired irradiance distribution while the DOE is the holographic plate[1]. Usually, the DOE is previously fabricated and works as a static element to project in the Fourier plane (Fourier holography [Goodman 1996]) an array of intensity spots [Lee 2004].

In this work, a different approach is used, based on implementing the DOE with a programmable liquid crystal Spatial Light Modulator (SLM) which can encode the CGH directly in its LC-display, following the same basic principle that has been adopted by Grier in 2003 to produce reconfigurable holographic optical traps [Grier 2003]. This permitted us to exploit at best the potential of the attractive CGH technique. In fact, this method offers a high spatial resolution and real-time reconfigurability without any mechanical motion or realignment [Grier 2003] and permits to transfer to the photosensitive sample almost any intensity profile (like the one achievable, as for instance, in a multiple-beam interference) simply modulating one beam. This avoids the need of complex interference schemes and the drawbacks related to the long term stability and reproducibility of the multi-beam holography, above all the vibrational noise and the control of the multi-beam parameters.

To summarize the content of this Section, here I will explain how to design the suitable holograms that can spatially modulate a laser beam, and how to integrate them into a single-beam holographic scheme capable to produce the desired curing patterns by addressing computer-generated phase-only holograms (also called kinoforms) to the liquid crystal display of the SLM.

3.1.2 Spatial Light Modulator

The Spatial Light Modulator used in this work is essentially a programmable liquid crystal display acting as a diffractive optical element due to the property of interaction of the incident light with the liquid crystal molecules contained into the pixel cell. The LC molecules are nematic with a twisted alignment between the parallel ITO coated plates of the cell. The electrodes driven by a computer permit to apply discrete values of voltages V_m in a suitable range of 256 levels, so that $m = \{0, 1, ..., 255\}$. The external electric field reorients the LC-molecules in each

[1] For clarity, the hologram is in this case the holographic plate on which the phase and amplitude information is encoded after interference of the reference and object beams: in literature, usually the hologram is also the reconstructed image itself.

pixel-cell separately and with a fixed degree of reorientation depending of the voltage level applied (as discussed in Sec. 2.1.6). The molecules in the middle of the cells will be largely reoriented whereas the molecules at the closer to the cell surfaces will result almost unvaried due the strong anchoring forces. Due to the birefringence of the molecules, the incident light (linearly polarized) that travels trough the cell, consequently, experiments an integral phase retardation $\Delta\Phi$ depending of the reorientation degree and the optical path according to

$$\Delta\Phi = \int_0^d \frac{2\pi}{\lambda}[n_e(z,\theta) - n_o]\mathrm{d}z, \tag{3.1}$$

and, hence, depending to V_i (see Fig. 3.1). In this way, each level of voltage V_m

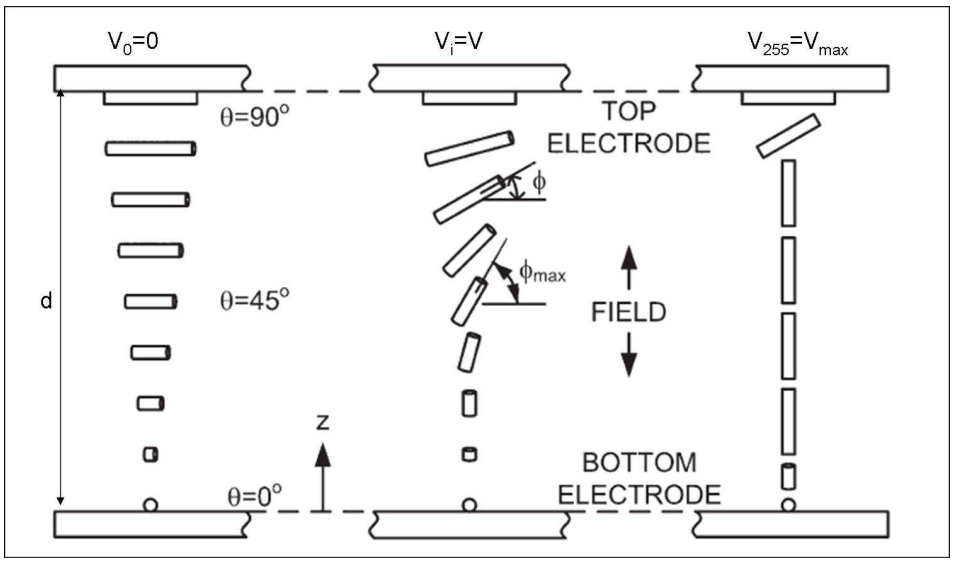

Figure 3.1: Scheme of three nematic twisted pixel-cells in a liquid crystal spatial light modulator: a fixed voltage reorients the LC-molecules resulting in a optical phase retardation experienced by the laser beam traveling through the cell; larger is the applied voltage level, larger will be the amount of LC reorienting.

corresponds to a discrete phase retardation value $\Delta\Phi_m$ (or simply Φ_m for brevity) added to optical phase of the incoming light locally, at each pixel position $\mathbf{r}_{ij}$. By addressing a phase profile $\Phi_{\mathbf{r}_{ij}}$ to the SLM-display via computer is therefore possible to determine the optical phase profile of the incoming beam properly expanded in order to cover the overall modulating surface of the SLM. The original Gaussian laser beam may be assumed as a plane wave. Due to the LC configuration into each pixel-cell, only vertically linear polarized light can experiment a phase retardation profile.

In a reflective SLM-display the electronic backplate is coated with a reflective substrate of silicon so that the light traveling trough the LC-cells are backreflected without affecting the overall behavior of the outgoing beam. The phase modulation

governed by the spatial light modulator may be transformed in amplitude profile modulation by adding a polarization analyzer in the path of the outgoing beam. By traveling through the cell, the vertical polarization component of a 45° linear polarized incident beam experiments a polarization profile depending on the phase profile provided by the array of LC pixel-cells, whereas the parallel polarization component results unaffected. Therefore, according to Malus law [Born 1980], after the vertically polarizing analyzer, the incident light will possess an amplitude profile.

The LC-spatial light modulator employed in this work is the HoloEye Photonics LC-R 3000. The system is based on a high resolution WUXGA LCoS display of 1920×1200 pixels with twisted-nematic cells. The SLM permits a modulation in the visible range $\sim (650 \div 400)nm$. It can be used to modulate light spatially in amplitude and phase, where the modulation function can be addressed electrically by a computer with a frame rate of 120 Hz. The square pixel-cell size is $9.5\mu m$, whereas the filling factor of the display is 92%, on an imaged array of 19.01×11.40 mm, and with a phase modulation ranging between 0 and 2π with 256 discrete levels.

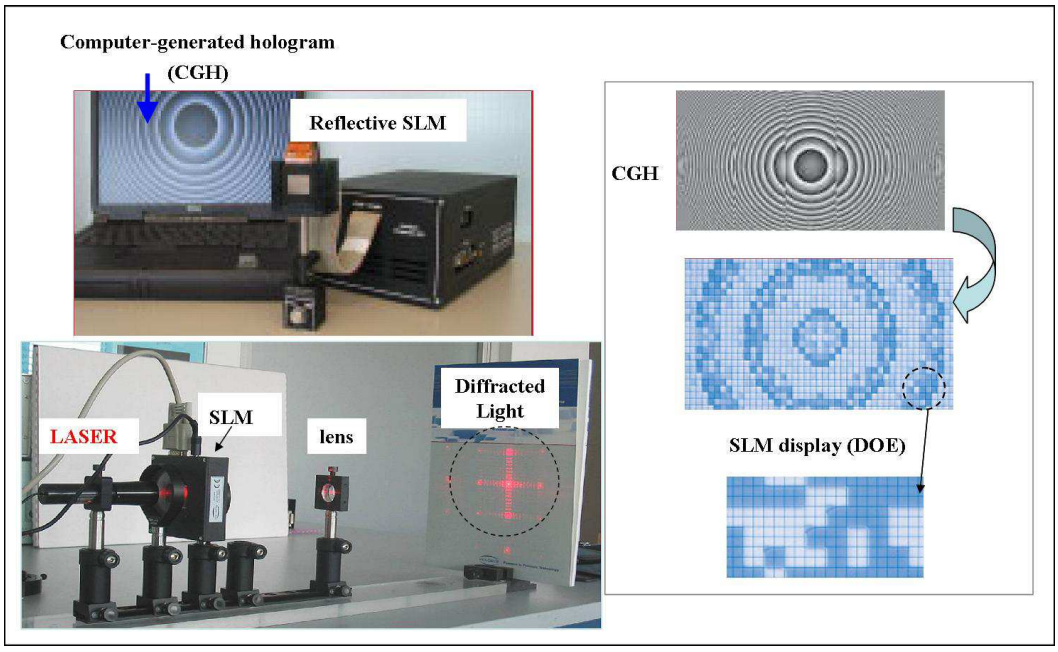

Figure 3.2: Example of a reflective spatial light modulator driven via computer (left upper half); a typical modulation of the intensity distribution provided by a transmission SLM; detail of the SLM-display encoding a CGH designed as Fresnel lens (flat lens).

The phase profiles addressed to the SLM-display are intensity images with 256 grey levels (8-bit images), each of which corresponds to a certain voltage level resulting in a phase retardation added to to optical phase of the incident beam. This correspondence permits to directly represent the phase-only holograms as intensity

images on the display of the computer driving the spatial light modulator (see Fig. 3.2). The design of the hologram is previously computed with particular algorithms in order to determine the optical phase profile of the beam to be modulated, as discussed in the next section. The hologram is therefore called computer-generated (CGH). The display of the SLM is the optical element that translates the CGH into a the desired DOE. In Fig. 3.2 a typical example of CGH depicted as intensity image is shown (left upper half). A typical modulation of the intensity distribution provided by a transmission SLM, that produces in the Fourier plane of a reconstructing lens a cross-like intensity profile, is also shown (left bottom half). In the same figure, on the right, the SLM-display representing a CGH is also shown: the CGH encodes in this case a Fresnel lens (flat lens) [Soifer 2002]. In fact, computer-generated holograms are able to reproduce almost any desired phase or amplitude optical element by designing their phase or amplitude profile, conventional element like a Fresnel lens, a cylindrical lens etc., or complex optical elements not achievable in a standard way.

3.1.3 Design of the Holograms

Computer-generated holography, typically, is based on the Fourier holography principle (other approaches may be adopted as discussed later on, also used in this work). The amplitude or/and phase holograms are calculated so that the beam, after diffraction, possesses the desired intensity distribution (or a particular amplitude and phase profile too), into the Fourier plane of a *reconstructing lens*, or into the far field. The reconstructing lens may be a simple lens or a microscope objective, or a more complex optical system. However the Fourier plane of this system, determined depending on the experimental situation treated, corresponds to the plane in which the beam outgoing from the CGH plane, that is the incident plane wave (approximation of the experimental laser beam) modified by the the phase profile provided by the SLM, is Fourier transformed.

In the left part of Fig. 3.3 two examples of intensity images or CGHs are shown, together with a detail of the reflective SLM-display LCR 3000. The central part of the same figure shows the basic scheme of the Fourier holography in which the CGH permits to create an arbitrary intensity distribution of light like those shown in the right part of the figure, that are an array of light spots (inset 1) and a target-like design (inset 2), just to give an idea of the potential design of the holograms and the resulting intensity profiles that can be encoded. Fourier holography is well known in literature (see [Hariharan 1984] [Goodman 1996] for details). Here, I want only to highlight the basic marks of the theory in order to describe the holographic process used in this thesis. The desired irradiance profile which induces the photopolymerization in the Fourier Transform (FT) plane of the sample (Fig. 3.3), is determined by the optical electric field of amplitude $E_{in}(\mathbf{r})$ in the input plane of the reconstructing lens (microscope objective or a positive focal lens etc.) of focal length f. As known by scalar diffraction theory, in the FT writing-focal plane the

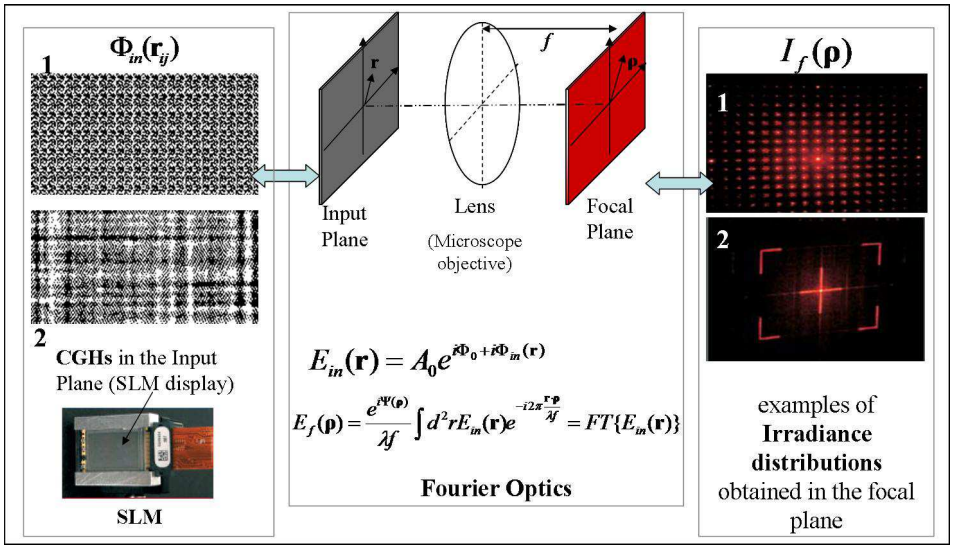

Figure 3.3: Two examples of CGHs are shown (left upper), together with a detail of the reflective SLM-display (left bottom). (Center) schematic representation of a Fourier holographic process: monochromatic light is incident on the input plane, a lens of focal length f projects the Fourier transform of the incident light's wavefront onto the focal plane; (insets on the right) intensity profiles encoded by the CGHs indicated as 1 and 2, respectively: an array of light spots (1) and a target-like design (2).

irradiance profile is related to the input field by the Fourier Transform relations

$$E_{in}(\mathbf{r}) = A_0 \exp[i\Phi_0 + i\Phi_{in}(\mathbf{r})], \tag{3.2}$$

$$\begin{aligned} E_f(\rho) &= A_f(\rho) \exp \Phi_f(\rho) && (3.3)\\ &= \frac{e^{i\Psi(\rho)}}{\lambda f} \int \mathrm{d}r^2 E_{in}(\mathbf{r}) \exp(-i2\pi \frac{\mathbf{r}\cdot\rho}{\lambda f}) && (3.4)\\ &= \mathcal{FT}\{E_{in}(\mathbf{r})\} && (3.5) \end{aligned}$$

$$\begin{aligned} E_{in}(\mathbf{r}) &= \frac{1}{\lambda f} \int \mathrm{d}\rho^2 e^{i\Psi(\rho)} E_f(\rho) \exp(i2\pi \frac{\mathbf{r}\cdot\rho}{\lambda f}) && (3.6)\\ &= \mathcal{FT}^{-1}\{E_f(\rho)\}, && (3.7) \end{aligned}$$

where A_0 and Φ_0 are, respectively, the amplitude and the phase profile of the incident laser beam, that are supposed to be uniform. Whereas $\Phi_{in}(\mathbf{r})$ is the phase profile, i.e. the phase-only hologram (or CGH) added to the incident beam by means of the electrically addressed liquid crystal display. The field in the FT focal plane, and hence the irradiance pattern $I_f(\rho) = |E_f(\rho)|^2$, can be opportunely designed adding the suitable phase profile $\Phi_{in}(\mathbf{r})$ to the incident beam impinging on the input plane (Fig. 3.3). For real applications the hologram consists of single pixels, and this enables us to use a Discrete Fourier Transform (DFT), which can be calculated via a Fast-Fourier Transform (FFT) algorithm, instead of the Fourier integral in Eq. 3.1.3.

The phase $\Psi(\rho)$ represents an additional phase profile due to the lens geometry and does not contribute to the irradiance distribution I_f, hence may be ignored without loss of generality [Goodman 1996]. Moreover, equation 3.1.3 states, as a result of the mathematical properties of the Fourier Transform, that any displacement of the hologram into the input plane, for instance due to mechanical vibrations of the SLM display reproducing the phase-only hologram, does not contribute to the irradiance profile, adding, in fact, an overall phase factor which does not influence the writing pattern.

We are assuming that the holograms consist of $N \times M$ point-like pixels on a regular array, which can modulate only the phase of the input beam. In fact, even if it is possible to exploit amplitude-only holograms influencing the amplitude of the incident laser beam, or complex holograms modulating both amplitude and phase, we are mainly concerned with the phase-only holograms, since they have a higher diffraction efficiency [Soifer 2002].

According to Whittaker-Shannon sampling theorem (see [Goodman 1996] and [Goodman 1996]) the pixel size l_f in the FT plane is related to the pixel size l_{in} in the input plane in accordance with the relation

$$l_f = \frac{\lambda f}{N l_{in}},$$

, where N represents the total number of pixels on the hologram side, and hence is connected with the spatial resolution of the hologram. With $l_f \simeq \lambda/2$ high resolution patterns are achievable, whereby large values of N are tough necessary to obtain large areas of optical curing, i.e., at least, one millimeter for probable and reliable applications.

Nonetheless the focal length f of the reconstructing lens cannot be chosen without deserving attention to the magnification demanded and the sizes of the input pupil if it is a microscope objective. Then, with the aid of a simple system of two relay lenses, it is possible to change the value of the input pixel size l_{in} in order to adapt it to the more suitable optical configuration and respond to the experimental requirements of the writing pattern. In other words, if holograms with higher resolution are necessary then those reproducible with the liquid crystal display of the SLM, then the relay lenses allow to adapt the optimal spatial resolution required into the FT focal plane with the linear dimensions of the hologram generating the irradiance profile, reproducing a conjugate hologram (CGH^*) in the back aperture of the microscope objective. The sizes of the cured area will also depend on the numerical aperture of this reconstructing objective.

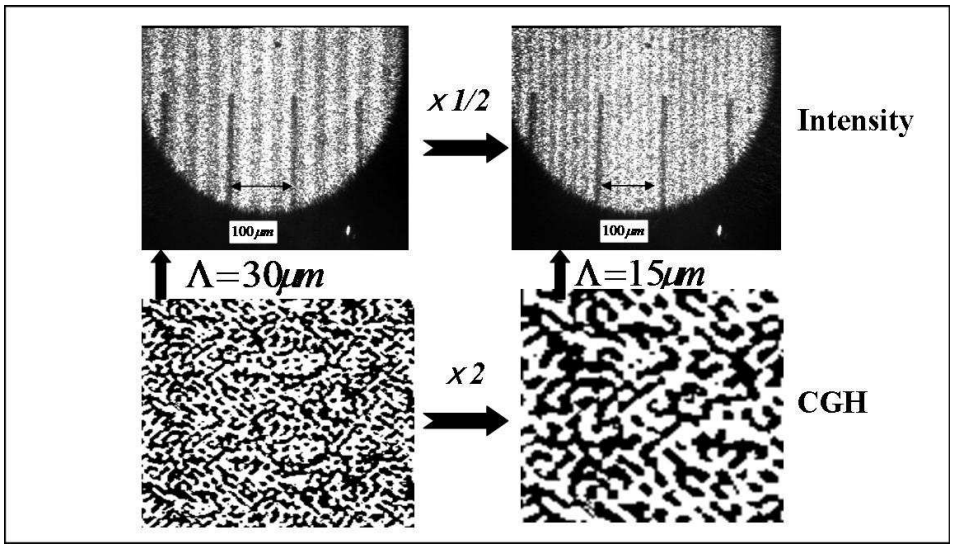

Figure 3.4: Effect of resizing in video real-time a CGH on a 1-D periodic intensity profile.

The resizing of the holograms in video real-time permits to vary the length scale of the irradiance pattern without any mechanical motion or realignment of the optics in the experimental setup, this thanks to the unique properties of the Fourier transform, implicit in Eq. and . In Fig. 3.4 an example of the resizing effect is shown. In the bottom half of the figure a CGH encoding a periodic intensity distribution with a square wave modulation is depicted. In the bottom half of the figure the resulting intensity profile produced by the SLM in the FT plane of

the optical system is presented, monitored with a CCD camera (the details of the experimental setup will be discussed later on). Despite the noisy aspect of the intensity profile obtained, which was due to the low efficiency of the particular CGH adopted, it is important to highlight how changing the resolution of the CGH in video of a factor of 2, the effect is transferred inversely to the intensity profile in which the spacing pitch Λ becomes clearly one half of the original value without any mechanical motion or realignment. In a two-beam holography experiment a square wave modulation of the intensity profile cannot be achieved, but despite this aspect, a decreasing of the grating pitch would require an increasing of the angular separation between the beams, with the consequent problem of redesigning the experimental setup. Moreover, the pattern can be changed completely in a new one simply by addressing a new CGH to the programmable SLM with a rate up to 120 *Hz*. This property will be true despite the experimental configuration adopted in this thesis work, i.e. the FHS, DIW or IS.

In the case of the Fourier holography scheme, however, the relay lenses provide, if necessary for practical requirements, a further fine, continuous, adjustment of the length scale of the irradiance profile in the FT plane, varying the distance between the lenses. Moreover, they permit a certain degree of control of the writing pattern which results before the back aperture of the microscope objective, allowing for instance to stop the undiffracted light reflected from the SLM. In order to do this, however, it is preferable to direct the diffracted light, and hence the writing pattern, along a different path, adding a linear phase profile to the CG hologram, parting in this way the diffracted light from the undiffracted one.

A great advantage of using a spatial light modulator with computer generated holograms, in fact, is the potentiality of manipulating the phase profile of the incident beam for different purposes simultaneously, possibly even correcting the aberrations introduced by the optical setup.

As I will discuss in the next sections, it is possible to design computer-generated holograms that may encode the desired irradiance distribution, or in general the desired properties of the beam such as the phase or amplitude profile or both, in a given region of space independently form the experimental optical setup adopted, provided that the contributions of all the optical elements involved are taken into account for the calculation of the holograms.

It is possible, as for instance, to create phase-only holograms encoding the amplitude information of the desired beam without the need for complex holograms as demonstrated by Davis [Davis 1999]. It is possible to reconstruct near-perfect holograms that permit to control both the phase and amplitude of the beam by using a SLM, as discussed in [Jesacher 2008]. By adding several holographic focusing lenses with different focal lengths in the design of a kinoform, 3-D projections are also achievable as demonstrated theoretically by Haist [Haist 1997] and experimentally by Sinclair [Sinclair 2004].

The basic marks of the computer designing of Fourier holograms will permit a better comprehension of the other computer-generated holograms experimentally adopted in this work.

3.1.3.1 Adaptive-Additive Algorithm

We are now mainly concerned with the designing and computing of the holograms, whereas the experimental details of the optical setup concerning the fabrication of structures with different arrangements of the liquid crystal-polymer materials are reported in the next sections.

The basic principle is to calculate the suitable phase profile $\Phi_{in}(\mathbf{r})$ of equation 3.2 that permits to produce the desired irradiance profile $I_f(\rho)$, that is given by the square modulus of equation 3.1.3. Obviously, it is a non linear problem, but it can be solved numerically by subsequent iterations and approximations. The digital holographic profile is computed with an iterative algorithm known as *Adaptive-Additive algorithm* (AA), and each step of the iteration requires a two-dimensional (direct/inverse) Fast Fourier Transform routine. Other algorithms may be applied for the hologram computation like Gerchberg-Saxton or genetic algorithms (the book of Soifer is a good reference for details about this issue [Soifer 2002]), but I found better results with the fast AA algorithm that I modified to increase the efficiency of the generated holograms.

The basic problem in the calculation of a Fourier computer-generated hologram $\Phi_{in}(\mathbf{r}_{ij})$, where $\mathbf{r}_{ij}$ indicates the position of the $(i,j)-$pixel, is the optimization of the degrees of freedom of the 2-D hologram so that its Fourier transform could yield the desired light distribution $I_f(\rho)$. The AA algorithm solves the problem of CGH computing by permanently changing between the focal and the hologram plane via Fourier transform and inverse Fourier transform, exploring, numerically, the space of degenerate phase profiles which can encode, with a suitable phase modulation of the incident beam, the desired irradiance profile in the focal plane. Since the maximum resolution of the SLM employed may be very high, supporting holograms of 1920×1200 pixels, the calculation of the double-precision numerical matrices necessitates fast algorithms. I have obtained very good results with an iterative algorithm based on the FFT routines of MathWorks Matlab 7.0.1, succeeding to complete the whole iterative process in a few seconds or tens of seconds, depending on the number of iterations required for convergence, which typically did not exceed 10 iterations. In Fig. 3.5 the flow chart of the algorithm is depicted. In the example a target-like intensity distribution, that has been encoded into a Fourier phase-only hologram, is shown: the experimental setup simulated is a Fourier holographic scheme as depicted in the central part of Fig. 3.3; starting from a random phase profile at the input plane (the input CGH), the output CGH permits to obtain the desired intensity profile in the Fourier plane of the experimental setup.

The AA algorithm consists of mixing the desired amplitude $A_f(\rho)$ in the focal plane with the n-th computed amplitude $A_n^f(\rho)$ in each iteration, adding the two terms with a suitable choice of the mixing coefficient β. A good choice for β may be in the range from 0.3 to 0.7. With the inverse FFT, in fact, at each iteration, the information encoded in the amplitude is partially transferred to the phase profile $\Phi_{in}(\mathbf{r}_{ij})$. Starting with a random phase profile $\Phi_0^{in}(\mathbf{r}_{ij})$ $(n = 0)$ in the hologram

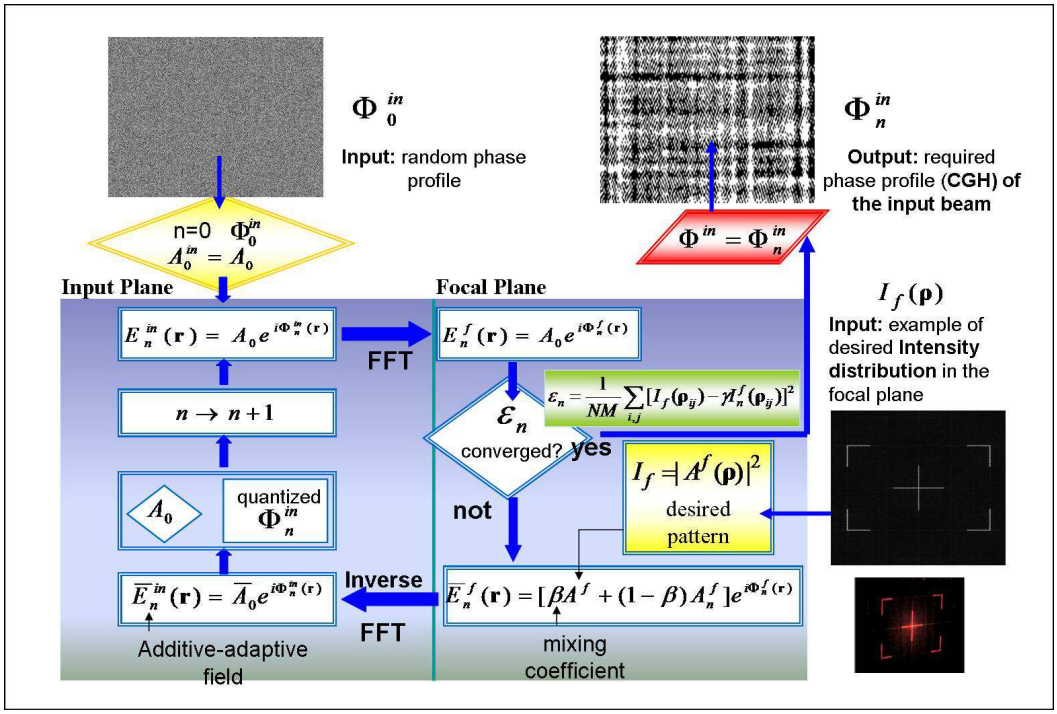

Figure 3.5: Flow chart of the AA algorithm: in the example, a target-like intensity distribution has been encoded into a Fourier phase-only hologram (the output CGH) starting from a random phase profile at the input plane (the input CGH).

plane, the AA computes the direct FFT of the input field

$$E_n^{in}(\mathbf{r}) = A_0 \exp[i\Phi_n^{in}(\mathbf{r})]$$

imposing a uniform input amplitude $A_n^{in}(\mathbf{r}) = A_0$. This restriction is imposed at each iteration in order to find the phase-only hologram required. The complex field obtained

$$E_n^f(\rho) = A_n^{in}(\rho) \exp[i\Phi_n^f(\rho)]$$

in the focal plane produces an intensity distribution $I_n^f(\rho) = |E_n^f(\rho)|^2$ which is compared with the desired irradiance profile $I_f(\rho)$ by computing the mean squared error sum

$$\varepsilon_n = \frac{1}{NM} \sum_{i,j} [I_f(\rho_{ij}) - \gamma I_n^f(\rho_{ij})]^2,$$

over the whole array of $N \times M$ pixels of indices (i,j), where the coefficient γ accounts for different overall intensities. The error is reduced computing the inverse Fourier transform of the adapted field $\bar{E_n}^f(\rho)$, defined as

$$\bar{E_n}^f(\rho) = [\beta A_f(\rho) + (1-\beta) A_n^f(\rho)] \exp[i\Phi_n^f(\rho)]. \tag{3.8}$$

The Fourier transform of the adapted field provides, in fact, the new starting field $\bar{E_{in}}^f = \bar{A}_0 \exp[i\Phi_n^{in}(\mathbf{r})]$ in the hologram plane after having imposed the restriction of uniform amplitude $\bar{A}_0$ and the quantization condition. In fact, the AA algorithm generates a phase profile which vary almost continuously between 0 and 2π, whereas the experimental holograms supported by the SLM may have only a discrete, maximum, set of 256 phase levels ranging from 0 and 2π, represented with the grey levels of an intensity image. According to this, the optimization of the holograms requires to quantize, opportunely, the phase profile obtained in each iteration. At this stage, the new phase-only hologram $\Phi_n^{in}(\mathbf{r}_{ij})$ will produce an improved intensity distribution. The cycle is repeated until the square mean error ε_n converges to within an acceptable tolerance. For practical purposes it is also possible to visualize the real-time formation of the intensity pattern (Fig. 3.6).

As aforementioned, the reconstructing lens realizes the desired irradiance pattern in the FT focal plane, hence the 'thickness' of the writing pattern will depend on the depth of field of the microscope objective (or other), related to the focal length f and the numerical aperture. We therefore need to account for it in designing the holograms and their spatial resolution. A very attractive alternative is the realization of 3-D irradiance distributions to pattern one- and two-dimensional dielectric modulations too. Moreover, in this way it could be possible to eliminate the uncertainty affecting the coincidence of the writing plane with the Fourier plane, an experimental drawback which could be, then, completely removed. However, the designing of three-dimensional patterns, introducing appropriate lens holograms [Haist 1997], requires more complicated calculations that I will not use in this work.

In addiction, the phase jumps may produce undesired speckles (aliasing) in the reconstruction plane, decreasing the contrast and the overall quality of the writing

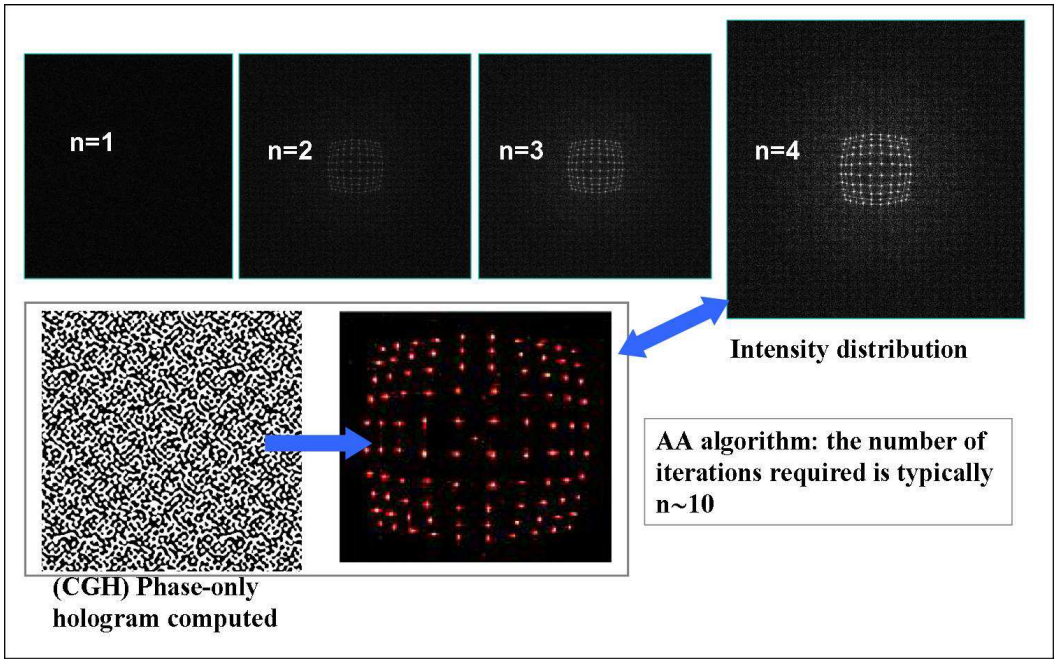

Figure 3.6: Example of intensity profile produced by a CGH after a few iterations using the AA algorithm: the intensity profiles consists of an irregular array of light spots.

pattern. Furthermore, the differences between the computed ideal phase profile and the experimental hologram addressed to the SLM display, decrease the efficiency of the hologram. The optimization of the holograms may require several techniques discussed in literature, that I will not mention here.

I found a different useful approach to increase the efficiency of the holograms (the ratio between the intensity of the light diffracted from the hologram addressed to the SLM and the undiffracted light), that is based on the experience and on many empirical tests performed on the calculated holograms. One of the possibility is to substitute completely the desired amplitude information in the adaptive field of equation 3.8 by choosing the mixing coefficient $\beta = 1$, neglecting in this way the amplitude information A_n^f achieved by the FFT routine and maintaining the only phase contribution Φ_n^f. The phase information is mixed with the desired amplitude information at each iteration and partially transferred to the phase profile of the input plane, that is the CGH, producing a higher efficiency. Moreover, I found convenient to increase the contrast of the desired amplitude information in the focal plane by adding an real exponent α, typically equal to 2, to the adaptive field, so that equation 3.8 becomes

$$\bar{E_n}^f(\rho) = A_f(\rho)^\alpha \exp[i\Phi_n^f(\rho)]. \tag{3.9}$$

In order to maintain to a constant value the overall amount of "energy" involved in the transfer from one field to the transformed one, I normalized each field or intensity expression to the total sum of the pixel values so that the calculated efficiency of the output CGH could correspond the experimental efficiency. Moreover, I applied a further restriction to the CGH in order to increase their efficiency. In the degenerate space of phase-only holograms encoding the desired intensity profile, the binary holograms (two grey level holograms) are example of holograms that produce the same intensity distribution either if they work as phase profiles either as amplitude profiles. I extended this restriction also to the 8-bit holograms having 256 grey levels by imposing a double cycle in the iteration. The intensity profile produced by the CGH at each iteration is first calculated starting from a phase-only hologram and then from an amplitude-only hologram that is obtained simply assuming the same design of the phase in the amplitude too. After a few iterations the CGH obtained produces the same intensity profile both as a phase and amplitude hologram.

By applying these simple modifications to the AA algorithm, the efficiency of the CGHs has been increased from $\sim (20\% \div 30\%)$ to $\sim (50\% \div 60\%)$ and the holograms were able to produce intensity profiles with a large contrast as we will see in the next section.

3.1.4 Experimental Setup (I): Fourier Holography Scheme

The scheme of the experimental setup employed to cure the photosensitive mixtures with the Fourier Holography approach is depicted in Fig. 3.7. The experimental parameters related to the optical curing process, that are the kind of mixture, the incident power and exposure time are summarized in Sec. 3.1.6. The FHS has been

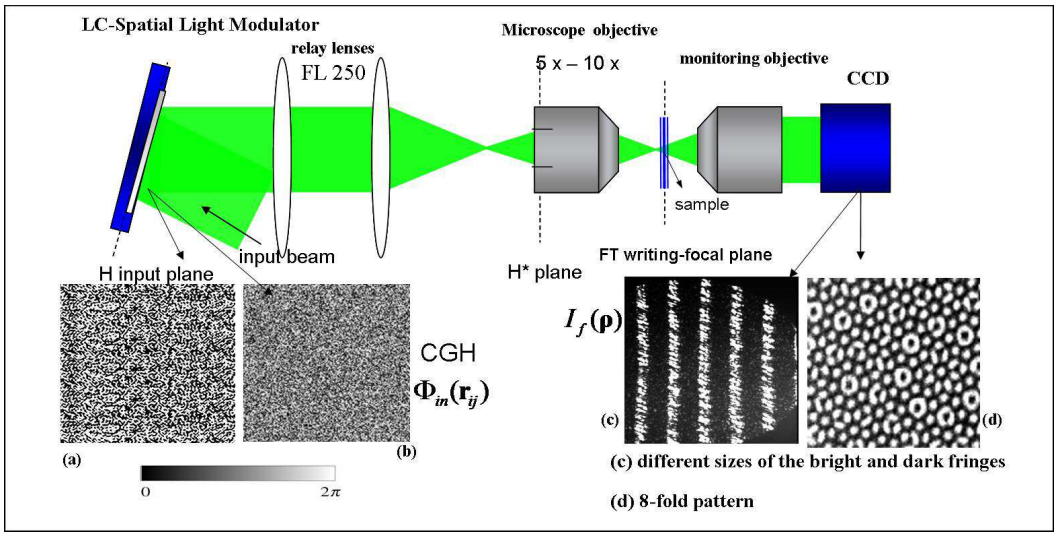

Figure 3.7: Experimental Scheme for Fourier Holography: the laser beam after being expanded and spatially filtered, impinges on a reflective SLM reproducing, in the H input plane, the CGH. Then the beam is projected by the relay lenses onto the conjugated plane H^*, which lies onto the input pupil of the microscope objective. Hence, the writing irradiance pattern is reconstructed in the FT writing-focal plane. A second microscope objective permits the real-time monitoring of the writing pattern with a CCD camera. Figures (a) and (b) show the phase-only holograms computed to design, respectively, the irradiance profile (c) and (d): a 1-D square pattern with different sizes of the dark and bright fringes (c), and a quasiperiodic octagonal irradiance profile (d).

the first holographic approach based on the use of a spatial light modulator adopted in this thesis work. The Gaussian input laser beam (at $\lambda = 532nm$) is spatially filtered with a microscope objective-pinhole system (not shown in Fig. 3.7) and expanded before it impinges on the spatial light modulator, so to utilize entirely its modulating surface and to ensuring the best efficiency. The digital discretized CGH was computed with the AA algorithm and then addressed as intensity image with 256 levels of grey to the SLM display, as described in the previous section.

The desired irradiance profile I_f is reconstructed at the back focal plane of a microscope objective, where the sample to be cured is placed. Due to the Fourier transform properties, any displacement of the hologram plane, produced, for instance, by environmental vibrations, does not affect the irradiance profile at least on a micrometer scale. The phase-only hologram in the H input plane is transferred to the input pupil of the microscope objective, in the H^* conjugate plane, by means of the relay lenses (Fig. 3.7). The large focal length $(150 - 200mm)$ of the lenses minimize spherical aberrations and coma. They permit also a fine adjustment of the hologram size in the H^* plane and hence of the grating spacing in the FT focal plane, with a sensitivity of about $100nm$. A second microscope objective permits the real-time monitoring of the writing pattern with a CCD camera.

The experimental holographic setup has been previously studied and designed using a software that I developed for this task by employing the Imaging Processing Tool of MathWorks Mathlab 7.0.1 and the Wolfram Research softwares Mathematica 5.0 and 6.0. The propagation through the whole experimental setup and the diffraction by the optical elements and by the CGHs addressed to the SLM-display have been treated first within the framework of the Geometric Optics approximation and then within the framework of the Fresnel scalar diffraction theory. Every section of the experimental setup has been included using the related diffraction integral associated to the particular optical element involved during the propagation of the laser beam. As for instance, in Fig. 3.8 the scheme of the propagation of the optical field trough the experimental system, starting from the input plane of the SLM, is depicted. The lenses L_1 and L_2 of focal lengths f_1 and f_2, respectively, project the input beam onto the Fourier plane in which the photosensitive sample is placed. By applying the operator properties described by Goodman [Goodman 1996], the integral operator $R[d_i]$ of free-space propagation may be transformed in combination with the lens operator $\mathcal{Q}[c]$, corresponding to the multiplication of a phase factor and defined as

$$\mathcal{Q}[c] = \exp\left[i\frac{\pi}{\lambda}\Delta^2 c\left(x^2 + y^2\right)\right] \tag{3.10}$$

where the variable $c = -1/f$ for a positive lens of focal f and where $x = r\cos\theta$ and $y = r\sin\theta$. Therefore $R[d]$ becomes

$$\mathcal{R}[d] = \mathcal{FT}^{-1}\mathcal{Q}\left[-\lambda^2 d\right]\mathcal{FT}, \tag{3.11}$$

where the symbols $\mathcal{FT}$ and $\mathcal{FT}^{-1}$ indicate the application of the direct and inverse Fourier transform integral operators, respectively. The parameter Δ is the sampling factor and defines the pixel size of the spatial light modulator which determines

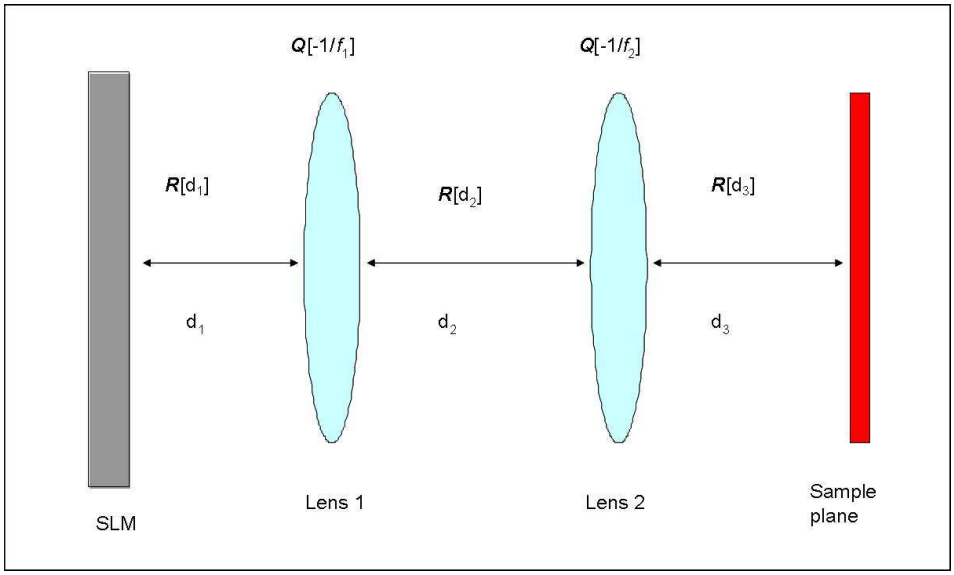

Figure 3.8: Representation of the diffraction operators associated to the propagation paths and the lenses used to project the CGH in the Fourier plane in which the sample is placed.

the discretization of the optical field and hologram. Attention must be paid to the length of scale associated to the argument of the direct and inverse Fourier transforms so that the results obtained from the diffraction simulation could agree with the experimental parameters. For this reason, the sampling Δ is crucial to obtain good results. The Fourier transforms are calculated with a two-dimensional Fast Fourier transform routine. The laser beam with a Gaussian profile is spatially filtered and expanded, so that the optical field impinging of the SLM is assumed to be a uniform plane wave. The operator $\mathcal{S}$ associated to the SLM is represented by transforming the incident plane wave in a complex field according to

$$\mathcal{S}\left[U_{in}(x,y)\right] = A\left(\frac{x}{\Delta},\frac{y}{\Delta}\right)\exp\left[i\Phi_{in}\left(\frac{x}{\Delta},\frac{y}{\Delta}\right)\right].$$

If the CGH is a phase-only hologram then the amplitude of the beam immediately after the SLM plane may be assumed uniform, that is $A\left(\frac{x}{\Delta},\frac{y}{\Delta}\right) = A_0$, and only the phase modulation provided by the CGH is considered. Although the SLM should work as a phase-only modulator, I found better results from the simulation of the holographic process by imposing a non uniform amplitude profile into $\mathcal{S}$. In fact, the theoretical simulations have given better results in reproducing the experimental optical modulation by supposing an amplitude contribution. The reason for this behavior of the SLM is still not clear. It is our opinion that there is a residual amplitude modulation due the pixel cell configuration and composition, as it has resulted from a characterization of the amplitude modulation produced by the SLM-display that the constructor HoloEye has provided to us. The data sheets shown in

Fig. 3.9 indicate an amplitude modulation depending on the grey level addressed to pixel cell of about $\sim 20\%$ even without the polarization analyzer after the SLM. Given these characteristics of our SLM, I considered an amplitude contribution

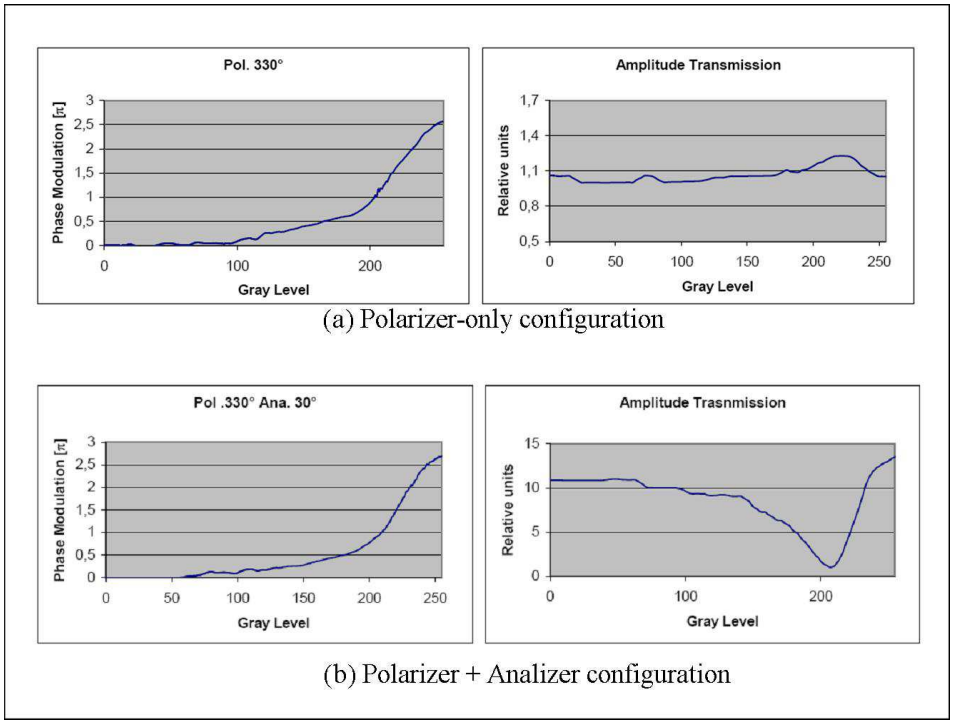

Figure 3.9: (a) Phase and amplitude modulations as a function of the grey level of the pixels (uniform over all the display) for a polarized laser beam impinging on the SLM, but without the analyzer after it; (b) similar characterization for an incident polarized beam but with the analyzer after the SLM.

in the calculation of the holograms. As described in Sec. 3.1.3.1, by imposing the condition of a simultaneous amplitude and phase modulation on the computed holograms, the efficiency of the CGHs that I realized increased. This circumstance may be related to the characteristics of the SLM employed in my experiment. In Fig. 3.10 two examples of the simulated intensity profiles of the beam after the lenses L_1 and L_2 are shown. In (a) a phase-amplitude combined CGH is used whereas in (b) a phase-only CGH. The desired intensity profile is represented in (c), calculated supposing an 8-beam interference (as described in the next section). The intensity profiles are calculated with the operator procedure described above with a resolution of 400×400 pixels. Despite the noisy aspect of the images, that was due to the low sampling and resolution in the calculation and to the magnification ~ 0.2 of the couple of lenses, the phase-amplitude CGH results in accordance with the desired profile.

In addition to the holographic setup of Figure 3.7, in the fabrication of one-dimensional gratings with a grating spacing $\Lambda \sim 2\mu m$, a second laser at $632nm$ is

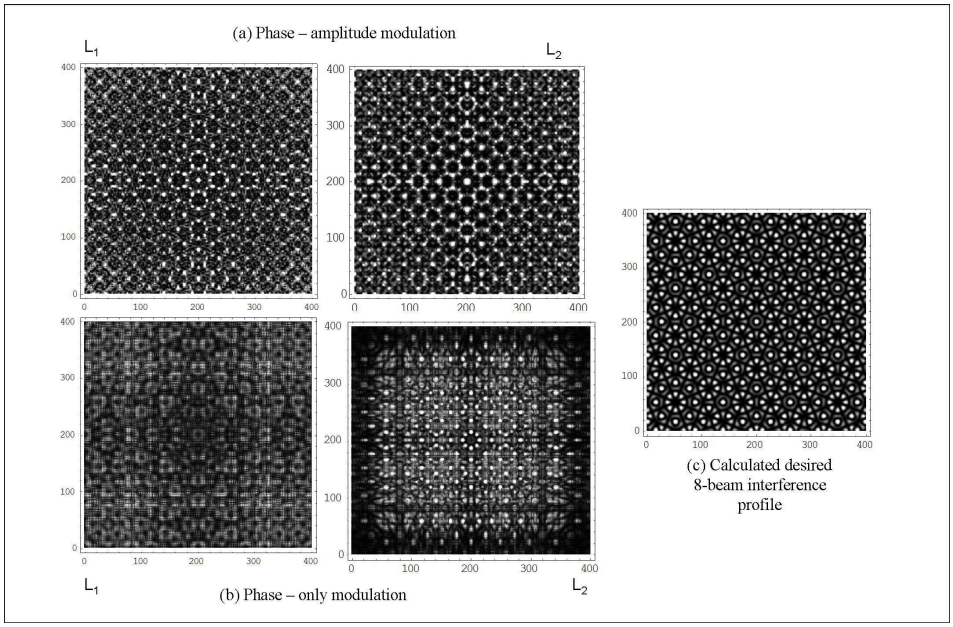

Figure 3.10: Calculated intensity profiles of the beam after the lenses L_1 and L_2: in (a) a phase-amplitude combined CGH is used whereas in (b) a phase-only CGH is supposed. The desired 8-beam interference profile is represented in (c).

used to illuminate the sample and study the formation of the grating by collecting the diffracted light from it by using a photodiode placed at the theoretical Bragg angle of the grating. In the first writing attempts, however, the grating spacing was too large to permit a sufficient deviation of the diffracted light from the undiffracted, therefore it was not possible at that stage to study the dynamics formation with this simple scheme. Moreover, this kind of real-time control is not useful when the structures to realize are more complex, as in the case of 2-D quasiperiodic ones.

Several holograms $\Phi_{in}(\mathbf{r}_{ij})$ have been computed to realize different irradiance profiles $I_f(\rho)$, from a simple sinusoidal modulation or standard square 1-D modulation to more complex irradiance distributions. However, the scheme of Fourier holography has been mainly used to produce the one-dimensional gratings, the most simple structures achievable. Figure 3.7 shows, on the bottom, two examples of my holograms, obtained by adaptive-additive algorithm. The CGH in Fig. 3.7-(a) provides the irradiance profile represented in Fig. 3.7-(c) (photo acquired with a CCD camera), which shows a one-dimensional periodic square modulation with different sizes of the dark and bright fringes. The CGH in Fig. 3.7-(b) provides the 2-D quasiperiodic octagonal irradiance pattern, represented in Fig. 3.7-(d), which presents an 8-fold rotational symmetry.

The overall structure can be reconfigured real-time resizing the hologram via computer. By varying the scale factor of the phase profile with a magnification factor $\mathcal{M}$ in fact, the length-scale in the focal plane of the microscope objective changes

with an inverse magnification factor $\mathcal{M}^{-1}$. The effect of resizing the hologram on a 1-D square irradiance profile is represented in Fig. 3.4-(a-b). The grating pitch of the light pattern was changed from $\Lambda = 30\mu m$ (a) to $\Lambda = 15\mu m$ (b) by enlarging the original relative CGH of a scale factor of two.

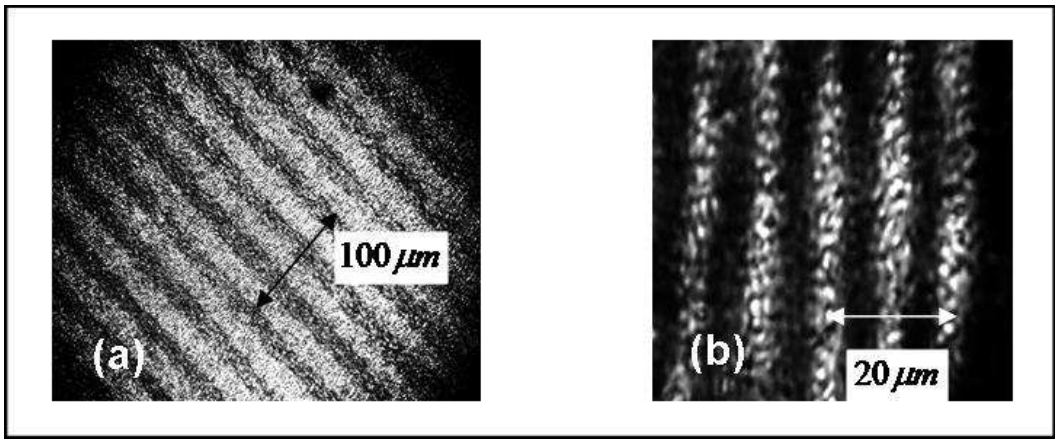

Figure 3.11: The images (a-b) show the result of the square-wave modulations of the LC content, and hence of the average refractive index, obtained by optical curing of the pre-polymer/LC mixtures with the CGH-patterns (the photos are taken using a polarized microscopy).

The first writing attempts regarded patterns with 1-D square and sinusoidal modulations. Two examples of gratings written into LC-polymeric mixtures are shown in Fig. 3.11-(a-b). Details of the photosensitive mixture are discussed in Sec. 3.1.6. The square-wave polymeric grating shown in Fig. 3.11-(a) corresponds to the irradiance distribution shown in Fig. 3.4-(a). A similar grating with a smaller period $\Lambda \simeq 10\mu m$ is shown in Fig. 3.11-(b). The quite large values of the grating spacing obtained in the preliminary writing patterns are not a limitation of the CGH technique. In fact, the modulation in the irradiance profile, realized with several pixel sizes (typically $1 \div 2\mu m$), was produced with a number of pixels per fringe of $10 \div 20$, whereas the microscope objectives employed as the reconstructing lens had a 5×-10× magnification. Limited by the optical setup, the cured area had, typically, a linear dimension of $\sim 1mm$ whereas the intensity of the writing beam was of the order of $2 \div 10mW$ at the sample position. The exposure times ranged from about $30s$ to $300s$.

The limitations in writing these irradiance patterns with a large period on the photosensitive mixtures were due to the low contrast of the intensity distributions produced by the CGHs, which was typically $4 : 1$ and only in a few cases increased to $25 : 1$. This was mainly related to the low diffraction efficiency of the first CGHs that I realized, which was typically less of 30%, and then to the high amount of undiffracted light, which was not prevented, in my first experimental tests, from disturbing the writing pattern. Moreover, the limited depth of field of the microscope

objective (about $60\mu m$) yielded a difficult matching between the writing plane and the position of the sample cell (the cell thicknesses ranged from a few microns to tens of microns). Furthermore, the presence of speckle (aliasing) [Haist 1997] in the irradiance profile decreased the overall quality and the contrast of the writing patterns.

Overcoming these experimental difficulties has been possible by improving the efficiency of the computed CGHs, as described in the previous section, and by adopting a second experimental scheme, that I called Direct Writing Method, which has permitted to obtain very interesting results.

3.1.5 Experimental Setup (II): Direct Writing Method

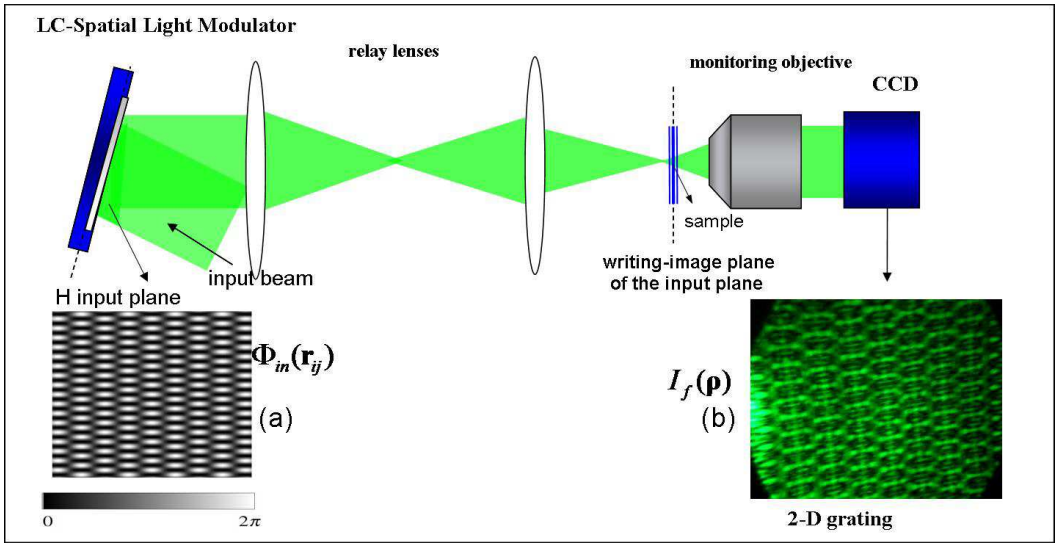

Figure 3.12: Experimental scheme of the Direct Writing Method: the laser beam after being expanded and spatially filtered, impinges on a reflective SLM reproducing, in the H input plane, the CGH. Then the beam is projected by the relay lenses onto the conjugated plane CGH^* corresponding to the sample plane in which the writing irradiance pattern is directly reconstructed. A second microscope objective permits the real-time monitoring of the writing pattern with a CCD camera. The inset (a) shows the phase-only hologram computed to encode the irradiance profile in the inset (b): a 2-D periodic pattern.

In the Direct Writing Method the holograms addressed to the SLM are not related to the desired writing intensity profiles through the Fourier relations of equations 3.2 and 3.1.3. As aforementioned in Sec. 3.1.3, in fact, it is possible to design computer-generated holograms that produce the desired irradiance profile or that are able to produce the desired amplitude and phase profile in a given region of space that do not work in the Fourier plane. They can produce the writing intensity in another plane if in the calculation of the holograms this requirement is

properly taken into account. In the direct writing method the hologram is generated in order to produce the intensity profile in the image plane of the SLM-display (H input plane of Fig. 3.12). In other words, the writing plane, in which the sample is placed, is chosen to be coincident with the conjugate plane of the hologram. In the Fourier holographic method the CGH is firstly projected, through the relay lenses of Fig. 3.7, into its conjugate plane CGH^* coincident with input pupil of a microscope objective that acts as the reconstructing lens, so that the writing intensity is reconstructed in its Fourier plane. In the DWM the problem is inverted in a certain sense. In fact, the writing plane corresponds to the conjugate plane CGH^* of the H input plane, directly. It corresponds to the image plane of the CGH with respect to a particular imaging system that has the role of reducing the scale length to permit the formation of a micrometer structure. The imaging system is realized through the relay lenses of Fig. 3.12. Therefore, the CGH is designed in order to reproduce the desired intensity profile in the image plane of the relay lenses. A homogenous mixture of photopolymer, liquid crystal, and photo-initiator is exposed to the required irradiance profile at the conjugate plane of the hologram. The lateral magnification of the imaging system determines the scale length of the pattern to be written.

As discussed by Davies et al. [Davis 1999], it is possible to encode the desired amplitude profile $A(x,y)$ directly into a phase-only hologram $\Phi(x,y)$ with a "direct" method that avoids the need of the numerical iterations. The principle is that of modulating the diffraction efficiency of the phase-only hologram along its profile by taking the product $\Phi(x,y)A(x,y)$. In this way, the amplitude profile represents the function modulating the efficiency of diffraction. Let us assume that we want to encode the general complex function

$$F(x,y) = A(x,y)\exp[i\Phi(x,y)].$$

They proposed the generation of the following phase-only function:

$$F(x,y) = \exp[iA(x,y)\Phi(x,y)],$$

by taking the new hologram as the multiplication of the amplitude and phase information. By expanding the above relation in a Fourier series we find the original phase function $\Phi(x,y)$ in the first order with an amplitude modulation that is approximately equal to the desired amplitude function $A(x,y)$. Moreover, the error in reproducing exactly the amplitude information may taken into account so that the distortion from the desired profile may be corrected.

In a similar way, the desired amplitude information may be addressed directly to the SLM as a CGH, neglecting the phase profile that may be uniform for our purposes of writing in which only the intensity profile related to the amplitude in needed. In the inset (a) of Fig. 3.12, a phase profile $\Phi(\mathbf{r}_{ij}) = A(\mathbf{r}_{ij})$ coincident with the amplitude information that we want to reproduce is shown. It represents a 2-D grating with an different period along the x and y direction, that is an 2-D rectangular structure. In the inset (b) of Fig. 3.12, the experimental resulting intensity profile is shown. It clearly demonstrates the same structure encoded into the

phase hologram. This simple approach may be generalized by describing the optical system using the scalar diffraction theory and then calculating the exact phase hologram able to reproduce the desired amplitude profile in the image plane of the lenses of Fig. 3.12. This is what I did numerically modifying the Adaptive-Additive algorithm to consider the propagation through the whole optical system using the diffraction theory and the operators defined in equations 3.10 and 3.11 instead of the single Fourier transform needed in the scheme of Fourier holography. As I explained in the previous section, by manipulating the free-space propagation integral it is possible to describe the whole path of the incident wave by using a combination of the lens phase factors and the Fourier transform integrals, just paying attention to the choice of the scale factors involved in the different steps. The FT integrals are then calculated through a two-dimensional Fast Fourier transform (FFT) algorithm that simplifies enormously the computational problem. As described before, also in the FHS this rigorous description of the propagation process has been applied for the CGH generation in order to take into account possible experimental deviations from the theoretical behavior introduced by the employment of the relay lenses of Fig. 3.7. Moreover, the experimental situation described in Fig. 3.8 (the optical train used in the FHS) is practically coincident with the direct writing setup, provided that the CGH is modified in the proper manner and that the relay lenses are used now as the imaging system, that may be done simply changing the parameters of the optical apparatus, that are the focal lengths f_i of the lenses and the distances d_i between the various optical elements.

Let us discuss in details the experimental setup represented in Fig. 3.12. Like in the FHS, the laser source is a Coherent doubled-frequency Verdi operating at a wavelength of $\lambda = 532nm$ and impinging with an angle of $\sim 5°$ respect to the normal to the reflective SLM-display. The desired reduced irradiance profile is reconstructed by means of two relay lenses with focal lengths ranging between 63 and $500mm$ depending of the wanted lateral magnification. I adopted a lateral magnification of $0.1 - 0.2$ in this work, so that the pixel size of $9.5\mu m$ produces a resolution in the writing intensity of $\sim 1 \div 2\mu m$. A higher resolution could be achieved with the drawback of producing smaller structures. The direct writing method has the same advantages of the Fourier holography scheme and solves the problem of the small cured areas of the FHS. In comparison, the right positioning of the sample is much more easy to accomplish thanks to the large depth of field (several hundreds of microns at least) of the relay lenses that substitute the microscope objective of the FHS. Typically, the desired intensity pattern superimposed to the sample is monitored using a laser source operating at a control wavelength $\lambda_c = 633nm$, different with respect to the writing laser, in order to prevent undesired photo-polymerization of the sample. The monitoring system is coincident with the one used in the Fourier scheme: a microscope objective ($20\times$) and a CCD camera (Fig. 3.12). Taking into account the spectral dependence of the imaging parameters, the positioning is then properly corrected when operating with the writing wavelength. This method of "direct imaging" permits to obtain higher spatial resolution in writing the pattern ($< 1\mu m$) and a higher optical contrast (from $\sim 25 : 1$ to $\sim 50 : 1$), thanks to the

increasing of the visibility of the highly illuminated regions with respect to the dark regions of the irradiance distribution, that correspond, as for instance, to the bright fringes in a 1-D periodic profile like a Bragg grating.

Like for the previous scheme, also in this case the design of the optical setup has been studied firstly with the Geometric optics approximation and the ABCD matrices and then by applying the diffraction theory. The quality of the writing patterns is demonstrated by the structures that I realized and that are presented in the next sections.

3.1.5.1 Calculation of the Writing Intensity Profiles

Experimentally, the direct holograms presented a peculiar property that was confirmed by the theoretical calculations provided using my modified version of the AA algorithm and the diffractive description of the propagation process through the whole optical system. Considering the writing pattern near to the image plane of the CGH, I observed a periodic modulation along the z-direction, that is the optical axis of the system and the propagation direction of the beam diffracted and outgoing from the SLM-display. Monitoring the intensity profile produced by the direct holograms by moving the plane of the sample along the z-axis, in fact, the bright regions of the writing pattern periodically changed into the dark regions. In other words, the intensity distribution changed into its complementary or negative image so that a bright spot, as for instance, was transformed into a dark spot surrounded by a bright circle. This property was observed in the case of periodic intensity patterns as well as for quasiperiodic and aperiodic intensity profiles. The periodicity of the modulation along the propagation direction was different from the periodicity in the (x,y)-plane, that is why the homogeneity of the writing pattern along the thickness of the sample to be cured was not compromised. In fact, it was always larger then the thickness of the sample, therefore the thickness of the cell was chosen in relation to the particular pattern to write so that structure achievable could not be influenced from this effect. Furthermore, this circumstance was exploited to realize a three dimensional patterning even if the CGHs encoded a two-dimensional intensity distribution. I found that the period Λ_z of the modulation along the z-axis is related to the typical modulation length in the (x,y)-plane of the intensity profile. In the case of a 1-D periodic grating, in fact, it is related to the spacing Λ of the fringes, that I will indicate as Λ_x for clarity. Let us consider the case of a 1-D periodic and sinusoidal intensity profile, encoded by a direct CGH, with a period Λ_x. This may be calculated supposing the interference of two plane waves having propagation vectors $\mathbf{k}_1$ and $\mathbf{k}_2$, that is a two-beam holographic process. In this case, the grating vector, having a magnitude

$$K_x = |\mathbf{k}_1 - \mathbf{k}_2| = \frac{2\pi}{\Lambda_x}, \tag{3.12}$$

is related to the spacing Λ_x that results

$$\Lambda_x = \frac{\lambda}{2\sin(\theta/2)}, \tag{3.13}$$

where λ is the common wavelength of the beams and θ measures the separation angle between them, ad depicted in Fig. 2.16 of Sec. 3.1.6. If we add a third beam along the z-direction, so that the three beams are coplanar, then a periodic modulation Λ_z appears in that direction too, in accordance with the relation

$$\Lambda_z = \frac{\lambda}{\cos(\theta/2)}. \tag{3.14}$$

It easy to show, in fact, that the grating vector along the z-axis $\mathbf{K}_z$ is given by the difference of the propagation vector of the third beam with the vector $(1/2)\mathbf{K}_x = (\mathbf{k}_1 - \mathbf{k}_2)/2$, hence the period along z is larger. The overall effect of this three beam process is that there are planes along the z-direction in which the period of the grating results to be one half of the original grating spacing, that is equal to $(1/2)\Lambda_x$. This is actually what happens if the CGH addressed to the SLM encodes a 1-D periodic profile. In fact the CGH itself acts as a diffraction grating and produces a central undiffracted beam together with several lateral diffraction orders. Neglecting the contribution of the orders superior than the first[2], the intensity pattern experimentally achieved may be then described as the superposition of these three beams that produce an interferential modulation both in the x- and z-direction. Moreover, by blocking the central beam, the modulation along the z-axis disappears. Also this effect was experimentally confirmed. In Fig.3.13-(a) the theoretical intensity profiles produced by the coplanar three-beam interference are shown. In the calculation the amplitudes and phases of the three plane waves are supposed to be all equal. It is possible to see that along the propagation direction there is a modulation appearing as a shifting of the intensity fringes: for $z = \Lambda_z/2$ there is a π shift so that the bright fringes change into the dark fringes and viceversa; for $z = \Lambda_z$ the intensity profile coincides with that at $z = 0$. The most interesting aspect in shown for $z = \Lambda_z/4$, that is for a $\pi/2$ shift, at which position, in fact, the spacing of the fringes, hence the period of the grating, becomes one half of the original. In Fig.3.13-(b) the experimental grating produced is shown. The photos are taken under a polarizing microscope. It is evident that there is a complete correspondence with the theoretical calculations. This property may be therefore useful to realize particular structures and study their interesting, yet unknown, properties. This is what I actually did, as discussed in the next sections where the details of the gratings fabrication and their electro-optical characterization are also presented.

Let us now discuss what happens in the case of more complex structures, that are 2-D periodic and quasiperiodic intensity profiles. As described in the Sec. 2.5.4, the multiple-beam holography may used in general to realize 2-D structures both periodic and quasiperiodic. To design the intensity profiles needed to induce the proper dielectric modulation inside a photosensitive material it is possible to calculate the interference profile of a multiple-beam process exploiting the relations 2.58, 2.63 and 2.64. These equations describe the interference process from a general

[2]Because the higher orders possess a lower intensity with respect to the first order and, moreover, they cannot not be collected by the imaging system because the lenses have a too small diameter, even if it is of 2 inches.

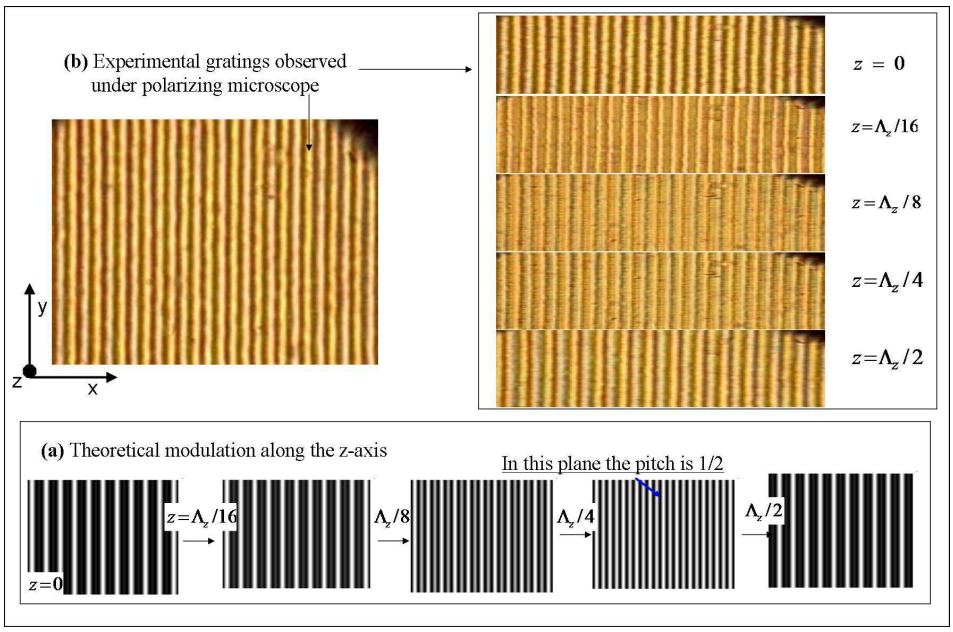

Figure 3.13: (a) Calculated intensity profiles produced by the interference of three coplanar beams at different position along the z-axis; (d) polarizing microscope images obtained changing the plane of focusing of the sample: a polymeric grating experimentally realized using a CGH encoding a 1-D periodic grating.

point of view, considering the case of an elliptical polarization of the N beams and also the possibility that the beams possess a different amplitude and global phase. Therefore, the interference pattern depends on many parameters ($6N+1$ in general). A useful simplification of the problem is offered by the equations 2.70 and 2.71 that describe the typical situation met in a multi-beam holographic experiment. The N beams in this case have the same linear polarization and the same amplitude and phase.

Let us consider a similar situation relaxing the hypothesis of the equal phases and considering an additional beam $(N+1)$ having a propagation vector $\mathbf{K}_z$ along the optical axis of the system, uniform amplitude A_0 and phase ϕ_0. This beam does not influence the rotational symmetry, so that the intensity profile keeps on holding an N-fold symmetry. The intensity profile becomes

$$I(\mathbf{r}) = A_0 \exp\left[i\mathbf{K}_z \cdot \mathbf{r} + i\phi_0\right] + \sum_{l,m=1}^{N} A_l^* A_m \exp\left[i\left(\mathbf{K}_l - \mathbf{K}_m\right) \cdot \mathbf{r} + i\left(\phi_l - \phi_m\right)\right], \tag{3.15}$$

that represents the intensity distribution given from the interference of N beams equally polarized, with initial phases ϕ_l, uniform amplitudes A_l ($l = 0,1,...,\ N$) and equally spaced around the azimuth so that each propagation vector $\mathbf{K}_m$ assumes the following expression (derived from the equation 2.58):

$$\mathbf{K}_m = \frac{2\pi n}{\lambda}[\cos(\frac{2\pi m}{N})\sin\theta, \sin(\frac{2\pi m}{N})\sin\theta, \cos\theta], \tag{3.16}$$

where n is the average refractive index of the photosensitive mixture and λ the common wavelength of the beams. Like for the case of three coplanar beams, that may be seen as a two-beam process with an additional beam, also in this case the beam along the z-direction has the only effect of producing a periodic modulation along its propagation direction, even though the resulting N-beam intensity profile is quasiperiodic rather than periodic. I calculated the intensity profiles needed to induce the formation of the quasiperiodic structures into the LC-polymer mixture using the equation 3.15 supposing $A_0 = 0$. To compare the experimental results with the theoretical profiles and to determine the period of the z-modulation, instead, I considered the general case of A_0
$neq0$ but with a phase $\phi_0 = 0$. In fact, this term, experimentally, may be due to the undiffracted light (the zero diffraction order of the CGH) but there is no real multiple-beam interference so that the actual diffraction orders may be considered in practice having all the same phase. The case of a periodic 2-D profile is clearly included in the general relation 3.15 as well as the two-beam and three-beam interferences. In Fig. 3.14 the quasiperiodic intensity profiles (IPs) calculated with the aforementioned relation are shown for a 8-, 9-, 10-, 12-beam interference. Figure 3.14-(a) and (b) show two irradiance profiles possessing both an 8-fold rotational symmetry although the calculated interference profiles have been obtained for different values of the initial phases ϕ_i of the interfering beams. In particular, $\phi_i = 0$, with $i = 1,...,\ 8$ in (a), whereas $\phi_2 = \phi_4 = \phi_6 = \phi_8 = \pi/2$, $\phi_3 = \phi_7 = \pi$ in (b).

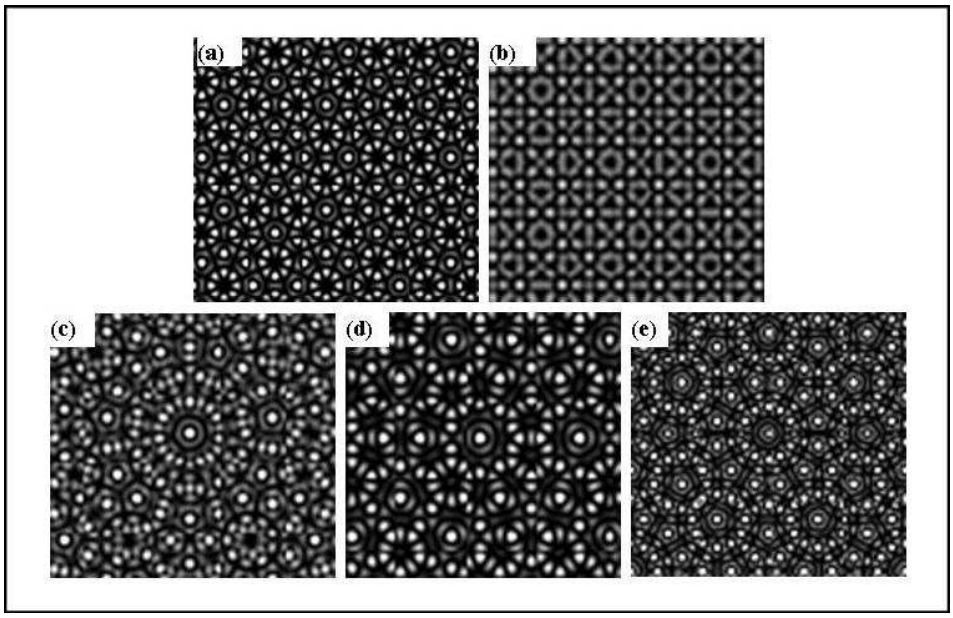

Figure 3.14: (a) Calculated quasiperiodic irradiance profile (IP) with 8-fold rotational symmetry obtained from phase values $\phi_i = 0$, for $i = 1,..., 8$, say 8-fold(A) pattern; (b) calculated 8-fold IP from phase values $\phi_1 = \phi_5 = 0$, $\phi_2 = \phi_4 = \phi_6 = \phi_8 = \pi/2$, $\phi_3 = \phi_7 = \pi$, say 8-fold(B) pattern. (c)-(e) Calculated IPs from 9-, 10-, 12-beam interference, respectively.

Let us indicate the first as 8-fold(A) pattern and the latter as 8-fold(B) pattern. These quasiperiodic profiles reveal an important advantage of the CGH-based technique with respect to the multiple-beam holography, in fact the accurate control of the optical phases of the beams in a multi-beam process is very difficult to experimentally achieve, and, consequently, the reproducibility of the structure may be compromised. These two structures are particular interesting as I will discuss hereinafter in the thesis. During this work, in fact, I realized tens and tens of structures changing the parameters of the interference relation and I realized also aperiodic structures not achievable as an interference process. This thanks to the great versatility of the holographic technique that I used. Among the structures that I calculated and fabricated, the 8-fold(A) and 8-fold(B) patterns will be useful to describe important aspects of the SLM-CGH technique. Figures from 3.14-(c) to (e) show the calculated IPs possessing a 9-, 10- and 12-fold rotational symmetry, respectively, obtained supposing no phase retardation between the interfering beams.

3.1.5.2 Aperiodic Patterning: the Thue-Morse Structure

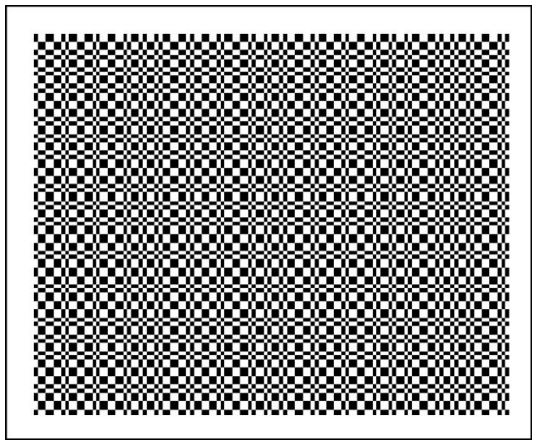

Figure 3.15: Two-dimensional Thue-Morse structure.

In Fig. 3.15 an aperiodic pattern is depicted representing the so called two-dimensional Thue-Morse structure. The Thue-Morse structure is an example of aperiodic pattern [Macià 2006], defined by recursive sequences, that cannot be obtained by interference of coherent beams. One-dimensional Thue-Morse gratings are known to exhibit PGB with interesting omnidirectional reflectance [Kolar 1994]. 2-D Thue-Morse gratings are defined mathematically by recursive procedure (see equation 3.17 below). Very recently, theoretical studies have shown the presence of PBG in a two-dimensional Thue-Morse structure [Moretti 2007]. We reported the first experimental realization of a photonic structure exhibiting a two-dimensional Thue-Morse arrangement [Zito 2008]. As we will see in the next sections, in fact,

the CGH technique permitted the realization of this kind of structure together with other complex patterns, possessing a rotational symmetry as high as 23-fold, by encoding the desired information into a CGH and using hence a single-beam technique. This demonstrates the great potential of our technique. In the one-dimensional case, a binary Thue-Morse sequence is constructed using the following rule: given an arbitrary sequence of two symbols, $A = 0$ and $B = 1$, say, a new sequence is formed by replacing each occurrence of A with the pair (A, B) and any occurrence of B with the pair (B, A) [Macià 2006]. The one-dimensional quasi-periodic Thue-Morse grating is formed starting from the single element A. The one-dimensional Thue-Morse grating is generalized to the two-dimensional case by the recursive rule defined by the following relation

$$M_{n+1} = \begin{pmatrix} I_n - M_n & M_n \\ M_n & I_n - M_n \end{pmatrix}, \tag{3.17}$$

in which

$$I_n = \begin{pmatrix} 1_{1,1} & \cdots & 1_{1,k} \\ \vdots & \ddots & \vdots \\ 1_{k,1} & \cdots & 1_{k,k} \end{pmatrix} \text{,with } k = 2^n, \tag{3.18}$$

where $I_{n,n}$ is a $2^n \times 2^n$ matrix in which each element is equal to one, and the initial matrix, for $n = 1$, is $M_1 = (0)$. It is easily verified, in fact, that any row and any column of the $2^{(n+1)} \times 2^{(n+1)}$ symmetric matrix M_{n+1} is a Thue-Morse sequence of order $n + 1$ generated from the first element of the row or column itself. The initial condition of the recurrence, defined by the starting matrix (a single element is a particular case), determines the symmetry and the properties of the 2D-Thue-Morse pattern affecting the optical properties of the resulting dielectric structure. In fact, given a binary square matrix of arbitrary size as the initial condition of equation 3.17, the resulting matrix of the iteration is a Thue-Morse 2D-pattern in which the unit cell corresponds to the matrix given in the initial condition. We expect that changing the unit cell from a scalar to an arbitrary square matrix would imply a modification of the Thue-Morse superstructure and, hence, of the photonic band gap properties of the quasicrystal. Typically ten or more iterations of equation 3.17 are needed in order to achieve the matrix size saturating the resolution of our SLM.

3.1.6 The Photosensitive Mixture and the Optical Curing

The gratings are obtained by curing, at room temperature T_o, a pre-polymer/LC photosensitive mixture, aiming to realize H-PDLC-like dielectric arrangements. The solution that gave the best results in terms of phase separation and optical contrast, reported in Tab.3.1, was made of the monomer *dipentaerythrol-hydroxyl-penta-acrylate* (DPHPA) (60.0% w/w), the cross-linking stabilizer monomer *N-vinylpyrrolidinone* (NVP) (9.2% w/w), the liquid crystal *BL038* by Merck (30.0% w/w), and a mixture of the photoinitiator *Rose Bengal* (RB) (0.3% w/w) and the coinitiator *N-phenylglycine* (NPG) (0.5% w/w). In sections and , the role of each

component is clarified and the anisotropic photopolymerization process produced by the optical curing of the visible irradiance pattern is discussed in details. During the process the thermal control has not been used because I found good results at the room temperature thanks to the viscoelastic properties of the LC component adopted, that was in nematic phase for $T = T_o$. The polymer has a refractive index

Component	**Concentration** (w/w)
Monomer *DPHPA*	60%
Liquid crystal *BL038*	30%
Photoinitiator *RB*	0.3%
Coinititor *NPG*	0.5%
Reactive diluent *NVP*	9.2%

Table 3.1: Component concentrations that gave the best phase separation and optical contrast results in the sample preparation of the photosensitive mixture to be optically cured.

$n_p = 1.530$, whereas the LC $BL038$ has an ordinary refractive index $n_o = 1.527$ and an extraordinary refractive index $n_e = 1.799$. The average refractive index was estimated to be $n \sim 1.57$ as described in Sec. 3.1.6. Although the refractive index contrast achievable with such a mixture, usually, is $\Delta n \sim 0.2 \div 0.3$, the liquid crystal content can be removed in the case of not switchable structures to increase the index difference up to ~ 0.5. Other mixtures can be used in order to increase the amplitude of the dielectric modulation, but they will not take into account on this work. The thickness of the sample cell varied from about 5 to $30\mu m$, whereas the cured area has a linear dimension ranging from ~ 4 to $20mm$ in the Direct Writing approach, depending on the magnification factor of the imaging system. Instead, the linear dimension of the cured area depends of the magnification factor of the microscope objective in the Fourier holography scheme where it is typically $\sim 1mm$.

The parameters of the optical curing process are essentially matter of experience. The dynamics of formation of the 1-D diffraction gratings in the case of the H-PDLCs is monitored through an additional laser source, a He-Ne laser at $632nm$, as previously described. In the case of 1-D and 2-D aperiodic structures it is difficult to control the formation of the dielectric arrangement with this technique. The phase separation between the liquid crystal component and the polymer depends of the typical spacing of the structure and thus the curing parameters, that are the power of the light incident on the sample and the exposure time, must be chosen in relation to the particular experimental situation. The intensity of the writing pattern was usually in the range of $1 \div 20mW/cm^2$ at the sample position, that is considering the attenuation and losses due to the optical elements, including the diffraction efficiency of the CGH addressed to the SLM. The exposure time was typically ranging between $30s$ and $300s$ depending on the writing power.

3.2 Experimental Results

In the next sections, the most important examples of the experimental structures that have been produced in this thesis by single-beam spatial modulation based on computer-generated holograms are finally described. If not differently specified, the presented structures have been realized with the direct writing method.

3.2.1 1-D Diffraction Gratings

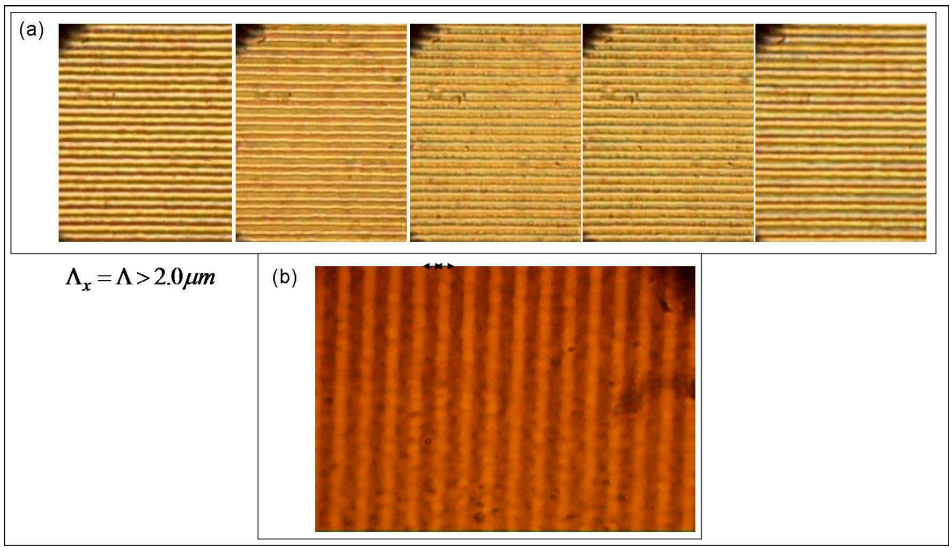

Figure 3.16: (a) Several examples of experimental gratings: the fringe spacing of the intensity pattern is modulated to produce a different grating period Λ; (b) equal polymer- and LC-fringe spacing (double arrow): reduced shrinkage.

In Fig. 3.17-(a) an example of a one-dimensional diffraction grating produced with a CGH encoding a square-wave intensity pattern is shown. The undiffracted central beam may attenuated or blocked in order to obtain a 1-D modulation only in the (x,y)-plane of the sample. As described in the previous section, this effect can be exploited to produce a periodic modulation along the propagation direction and to produce higher resolution gratings, with a period equal to one half of the fringe spacing expected in the case of a two-beam interference. At the present, the smaller grating pitches reached in this work are of the order of $\sim 1.2\mu m$ due to the limited resolution of the SLM-display and the limited numerical aperture of the adopted relay lenses. Thanks to the possibility of a fine tuning of the writing pattern by changing the CGH real-time or changing the relative distance between the relay lenses (Fig. 3.12), the grating pitch may be changed with high precision ($\sim 100nm$) in order to satisfy the experimental requirements (see Fig. 3.16a). Moreover, the shrinkage of the polymer stripes affecting the homogeneity of the grating's period may be reduced by imposing different values to the spacing of the bright and dark

fringes, although, at the present, only for grating's period not smaller than $2.0\mu m$ (see Fig. 3.16b). The asymmetric period (with a bright fringe larger with respect to the dark one) compensates the shrinkage of the polymer-rich region corresponding to the bright fringe of the intensity pattern. The reproducibility of the structures

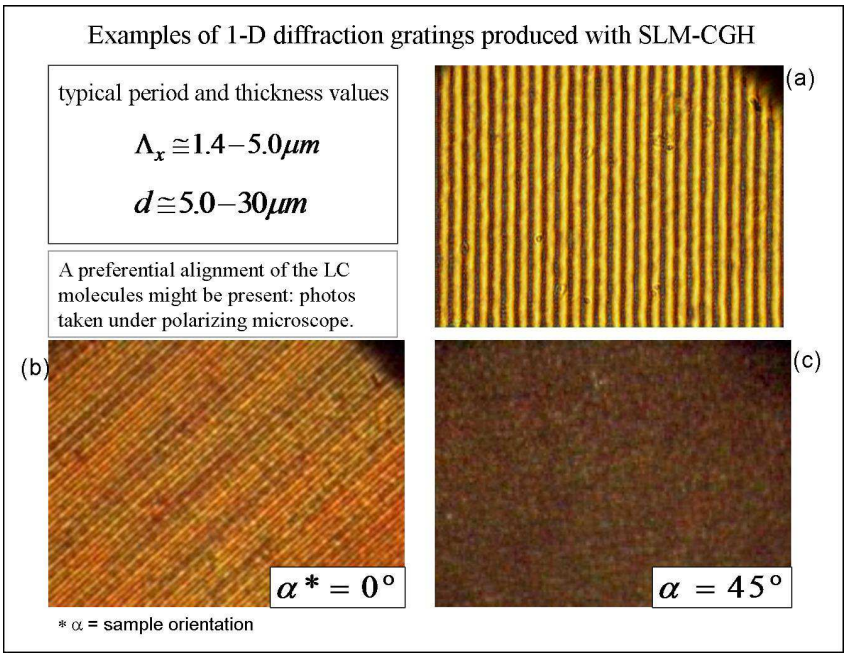

Figure 3.17: (a) Example of the one-dimensional diffraction grating achievable with the SLM-CGH technique; (b)-(c) images of a grating under a polarizing microscope for two different orientations of the sample with respect to the axis of the analyzer.

recorded into the LC-polymer composites is one of the great advantages of the SLM-CGH technique because this fabrication method is not affected from the instability of the phase coherence typical of the interference techniques. In Fig. 3.17-(b) and (c) the images of a grating under a polarizing microscope are shown for different orientations of the sample with respect to the axis of the analyzer. The LC-rich fringes appear bright because the birefringence of the LC-molecules changes the polarization of the linearly polarized light that travels through the liquid crystal domain, therefore light is not extinguished by passing through the analyzer. The homogeneous polymer stripes, instead, appear completely dark. This circumstance reveals a good phase separation between the liquid crystal and polymer in the grating. Moreover, by rotating the sample, the LC fringes completely disappear (Fig. 3.17c) attesting a preferential alignment of the LC-molecules with the molecular director along the direction normal to polymer fringe. This morphology is typical of the POLICRYPS grating as discussed in Sec. 2.3.4. Later on we will see other evidences that bring us to believe that the gratings achievable with the SLM-CGH possess an intermediate behavior between POLICRYPS and H-PDLC gratings.

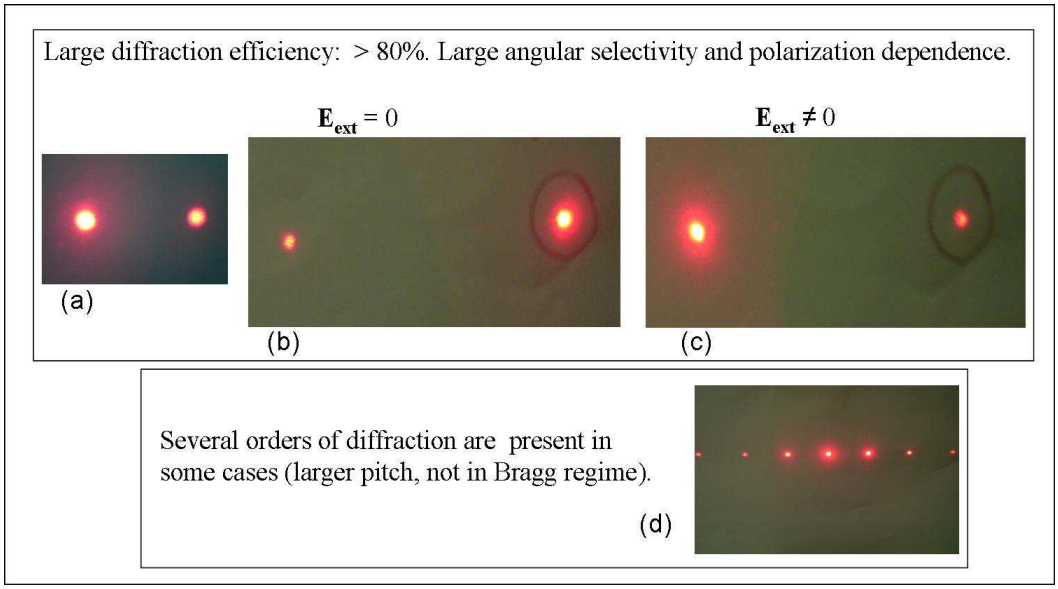

Figure 3.18: (a) Typical diffraction pattern produced by our transmission grating in the Bragg regime; (b)-(c) the intensities of the zero and first diffraction orders are modulated by applying an external electric field; (d) the diffraction pattern produced by our grating not in the Bragg regime.

As discussed in Sec. 2.2, the diffraction regime of the gratings depends on many aspects among which it is possible to identify several important parameters to design and classify the holographic gratings. According to those, the gratings here produced are expected to be volume phase gratings in Bragg regime and to work in transmission (see Sec. 2.2.8 and 2.2.4 for details). Although, usually, the experimental structures confirmed the expected behavior, I found situations in which it has been difficult to establish the diffraction regime. Further research is necessary to clarify what happens in these cases. In Fig. 3.18-(a) the typical diffraction pattern produced by a transmission grating in the Bragg regime is shown, in which the zero and the first (+1) diffraction orders are both visible when the illuminating beam, a He-Ne laser at $632.8nm$, impinges perpendicularly to the surface of the sample. In Fig. 3.18-(b) and (c) the intensities of the zero and first diffraction orders are modulated by applying an external electric field $\mathbf{E}_{ext}$ at the conductive plates of the sample (coated with indium tin oxide ITO). As schematically depicted in Fig. **??**, when the state is on ($\mathbf{E}_{ext} = 0$) the most part of the light is diffracted into the first order if the normal $\hat{n}$ to the sample's surface is oriented at the Bragg angle θ_B with respect to the propagation vector of the incident beam ($K\hat{z}$), that is $\hat{z} \cdot \hat{n} = \cos\theta_B$, as shown in Fig. 3.18-(b); when the state is off ($\mathbf{E}_{ext} \neq 0$) the most part of the light is transmitted into the zero order in the same condition of Bragg orientation, as shown in Fig. 3.18-(c). Consequently, the grating becomes an active device acting as an optical switch that can be used in optoelectronic circuital

elements. The application of an electric field (typically a square wave profile with a modulation frequency of $1KHz$) modulates the diffraction efficiency of the grating by reorienting the birefringent liquid crystals molecules so that the refractive index contrast vanishes when all the molecules are aligned with the external field. The diffraction efficiency depends on the optical contrast achieved in the grating, related to the dielectric contrast dependent on the amount of phase separation established in the grating. The dependence of the diffraction efficiency η on $\mathbf{E}_{ext}$ is affected by many parameters, above all the presence of droplet domains of LC-molecules like in the H-PDLC or not like in the POLICRYPS. In Fig. 3.18-(d) the diffraction pattern produced by a different grating not in the Bragg regime is represented: beyond the central undiffracted light (0^{th} order) and the first diffraction orders (± 1), many other higher orders are present.

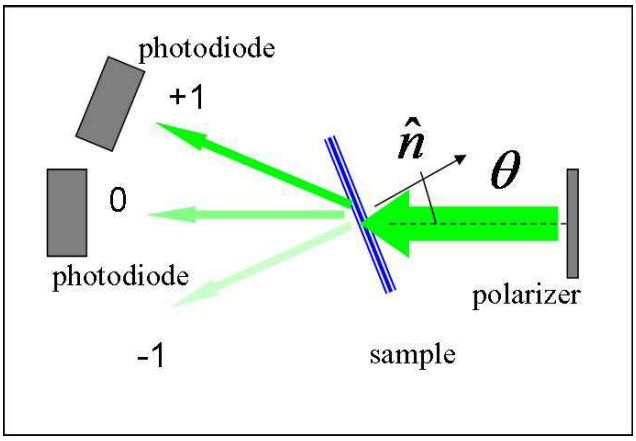

Figure 3.19: Schematic representation of the experimental apparatus for the measurement of the diffraction efficiency $\eta(\theta)$.

In Fig. 3.19 the schematic representation of the experimental apparatus for the measurement of the diffraction efficiency $\eta(\theta)$ as a function of the angle θ between $\hat{n}$ and $K\hat{z}$ is depicted. Usually, the characterization has been made for $\lambda_c = 632.8nm$ with a He-Ne laser, both for incident s- and p-polarization. The diffracted and transmitted light is collected with a photodiode simultaneously. The sample is positioned on a motorized rotational stage controlled with the National Instruments software Labview 7.0 that is interfaced with the detectors. In fact, the incident light is modulated with a chopper and the modulation frequency is sent to a Lock-in Amplifier together with the output signals from the photodiodes to increase the sensitivity of the light detection. The coincidence of the measurements is provided via computer using Labview. The measurement at each angle is repeated several times and then averaged before the subsequent step. The sample is also controlled in temperature. The measurements have been made at $T = 25°C$. The same apparatus has been used for the characterization of the diffraction efficiency at the Bragg angle, that is $\eta(\theta_B)$, as a function of the applied external electric field.

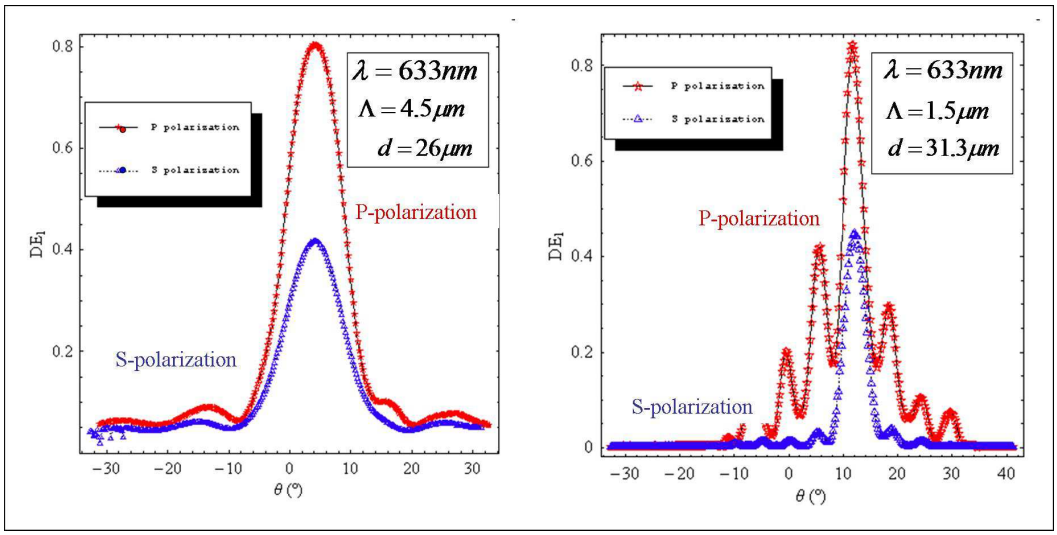

Figure 3.20: Experimental observation of two typical curves of diffraction efficiency as a function of the incidence angle.

Two typical curves of the angular dependence of the diffraction efficiency experimentally observed are shown in Fig. 3.20, both for perpendicular and parallel polarization of the incident beam. The measured diffraction efficiencies were larger then 80% in many cases, revealing a large optical contrast induced into the grating formation. The curves agree with the theoretical Bragg regime discussed in Sec. 2.2. In the insets of each graph the experimental parameters of incident wavelength λ and thickness d of the sample are shown together with the measured grating pitch Λ. For smaller Λ (curve on the right) the spectral selectivity is very large (inversely proportional to the full width half maximum value). The efficiency measured for p-polarization is clearly different with respect to the case of s-polarization, the latter being lower at the Bragg peak of about the 40%. This behavior has not been observed in a H-PDLC nor in a POLICRYPS grating. For the H-PDLC only a very little dependence on the polarization has been observed experimentally, whereas for the POLICRYPS the s-polarization efficiency should be nearly zero. This circumstance is another evidence that the gratings achieved are not H-PDLC nor POLICRYPS but they have an intermediate behavior that reveals the advantage of the high diffraction efficiency of POLICRYPS and the advantage of a polarization dependence but without the drawback of a vanishing efficiency for the s-polarization. This is s very surprising result in our opinion because there has not been a thermal control during the curing process, that is one of essential aspect of the POLICRYPS quality (see 2.3.4). However, one of the drawback presented by our gratings consists in the higher voltages required to induce a modulation of the efficiency by applying an external electric field with respect to the values usually required in the case of PLICRYPS gratings ($\sim 4V/\mu m$). The property of high switching voltage is typical, in fact, of the droplet gratings ($\sim 10V/\mu m$). Moreover, the maximum variation of

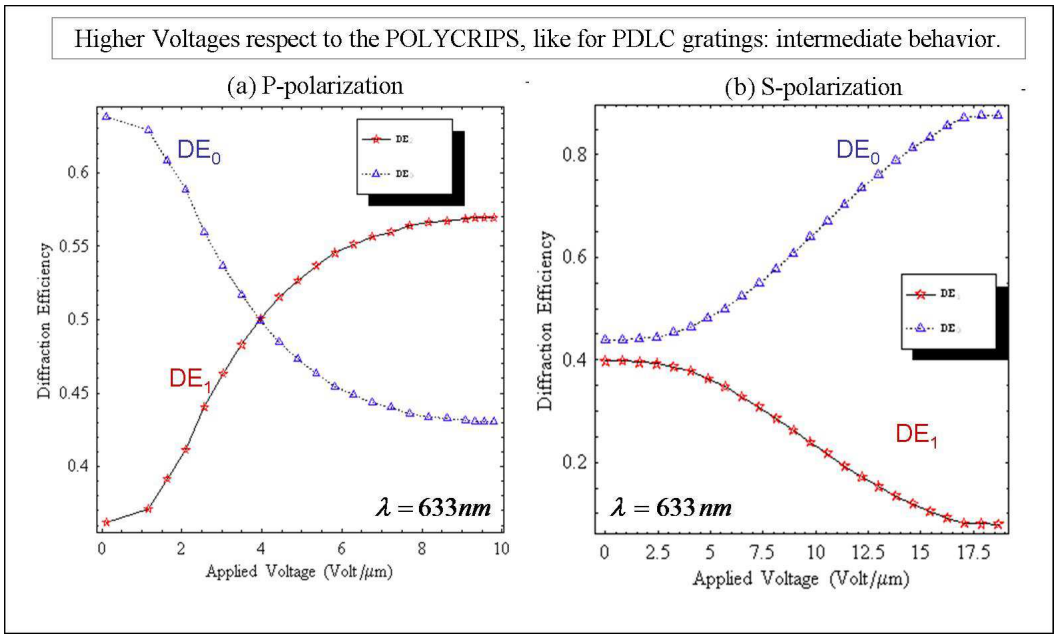

Figure 3.21: Diffraction efficiency as a function of the applied external electric field for p-polarization (a) and s-polarization (b) of the incident beam.

the diffraction efficiency as a function of the voltage is similar to the PDLC case. This behavior is evident in Fig. 3.21: the diffraction efficiency depends again on the polarization state of the incident beam and with a typical variation of about 20% for p-polarization (a) and $\sim 40\%$ for s-polarization (b), while the switching voltage is about $5V/\mu m$ for p-polarization and $\sim 10V/\mu m$ for s-polarization. This difference may be due to the presence of optically anisotropic liquid crystal domains with a molecular orientation, only averagely, along a preferential direction, that therefore, it gives rise to a polarization dependent behavior. Therefore, the gratings manifest an intermediate behavior in relation to the switching voltage too.

3.2.2 Diffraction Gratings with a Periodic Modulation along the z-axis

Figure 3.22 refers to the case of a grating possessing a periodic modulation along the z-direction. The grating morphology is shown in Fig 3.13. In Fig. 3.22-(a), the presence of the modulated structure is revealed by the existence of two completely different angular diffraction efficiencies for p-polarization and s-polarization. For p-polarization the eventual pitch Λ associated to the Bragg peak (it is not possible to actually establish if the grating is or not in the Bragg regime) is about one half of the pitch for s-polarization (in this case the Bragg regime is evident). In the first case, the presence of multiple diffraction peaks may be due to the fact that the grating is not in the Bragg regime. Another possibility if that the multiple peaks may be

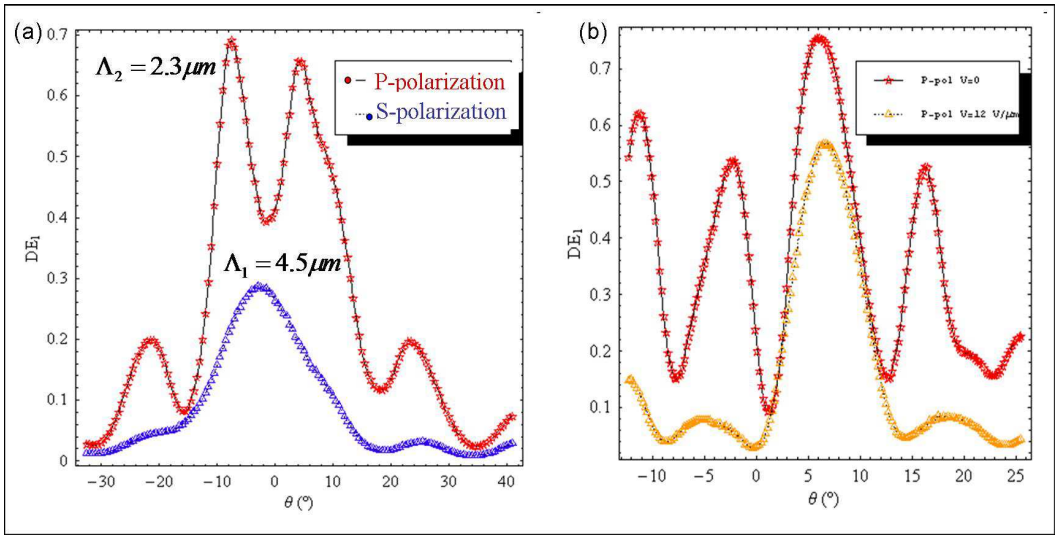

Figure 3.22: (a) Diffraction efficiencies for p-polarization and s-polarization for a periodic grating possessing a periodic modulation along the z-direction too; (c) z-modulated grating: variation of the p-polarization angular efficiency for two values of the external voltage.

related to the singular morphology of this kind of structure in which subsequent shifted gratings are stacked together and where the period Λ_x becomes one half of the original value at a certain depth z, as discussed in Sec. 3.1.5.1. Why different polarization states should experience a different behavior is not clear. Therefore, the understanding of the actual behavior of this kind of structure necessitates further research. However, this z-modulated grating represents a very interesting result in our opinion, because it may be used for particular electro-optical applications thanks to its characteristic polarization dependence and to the possibility to electrically modify its efficiency. In fact, by applying an external field, the angular efficiency for p-polarization may be varied, as shown in Fig. 3.22-(b) (here the p-polarization curve is quite different with respect to the previous one because the sample, although possessing the same morphology, is different[3]).

3.2.3 2-D Periodic Structures

Among the many one-dimensional and two-dimensional gratings that I realized in this work, two examples of 2-D structures are shown in Fig. 3.23. In the upper and bottom parts of the figure, the calculated intensity profiles (a), the experimental realized patterns (b) and the experimental diffraction patterns (c) produced by the structure are shown. The intensity profiles are calculated from the two-beam

[3]This measurement was performed in a second moment on another grating because the first sample unfortunately was used for a scanning electron microscopy analysis before measuring its voltage dependence.

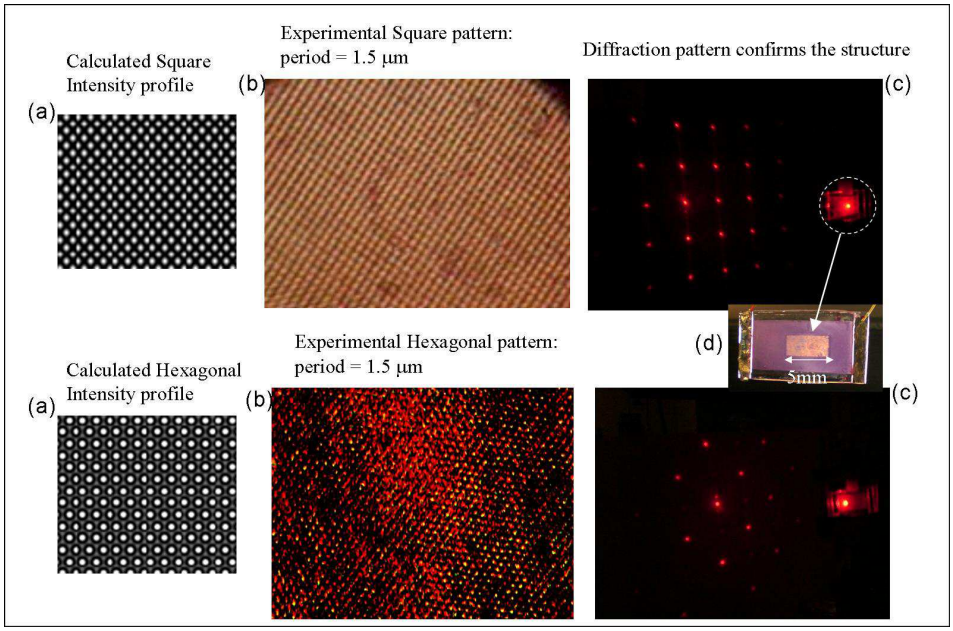

Figure 3.23: (upper part) Calculated intensity profile (a), experimental realized pattern (b) and the experimentally observed diffraction pattern (c) for a (2-D) square structure; (bottom part) calculated intensity profile (a), experimental realized pattern (b) and the experimentally observed diffraction pattern (c) for a (2-D) hexagonal structure; (d) typical sample produced starting from an initial homogeneous photosensitive mixture: the written area, with a size $\sim (2.5mm \times 5.0mm)$, becomes transparent after the optical curing.

interference relation by changing opportunely the parameters of the beams in order to produce the desired unit cell of the structure, as discussed in Sec. 2.5.4. The upper pattern manifests a square unit cell (rectangular in general), whereas the bottom pattern possesses a hexagonal (or triangular) unit cell. The far field diffraction pattern produced by these two structures confirms the expected symmetry and geometry, as shown in Figs. 3.23-(c). The hexagonal and square structures are of particular interest for photonic applications because they possess a PBG even for low dielectric contrast, therefore it should be possible to realize a PhC with soft materials like polymer and liquid crystals in which typical values of the difference Δn between their refractive index is of the order of 0.2. I will discuss this problem more in detail in the section regarding the FDTD simulations and the PBG properties of the realized structures. The structures realized in this work are made of polymer and liquid crystal mixtures in which the LC-component usually is embedded into the polymeric matrix realizing with a particular morphology the desired pattern. To reveal the achieved arrangement into such kind of patterns by Scanning Electron Microscopy, as usually may be done in the case of structures obtained by patterning hard materials, is a very difficult task, as discussed also by Gorkhali [Gorkhali 2006]. It the case of LC-polymer composites, the LC-component must be eliminated with a suitable procedure to permit the scanning of the surface of the structures. This may be done when a large phase separation occurs, as in the case of 1-D gratings. The diffraction pattern, however, is a reasonable evidence of the presence of a phase modulation into these kind of structures. In Fig. 3.24 several SEM images[4] of two samples that I realized are shown. In the upper part of the figure, the top view images of hexagonal (a) and rectangular (b) structures are presented. The side view of the same structures is depicted in the bottom part of Fig. 3.24, indicated as (a) and (b) for hexagonal and rectangular, respectively. The formation of a the desired pattern is evident although not very striking.

3.2.3.1 3-D Periodic Structures

If a CGH encoding a one-dimensional periodic modulation like a Bragg grating produces a periodic modulation along the z-direction, that is the optical axis of the experimental setup, then starting from a CGH encoding a two-dimensional periodic profile in the (x,y)-plane of the writing pattern it is possible to exploit the interference of the lateral diffraction orders produced by the SLM to induce a periodic z-modulation also in this case. The result is a stack of 2-D gratings that are shifted along the thickness (z-axis) of the sample, so that a three-dimensional structure may be achieved with a single step process. The top view of this structure is shown in the polarizing microscope image of Fig. 3.25-(a), whereas its experimental diffraction pattern (produced with a laser beam operating at $\lambda = 532nm$) is represented in the inset (b) of the same figure. However, with this approach the period along the third dimension is different, larger precisely, with respect to the period along

[4]The SEM images shown in Fig. 3.24 have been acquired in the laboratories of the University "Politecnica delle Marche" of Ancona in collaboration with the group of Pr. F. Simoni.

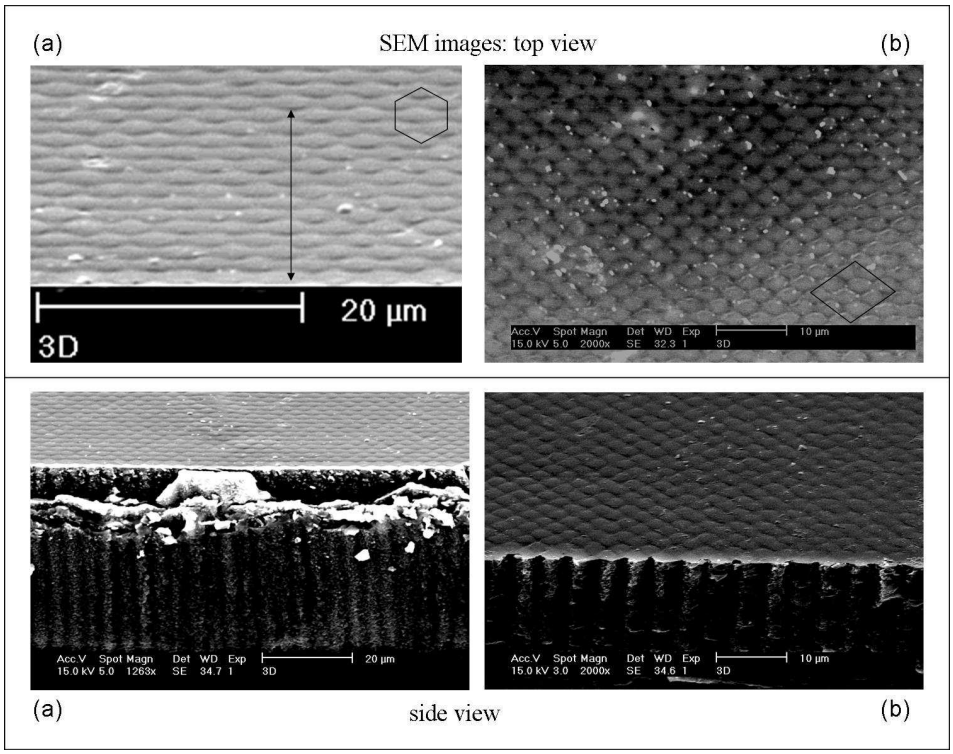

Figure 3.24: (upper part) SEM top view images of hexagonal (a) and rectangular (b) structures; (bottom part) SEM side view images of hexagonal (a) and rectangular (b) structures.

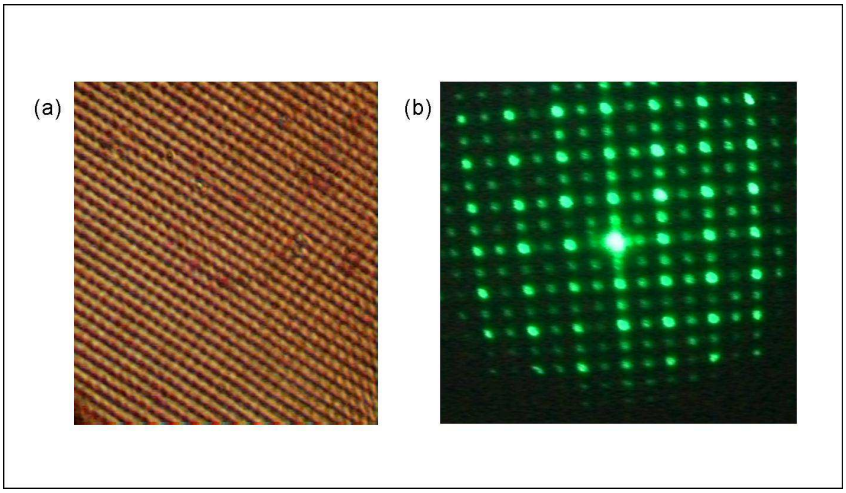

Figure 3.25: (a) Top view of a polarizing microscope image of a 3-D square periodic structure; (b) experimental diffraction pattern produced by the structure in (a).

the transverse plane. The fabrication of a 3-D structure for more reliable applications requires the implementation of more complex CGHs, by projecting, as for instance, a three-dimensional array of light spots inducing the polymerization of the sample in according to the 3-D geometry of the spots array. This may be actually done with a CGH (see [Grier 2003] for details), although this technique has not been exploited yet for photo-polymerization of liquid crystal and polymer composites. At the present, I'm working to develop this 3-D optical curing system, but unfortunately I have not yet obtained satisfying results.

3.2.4 2-D Quasiperiodic Structures

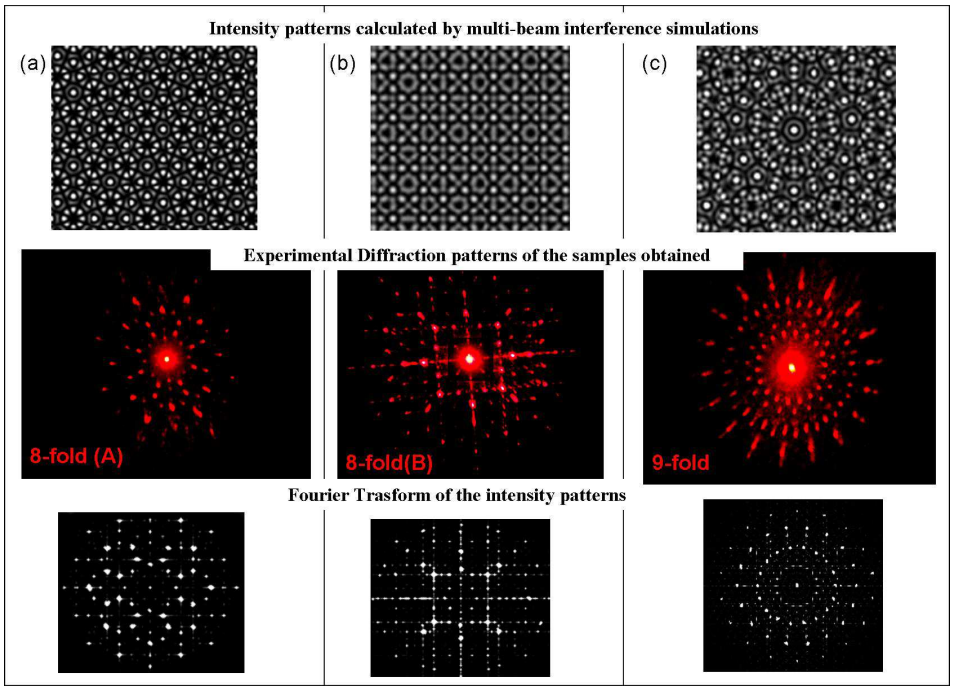

Figure 3.26: Quasiperiodic structure 8-fold(A) (a), quasiperiodic structure 8-fold(B) (b), quasicrystal structure with 9-fold symmetry (c): (first row) calculated irradiance profile (IP); (second row) observed diffraction pattern (DP); (third row) 2D Fourier transform (FT) of the irradiance profile.

In Fig. 3.26 three examples of the quasiperiodic structures produced with the SLM-CGH technique, using the direct writing approach, are shown. The figure is divided into three insets, indicated with the symbols (a), (b) and (c) that are related to different rotational symmetries or tiling geometries of the structures. In detail, insets (a) and (b) refer, respectively, to the quasiperiodic 8-fold(A) and 8-fold(B) quasicrystals, previously defined (3.1.5.1) and shown in Fig. 3.14-(a) and -(b), respectively. Inset (c) shows a pattern possessing a 9-fold rotational symmetry. Each inset of the figure consists of three rows. In the first row, the Intensity Profiles (IPs),

calculated supposing a multiple-beam interference as discussed in Sec. 3.1.5.1, are depicted, where in the grey scale the white regions correspond to the constructive interference regions and viceversa. The IPs are sent to our SLM and then imaged at the sample position. In the second row, we have the experimental Diffraction Pattern (DP) produced by the written structure. Finally in the third row, the calculated 2D Fourier Transform (FT) of the related IP is represents. The FT pattern is calculated with a FFT algorithm in order to compare the theoretical diffraction pattern with the experimental result. Examples of quasiperiodic structures achievable varying the initial phases of the interfering beams in the numerical calculation of the irradiance profile are presented in Fig. 3.26-(a) and (b) for a structure with 8-fold rotational symmetry. In the inset (a) all the beams possess the same initial phase, where in the inset (b), instead, the initial phases of the eight beams are periodically shifted of $\pi/2$. Analogously, figures 3.27-(a), -(b) and -(c) refer to 2-D

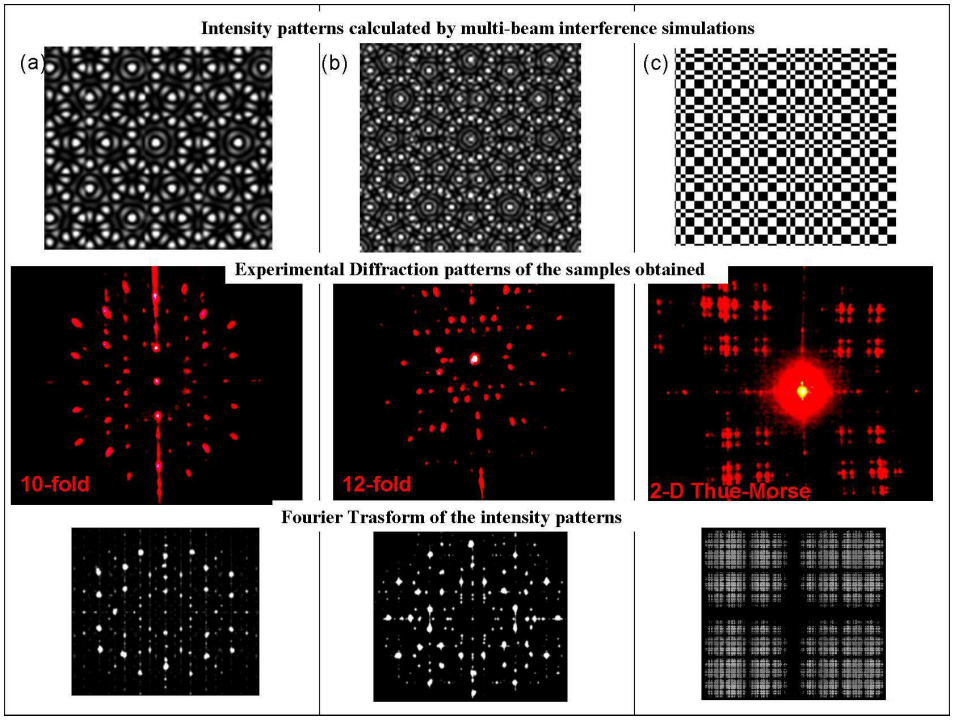

Figure 3.27: Quasiperiodic structure with 10-fold symmetry (a), quasicrystal with 12-fold symmetry (b), 2D aperiodic Thue-Morse structure (c): (first row) calculated irradiance profile (IP); (second row) observed diffraction pattern (DP); (third row) 2D Fourier transform (FT) of the irradiance profile.

quasiperiodic structures having 10- and 12-fold rotational symmetry and to the aperiodic 2-D Thue-Morse pattern in this order. Figures 3.28-(a) and -(b) refer, instead, to quasiperiodic structures having 17- and 23-fold rotational symmetry in this order. In each inset the calculated IP, the observed DP and the theoretical DP, calculated as Fourier Transform of the irradiance profile, are shown. The similarity between the

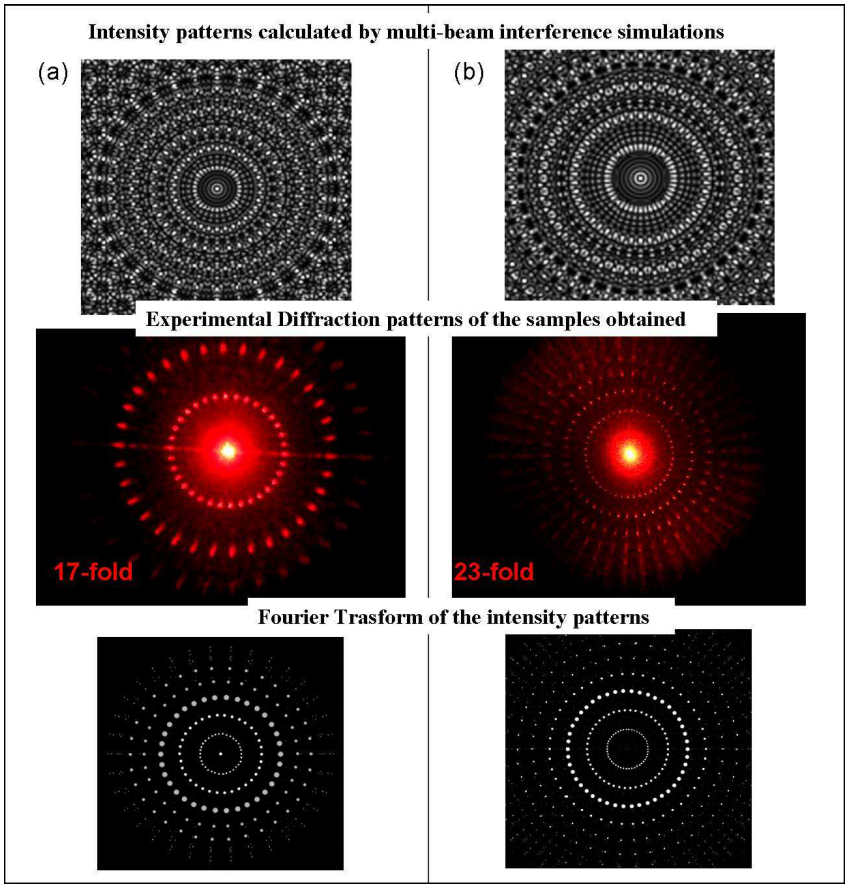

Figure 3.28: Quasiperiodic structure with 17-fold symmetry (a), quasicrystal with 23-fold symmetry (b): (first row) calculated irradiance profile (IP); (second row) observed diffraction pattern (DP); (third row) 2D Fourier transform (FT) of the irradiance profile.

positions and cone angle of the spots in the calculated Fourier transform FT and the observed diffraction pattern DP demonstrates the good quality of the quasicrystals written with the SLM-CGH technique. These structures are two-dimensional phase gratings in which the modulation profile of the average refractive index is not easily accessible with the scanning electron microscopy. Nevertheless, the observed optical diffraction patterns doubtless substantiate the presence of the index profile. The diffraction spots in first and higher orders show the expected N-fold symmetry and have N points for even symmetry and $2N$ points for odd symmetry, as described in Sec. 2.5.4. The magnitudes of the basic reciprocal vectors in the diffraction patterns are related to sensible lengths of the crystal structures, such as a tile side, because they are related to the fundamental reciprocal vectors of the quasicrystal. In this way I estimated the size d of the self-similarity cell (the "unit cell") to be in the range between 4.8 and 8.6μm, increasing with the order of the symmetry, as reported in Tab.3.2. It is worth noticing that, even if the typical length of the obtained struc-

N-**fold symmetry**	8-(A)	8-(B)	9	10	12	17	23	Thue-Morse
"unit cell" d (μm)	4.8	5.3	5.7	5.8	5.8	6.1	8.6	4.6

Table 3.2: Experimental self-similar "unit cell" d measured in quasiperiodic patterns realized with different rotational symmetries and in a 2D aperiodic Thue-Morse structure.

tures was in the range $(5-10)\mu m$, the typical separation between equal dielectric regions in the fine structure of the self-similarity cell was in the range of $(1-2\mu m)$. In fact, the 1-D Bragg grating and 2-D periodic square and triangular lattices that I realized had a pitch of about $1.5\mu m$. The scale length of the realized structures depends on the lateral magnification of the relay lenses of the DWM, which also affects the extension of the writing area, as long as the spatial resolution is far from the diffraction limit. The ultimate limit in the achievable resolution depends on the SLM pixel size and on the wavelength of the writing light. Using UV light and state-of-the-art SLM pixel size [Apter 2007], the limit in the spatial resolution could be improved by a factor of $3-4$. Since now however, the scalability of the optical properties permits to use the quasiperiodic structures that I realized to study their interesting yet unknown optical behavior. The importance of these quasicrystals relies on the ability to produce with a single beam technique quasiperiodic Penrose-tiled structures with unprecedented rotational symmetry up to 17- and 23-fold and two-dimensional Thue-Morse structures too. To realize a 23-fold quasicrystal with the usual multi-beam holographic lithography, 23 interfering laser beams would have been necessary. Furthermore, now it is open the possibility of a full characterization of quite interesting aperiodic structures, like two-dimensional Thue-Morse, which have been studied until now only theoretically [Moretti 2007]. In fact, this kind of pattern could not be realized by multiple beam holography even in principle.

These quasicrystal structures, as well as the periodic one, are written into polymeric liquid crystal films, so to permit switching by external fields. The diffraction

efficiency measured on these samples was typically one order of magnitude larger with respect to that measured on similar quasicrystals written into polymer by means of multiple-beam holography by Gorkhali [Gorkhali 2006]. The efficiency measured was typically in the range of $\sim 10\% \div 30\%$ and did not show any dependence on polarization of the incident laser beam. In fact, it is my opinion that the quasicrystals produced had the typical morphology of PDLC, circumstance that was confirmed from the voltage independence of the diffraction efficiency too. This behavior might be due, in fact, to the existence of a PDLC morphology consisting of spherical liquid crystal microdomains (very small droplets) isotropically oriented inside the volume of the structure that cannot be reoriented by moderate external voltages due to their small size (see also Sec. 2.1.8 and 2.3.1). This result coincides with the experimental observation of the diffraction efficiency as a function of the external voltage presented measured by Gorkhali et al. [Gorkhali 2006] on polymeric quasicrystals fabricated with multiple-beam holography. They found only a very low efficiency modulation ($\sim 1\%$) by applying a moderate external voltage. The overall morphology of the LC-polymer quasicrystal compounds obtained with the SLM-CGH technique is comparable to the PDLC-like morphology induced by multiple-beam holography, whereas the larger diffraction efficiency that I measured on my samples may be due to the larger pitch of the structures (limited to $\sim 1\mu m$ at the present).

In conclusion, further research is necessary to optimize the fabrication process of soft matter quasicrystals having high rotational symmetries in order to produce reliable and efficient active photonic devices based on this kind of materials.

3.2.5 Structures with Defects written with a Single-step Process

The SLM-CGH technique permits to obtain not only periodic structures but also quasiperiodic. Moreover, every kind of complex pattern may be encoded in a CGH with the only limitation of the SLM-display resolution. As a result, the SLM is able to project binary intensity profiles in order to increase the amplitude of the dielectric modulation in writing periodic, quasiperiodic and even disordered structures. Although holographic lithography permits to achieve the same result by using a process with a threshold level thanks to the typical employment of compounds with a photoresist developed with a chemical etching mechanism, whereas the same effect is difficult to achieve in a photosensitive polymer mixture. Instead, this is possible by using a binary intensity pattern with the SLM-CGH technique. Moreover, interesting possibilities may be explored by combining the SLM technique and the lithography of hard materials. In this work, I realized several examples of structures by using a binary intensity profile that I will show hereinafter in this section. The octagonal quasiperiodic structures represented in Fig. 3.29-(c) and (d) are calculated, as for instance, by inserting a threshold level into the intensity profiles depicted in (a) and (b). These 8-fold quasiperiodic patterns have been defined previously (see Sec. 3.1.5.1) and already shown in Fig. 3.14-(a) and (b), respectively. I will discuss in the last sections the PBG properties of these quasicrystals presenting interesting

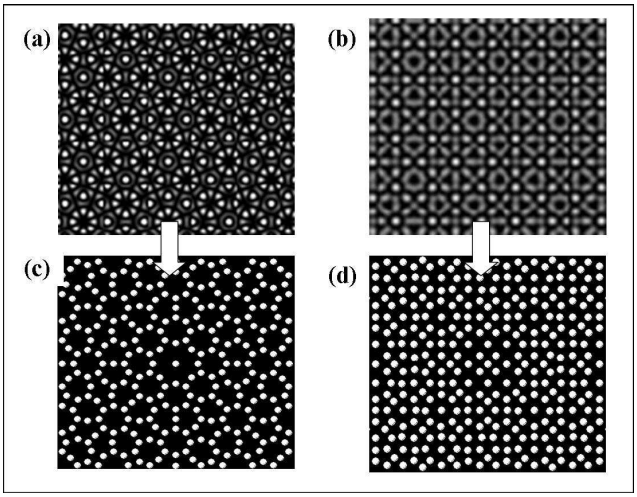

Figure 3.29: (a)-(b) Calculated octagonal quasiperiodic intensity profiles obtained by changing the relative phases of the interfering beams; (c)-(d) binary intensity profiles obtained inserting a threshold level into the intensity images (a) and (b), respectively.

results.

As discussed about PhCs and PhQCs in the previous chapter, it is by inserting defects into a PBG material that it is possible to exploit the important properties of the photonic structures so to realize optoelectronic devices. The CGH-based technique that I developed consents to design and to write with a single-step process almost any kind of structure including patterns possessing point-like, linear defects and complex layout of defects too.

Due to the limited experimental instruments[5], the images of the structures here shown have been realized with an optical microscope. Therefore, the samples have been realized with a tile size[6] a larger (in the range $\sim 2.5 \div 5\mu m$) so that the design of the structures could be easily visible. Now I will present several examples of structures with defects that I realized with the SLM-CGH technique. The samples have been written with a single process of optical curing starting from a precalculated intensity profile possessing the desired design of defects. In Fig. 3.30 a defect Y-channel in a hexagonal LC-polymer pattern is shown. The insets (a), (b) and (c) represent the experimental structure produced (detail), the experimental writing intensity and the precalculated intensity profile, respectively.

Several examples of 8-fold(B) quasiperiodic structures are shown in Fig. 3.31. The samples have been cured with binary intensity pattern in order to increase the

[5]The SEM images previously shown in Fig. 3.24 have been acquired in the laboratories of the University "Politecnica delle Marche" of Ancona in collaboration with the group of Pr. F. Simoni.

[6]The size a of the unit tile of the quasiperiodic patterns may be considered as a generalization of the lattice constant of the periodic structures, in fact the tile size a coincides with the lattice constant in the case of periodic crystals.

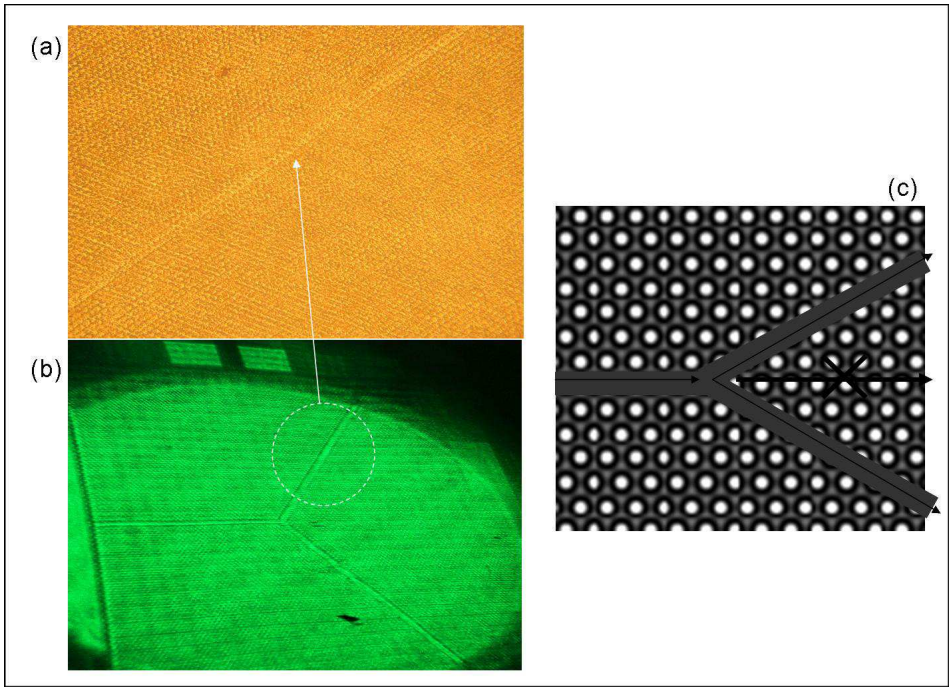

Figure 3.30: Linear defect with a Y-channel layout in a hexagonal pattern: (a) detail of the channel of the experimental structure produced; (b) experimental writing intensity; (c) schematic representation of the precalculated intensity profile.

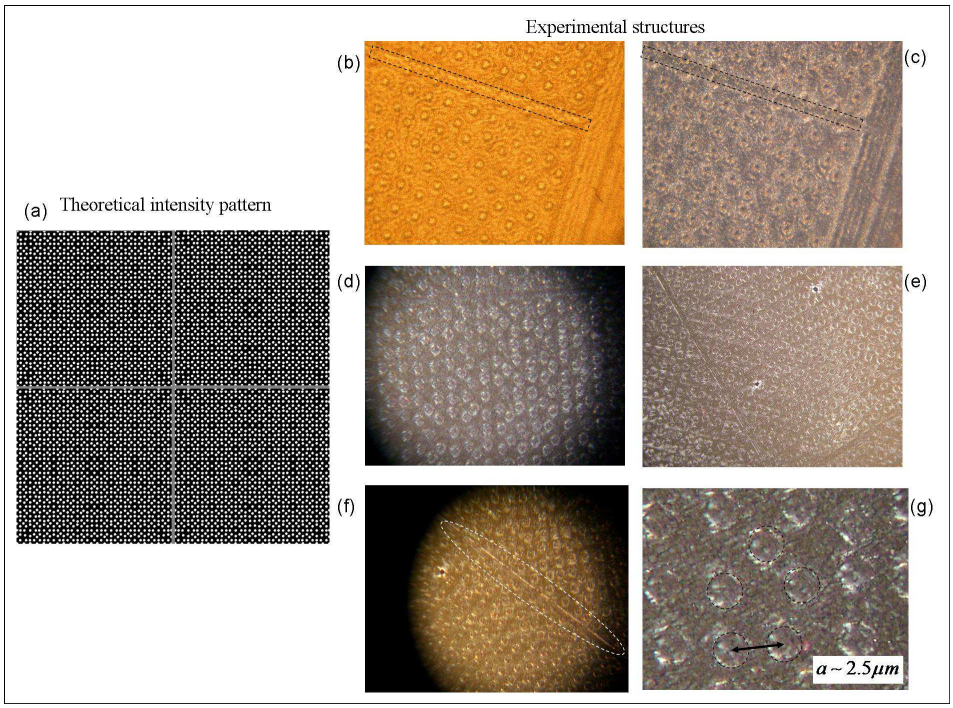

Figure 3.31: 8-fold(B) quasiperiodic structures: (a) schematic representation of the intensity pattern with perpendicular defect linear channels; (b) resulting structure realized in the sample; (c) the same structure taken under crossed polarizers; (d) same quasiperiodic sample with an increased aspect ratio; (e)-(f) details of the defect channels; (g) detail of the tiling geometry of the polymer rods.

phase separation between liquid crystal and polymer. The schematic representation of the intensity pattern in the inset (a) shows two perpendicular linear channels. The resulting structure realized in the sample is shown in the inset (b). In the inset (c), the image of the same structure taken under crossed polarizers shows a pattern of polymer rods into a homogeneous liquid crystal-polymer compound. The detail of a linear channel is also evident into the dashed rectangular. By varying the diameter of the intensity spots it is possible to modify the filling factor of the dielectric rods with respect to total area of the pattern as shown in the inset (d) in which the aspect ratio (between the rods diameter and the tile size) has been increased. Insets (e) and (f) show a detail of the perpendicular channels in the same 8-fold quasicrystal, whereas the particular tiling of the structure is presented in inset (g) where $a \simeq 2.5\mu m$. The diffraction pattern confirmed the 8-fold rotational symmetry of the quasicrystal. The efficiency of diffraction of this kind of structures realized with a binary intensity profile do not vary by changing the angle of incidence and polarization of the incident beam and has a typical value in the range $\sim 15\% \div 30\%$. The sizes of the defects may be controlled with high accuracy as demonstrated

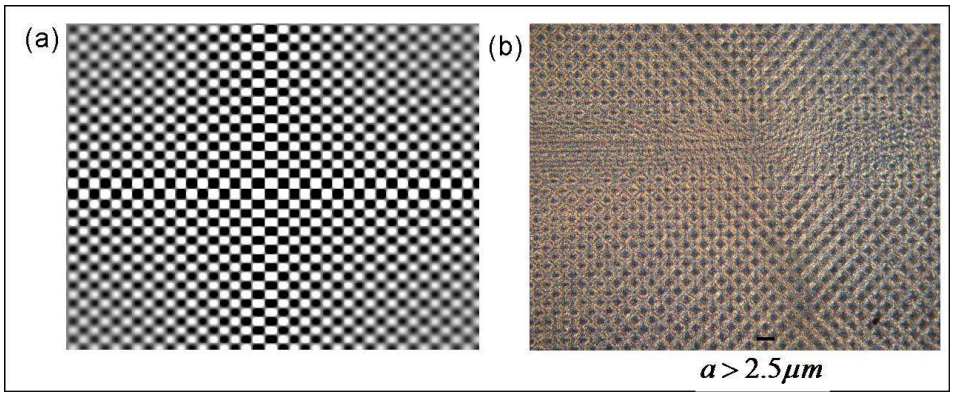

Figure 3.32: (a) Intensity profile obtained as the product of two Bessel functions and used to produce the corresponding structure (b).

from the particular structure shown in Fig. 3.32. The inset (a) represents the intensity profile used to write the structure and was calculated as the product of two Bessel functions, therefore the zeros of the function determine the variable size of the rectangular dielectric regions, decreasing from the center to the boundary. This is an example of the potentiality of writing of the technique. The resulting sample is shown in the inset (b) of the same figure. The image is taken between crossed polarizers and indicates a good separation of the liquid crystal and polymer components.

3.2.6 Experimental Setup (III): Interference-based Scheme

The limitations in the writing resolution of the periodic, quasiperiodic and aperiodic structures is due to the limited pixel size of the SLM-display and to the writing

wavelength when using the spatial light modulator to project the writing irradiance directly onto the photosensitive compound. However, it is possible to exploit the modulation capability of this technique using a different approach, as for instance to control the amplitude and phase property of the beams in a two-beam holography process. In this thesis I used the SLM exploiting its potentiality of encoding any kind of optical element, conventional or not, to realize an interference-based scheme (IS) in order to overcome the resolution limitations imposed by our device. In a recent paper, Yang and coworkers used an octagonal pyramidal prism [Yang 2006] to realize an 8-fold quasiperiodic pattern by exploiting the interference produced at the bottom of the prism. The key element is the prism which plays the roles of both splitting the incident single laser beam into eight (or even nine) interference beams and then combining the beams again to encode an intensity pattern under the bottom of the prism. The typical pitch of the interference profile is related to deflection angle of the prism faces. The basic idea in my case is to use the SLM and a suitable CGH

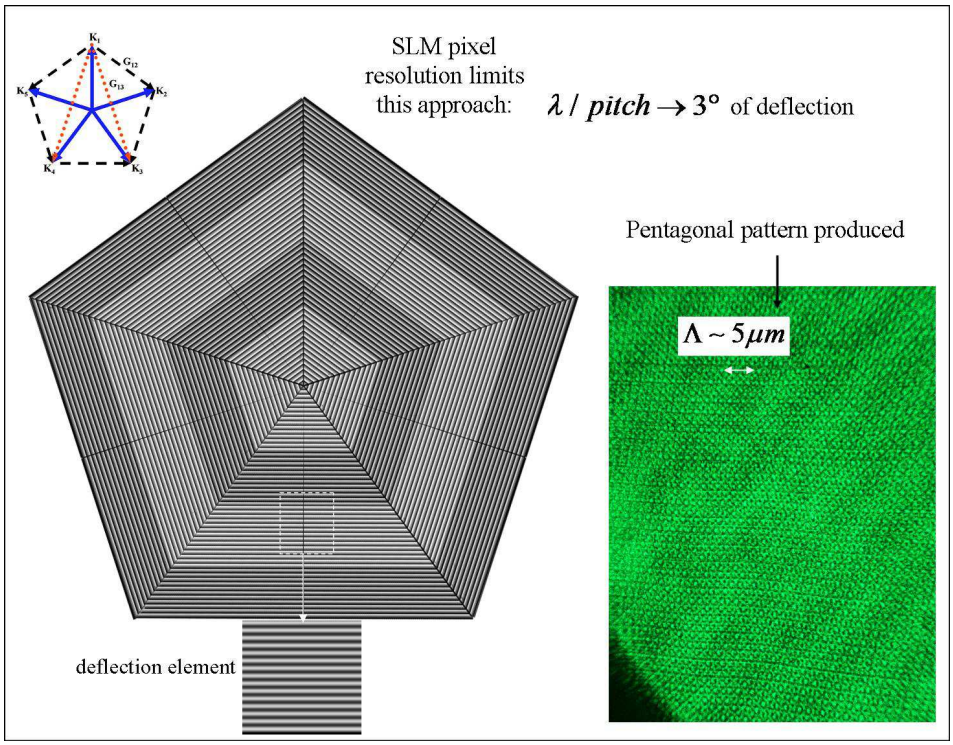

Figure 3.33: (left part) Phase CGH having the same role of a pentagonal prism and (upper inset) five-beam geometry; (right part) fivefold interference profile produced the prism-like CGH.

to realize a phase optical element having the same role of the prism described in the paper of Yang. For this purpose, I realized a pentagonal pyramidal prism as a CGH. The schematic representation of this particular phase prism is shown in Fig. 3.33. Each face of the prism is a deflection phase element similar to an optical

wedge and to a diffraction grating. By combining five triangular phase gratings opportunely it is possible to obtain in regular pentagonal phase prism as depicted in the left part of the figure. The five-beam geometry with the respective wavevectors is also represented in the upper inset of the figure. The drawback of this approach is related again to the pixel size. In fact, the maximum deflection of the beams achievable is determined by the ratio between the pixel size and the wavelength of the beam incident on the phase prism, operating at $532nm$. The linear variation of the phase as a function of the spatial coordinate (the pixel position) defines the deflection angle of each grating element. The fastest variation, that is the maximum angular deviation, is determined by the pixel size and corresponds to a deflection of only 3°. Consequently, the fivefold interference profile produced in this way has a typical tile size of $\sim 5\mu m$ as shown in the right inset of Fig. 3.33. To overcome

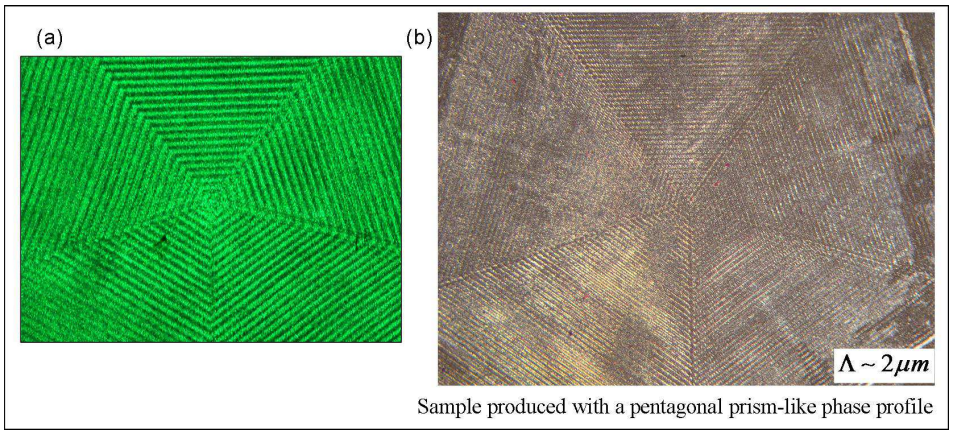

Figure 3.34: (a) Writing intensity used to transfer the phase prism to a polymeric sample; (b) sample produced with a pentagonal prism-like phase profile.

this problem I transferred the phase prism to a polymeric sample with the direct writing method. By doing this, in fact, the resolution is increased approximately of a factor 10 and hence a deflection of 30° is correspondingly achievable by exploiting the sample as the projecting system of the fivefold interference profile. The writing intensity profile that I used to transfer the prism-like phase profile (as a combination of five deflection gratings) to the polymeric sample is depicted in Fig. 3.34-(a). The resulting sample is shown in the inset (b) of the same figure, in which the desired structure is clearly evident.

Figure 3.35, instead, shows the diffraction pattern produced by the polymeric sample with the prism-like structure manifesting the expected fivefold symmetry: such diffraction pattern, in fact, corresponds to the Fourier transform of the 5-fold interference profile projected by the polymeric sample. Unfortunately, since now I have not had the possibility to use the realized sample as the projecting element and therefore to induce the formation of a fivefold dielectric modulation of higher resolution into a LC-polymer compound.

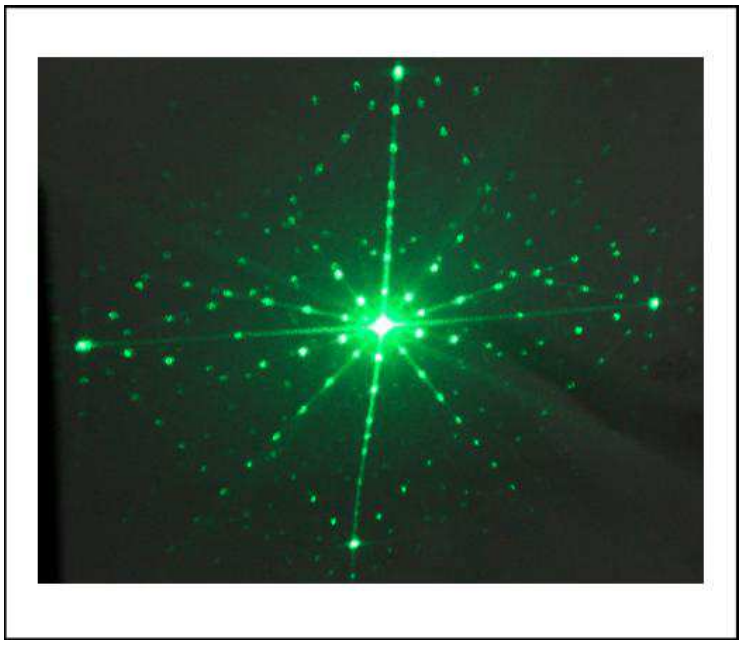

Figure 3.35: Diffraction pattern corresponding to the Fourier transform of the 5-fold interference profile projected by the polymeric sample.

3.3 Theoretical Analysis: Finite Difference Time Domain Simulations

In this section, I will demonstrate the importance of the tiling geometry in the arrangement of a quasicrystal structure. A typical ideal quasicrystal structure with geometric tiling is made of infinitely-long dielectric cylinders placed at the vertices of a N-fold-symmetric aperiodic tiling with lattice constant (tile side-length) a, generated by the so called Stampfli inflation rules [Oxborrow 1993]. For the fivefold symmetry originally defined by Penrose, as for instance, a useful reference is the paper of Levine [Levine 1984]. Differently from the results obtained by Hiett ([Hiett 2003]) about the dodecagonal structure (analyzed also by Zoorob [Zoorob 2000]) according to which different tiling geometries ("triangle-triangle" and "square-square" unit tiles in particular) did not influence the PBG properties that they numerically calculated, I found that the tiling geometry and hence the specific design of the quasicrystal (despite its rotational symmetry) deeply influences the photonic bandgap of quasiperiodic structures. Although the results that I obtained are related to a different symmetry, that is the octagonal in particular, such results demonstrate the importance of the specific arrangement of the pattern in determining its properties. In other words, the cases examined by Hiett are possibly specific of the dodecagonal quasicrystal. I will show, by Finite Difference Time Domain (FDTD) simulations of the transmission spectra in several 8-fold quasiperiodic patterns, the influence of different building tile geometries on the photonic band-gap for low refractive index

contrasts. This demonstrates the importance of an accurate control of the writing pattern to produce feasible photonic band-gap structures with low refractive index materials. The typical interference patterns obtained changing the relative phases of eight interfering light beams in a multiple-beam process (examples are shown in 3.14 of Sec. 3.1.5.1 and 3.26) produce structures with important differences in the dielectric distribution with respect to the standard geometric tiling of space. For octagonal quasicrystals, the building unitary tile, known as Ammann-Beenker tiling, consists of "squares" and "rhombuses" of equal side lengths a (see [Zhou 2007], [Socolar 1989] and also [Romero-Vivas 2005] for details), while the interference patterns, typically, give rise to completely different arrangements. Usually, the PhQCs possessing a PBG have been realized in hard materials [Mao 2006] or using a direct writing technique [Zhou 2007] by fabricating the structure with a geometric tiling, while the resulting tiling in the case of an interference pattern may strongly affect the PBG properties of the quasicrystal. Therefore, the question is to understand if the rotational symmetry is the only parameter affecting the properties of the photonic band-gap (if it exists) or if the particular arrangement and design of the quasicrystal may influence the PBG. At the present, the comprehension of the behavior and of the characteristics that this kind of photonic structures manifest is very limited. I will discuss the case of octagonal crystal because its building tile is easier to analyze with respect to other structures like Penrose or dodecagonal. I will analyze and compare the standard octagonal and 8-fold interferential patterns with different unit-tiles to provide a comprehension of the behavior of the photonic band-gap with respect to the building tile, the variation of the refractive index difference Δn and the filling factor (defined as the ratio between high dielectric constant area and the overall area of the structure). I will show interesting results about quasiperiodic structures that highlight the importance of the possible advantages introduced by the SLM-CGH technique. In fact, this technique permits to control with high accuracy the required characteristics of the structure like the building tile without the limitations of fabrication imposed by the interference processes in achieving the desired dielectric distribution. In fact, as previously demonstrated, I was able to produce structures achievable with the multiple-beam holography like 2D quasiperiodic patterns (of rotational symmetry as high as 23-fold) as well as structures possessing a geometric tiling and structures with an aperiodic tiling (2D Thue-Morse) that cannot be realized using N-beam interference even in principle. These results demonstrate well the potential of the SLM-CGH technique. I will also present interesting theoretical results about other quasiperiodic crystals like the fivefold (Penrose or pentagonal) and the twelvefold (dodecagonal).

Unfortunately, since now, experimental measurements of the transmission spectra on the sample realized in this work have not been possible due to our instrumental limitations. At the present, we are studying possible collaborations to overcome these problems.

3.3.1 Influence of the Tiling Geometry on the PBG properties

The octagonal structure analyzed here is supposed made of dielectric rods with the Ammann-Beenker tiling of space, in air. The positions of the cylinders of radius r are coincident with the vertices of "squares" and "45° rhombuses" with sides of equal length a. It has been demonstrated that this structure presents a complete PBG with a very low threshold value for the refractive index difference ($\Delta n = 0.26$) between high and low dielectric materials, whereas the gap width to midgap ratio ($\Delta\lambda/\lambda_m$) becomes close to 5% for $\Delta n = 0.45$ [Romero-Vivas 2005]. Therefore, optoelectronics devices based on the octagonal photonic quasicrystal promise to be realized in silica, a very common telecommunication optical material, or even in soft materials like polymer.

For this purpose, holographic technique represents a very important fabrication method. Depending on the threshold level of the photosensitive matter and the exposure time, the filling factor may have different values. Typically, the maxima positions of the light pattern correspond to the high dielectric regions, that, usually, can be approximated with a structure of dielectric rods in air (or other materials). Despite the multiple-beam process, the SLM-CGH method permits to write directly a binary pattern as discussed in the previous section (see Fig. 3.29). Therefore the binary approximation is reasonable.

As already described, by adjusting the holographic parameters like the relative initial phases of the beams different interference patterns can be obtained as reported in Fig. 3.14. Therefore, different arrangements of the rods in air may be realized, depending on the resulting interferential profiles, as shown in Fig. 3.29 where two octagonal binary patterns, obtained for two different sets of the initial phases, are reported. In particular, for the first pattern, say, 8-fold(A), the phases were supposed to be all equal, that is $\phi_1 = \ldots = \phi_8 = 0$, whereas for the second pattern, say, 8-fold(B), the phases were periodically shifted of $\pi/2$, that is $\phi_1 = \phi_5 = 0$, $\phi_2 = \phi_4 = \phi_6 = \phi_8 = \pi/2$, $\phi_3 = \phi_7 = \pi$. The intensity profiles calculated for both the 8-fold(A) and 8-fold(B) structures are shown in Fig. 3.14-(a) and -(b), respectively. The corresponding patterns of rods here analyzed are shown in Fig. 3.36-(a) and-(b), respectively, where their patterns may be compared with the Ammann-Beenker octagonal tiling depicted in the inset (c) of the same figure. I designed the 8-fold(B) pattern trying to reproduce a quasiperiodic intensity profile that could be very similar to the geometric Ammann-Beenker octagonal so that the created structure could have similar PBG characteristics. By using an iterative algorithm similar to the AA algorithm before described, I calculated the phase values that could induce the formation of a constructive interference pattern in accordance with a precalculated array of positions in which circular rods were placed. I studied several resulting patterns among which the 8-fold(B) structure demonstrated very interesting properties.

All the structures here analyzed have been designed by positioning circular dielectric rods of radius r in the maxima coordinates of the interferential intensity patterns of Fig. 3.14-(a) and -(b), respectively. In the octagonal structure of

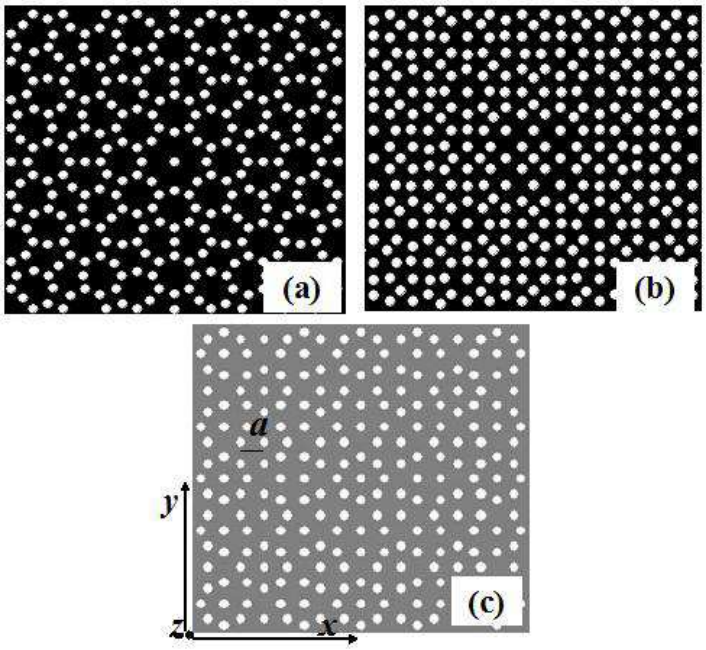

Figure 3.36: (a) Dielectric structure of rods from 8-fold(A) pattern; (b) dielectric structure of rods from 8-fold(B) pattern; (c) octagonal structure of rods with "square-rhombus" tile of equal side lengths a.

rods with the Ammann-Beenker tiling of space (Fig. 3.36-(c)) the side length of the unit-tile of space is a. Due to the non-geometric procedure of building the structures depicted in Fig. 3.36-(a) and -(b), I found more convenient to define as characteristic length of the patterns a new parameter, that is the average distance a_d between neighboring rods along the x-direction. The 2D finite difference time domain (FDTD) method with uniaxial perfectly matched layer (PML) boundary conditions was used in all simulations. FDTD algorithms are well known in literature [Sullivan 2000], they exploit the numerical discretization of time and spatial variation of the electromagnetic fields and Maxwell equations into the structure of interest. For this purpose I used the Photonics Cad-Suite R-Soft. The photonic quasicrystals examined were non-periodic in the translational direction and the supercell approximation, necessary in these cases, required very long computational time [Gauthier 2005]. The FDTD technique, instead, was faster and very accurate. I employed this approach to obtain transmission information, through the (x,y) plane (Fig. 3.36), as a function of propagation direction, wavelength and polarization. A Gaussian time-pulse excitation was placed in several points of the structure (in different simulations). The pulse was wide enough in frequency domain to cover the range of frequencies of interest. Several detectors were placed in particular positions and allowed us to store field components. Their positions were chosen to cover the angular range related to the 8-fold rotational symmetry (45°) and the mirror symmetry with respect to a line of 22.5° in each 45° sector [Hase 2002], with an angular separation from 5° to 15°. After a sufficiently large time of calculation, the field was Fourier-transformed to calculate the transmission spectrum with very high frequency resolution. The corresponding wavelength range was $(0.1 - 6.0)\mu m$ with a resolution of $\delta\lambda = 5.0 \times 10^{-4}\mu m$. The transmission coefficient through the system was calculated for different values of the dielectric constant of the rods in air, for both polarization TM (electric field E_z parallel to the rod axis) and TE (magnetic field H_z parallel to the rod axis) [Chan 1998], for each detector, that is for different propagation directions of the time-pulse excitation. The discretization grid provided a minimum of 100 grid points per free space wavelength. The transmission coefficient, normalized with respect to the incident power of the source, was calculated as a function of the variation of the filling fraction r/a_d, given as the rod radius to average distance ratio. The parameter r/a_d is related to the filling factor and it was varied in order to maximize the gap width of the octagonal structure for fixed refractive index difference $\Delta n = 0.65$. I found that interesting values were in the range $r/a_d \sim (0.15 - 0.35)$, with a maximum band width at $r/a_d \backsimeq 0.24$ ($r/a \backsimeq 0.34$). The value of r/a_d was held fixed in all simulations analyzed here for comparison. The data collected from the detectors placed at different positions and angular orientations had the same overall shape for all the transmission spectra I investigated here, demonstrating the isotropy of the structures with respect to the propagation direction of the excitation source and, hence, the existence of a complete photonic band-gap. In Fig. 3.37, the transmission spectra of the octagonal pattern of Fig. 3.36-(c) is shown for TM polarization as a function of the refractive index difference Δn. The spectra are shifted in the vertical direction to permit

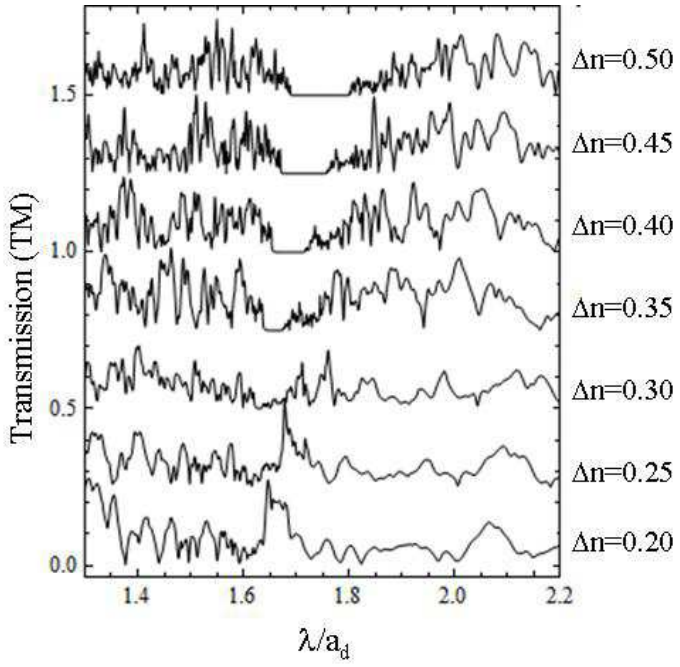

Figure 3.37: Transmission spectra (TM polarization) of the octagonal pattern (Ammann-Beenker tiling) for several values of the refractive index difference Δn.

comparison. We see that an index difference of $\Delta n \backsimeq 0.3$ is needed to form the band-gap at the free space mid-gap wavelength $\lambda_m = 1.62\mu m$ (corresponding to the tile length $a = 0.93\mu m$ and the average distance $a_d = 1.0\mu m$), with a gap width to midgap ratio $\Delta\lambda/\lambda_m \sim 0.3\%$. The PBG had $\Delta\lambda/\lambda_m = 6.3\%$ at $\lambda_m = 1.74\mu m$ for $\Delta n = 0.5$ and increased up to $\Delta\lambda/\lambda_m \sim 22.6\%$ at $\lambda_m = 2.21\mu m$ for $\Delta n = 1.0$ (not shown in Fig. 3.37). The mid-gap free space wavelength λ_m varied with Δn because the increasing of the index difference corresponds to increasing of the average refractive index. I did not find a clear PBG in the octagonal pattern of Fig. 3.36-(c) for the TE polarization. My simulations showed, in fact, only a very narrow PBG with a relative width $< 1\%$ for $\Delta n = 0.9$ around $1.48\mu m$, whereas in other regions of the spectra the possible presence of a band-gap was completely hidden by structures of multiple peaks that were related, probably, to localized modes (not shown here). Moreover, in the case of the TE polarization, the data collected from the detectors placed at different angular orientations demonstrated a dependence from the propagation direction.

In Fig. 3.38-(a) and -(b), respectively, the transmission coefficients in TM polarization of the 8-fold(A) and 8-fold(B) patterns (see Figs. 3.36-*a* and *b*) are shown, for a refractive index difference $Deltan = 1.5$. The two structures presented important differences. The pattern (A) had a PBG of $\Delta\lambda/\lambda_m = 19\%$ around $\lambda_m = 3.75\mu m$, whereas the pattern (B) had two band-gaps, one with a relative width $\Delta\lambda/\lambda_m = 13\%$

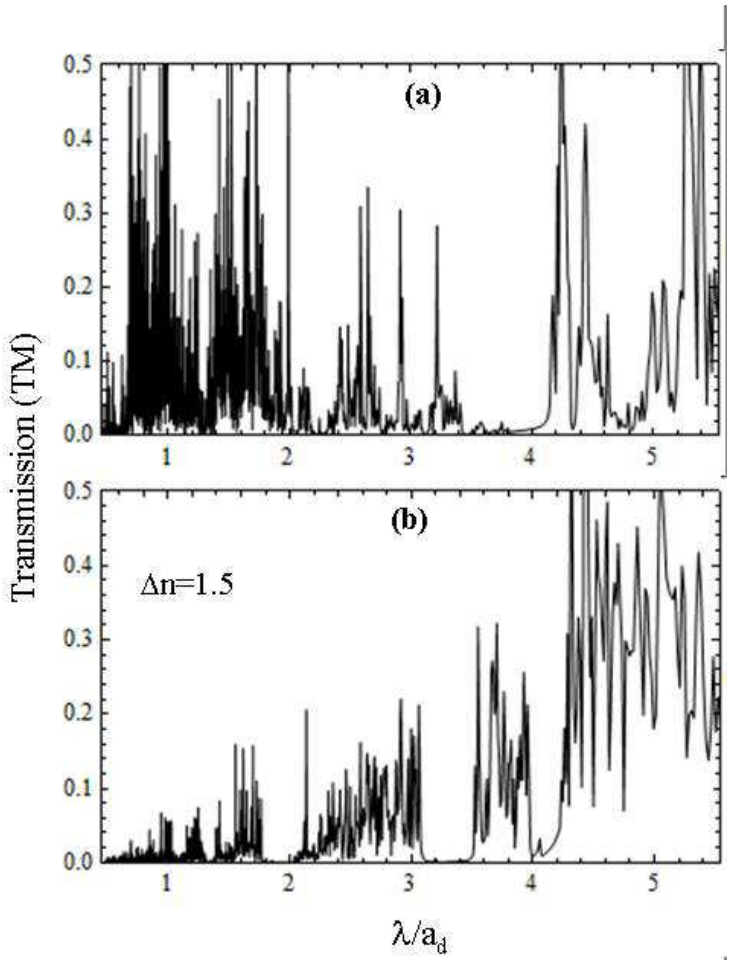

Figure 3.38: (a) Transmission spectrum (TM polarization) for the 8-fold(A) pattern with refractive index difference $\Delta n = 1.5$; (b) Transmission spectrum (TM polarization) for the 8-fold(B) pattern with $\Delta n = 1.5$.

at $\lambda_m = 1.93\mu m$ and the other of 12% at $3.30\mu m$. I analyzed the same structures for several values of the index contrast and TM polarization. I found that, in comparison with the octagonal structure, an index contrast larger of about a factor two was needed to open a PBG of comparable width to mid-gap ratio. Several TM transmission spectra for an index difference up to ~ 1.1 are shown in the next section for the 8-fold(B) (see FIg. 3.43). However, the most important results are for higher dielectric contrasts. The pattern (A) had a larger band-gap, but for longer wavelengths ($\lambda_m = 3.75\mu m$) with respect to the first band-gap of the pattern (B) and with respect to the PBG of the octagonal pattern of Fig 3.36-(c), that had $\lambda_m = 2.6\mu m$ for $\Delta n = 1.5$ (not shown in Fig. 3.37). On the other hand, the 8-fold(B) pattern, even with a smaller PBG, could work at shorter wavelengths ($\lambda_m = 1.93\mu m$). By changing the filling fraction the transmission spectra preserved the overall shape. Only a shift in the mid-gap wavelength was observed.

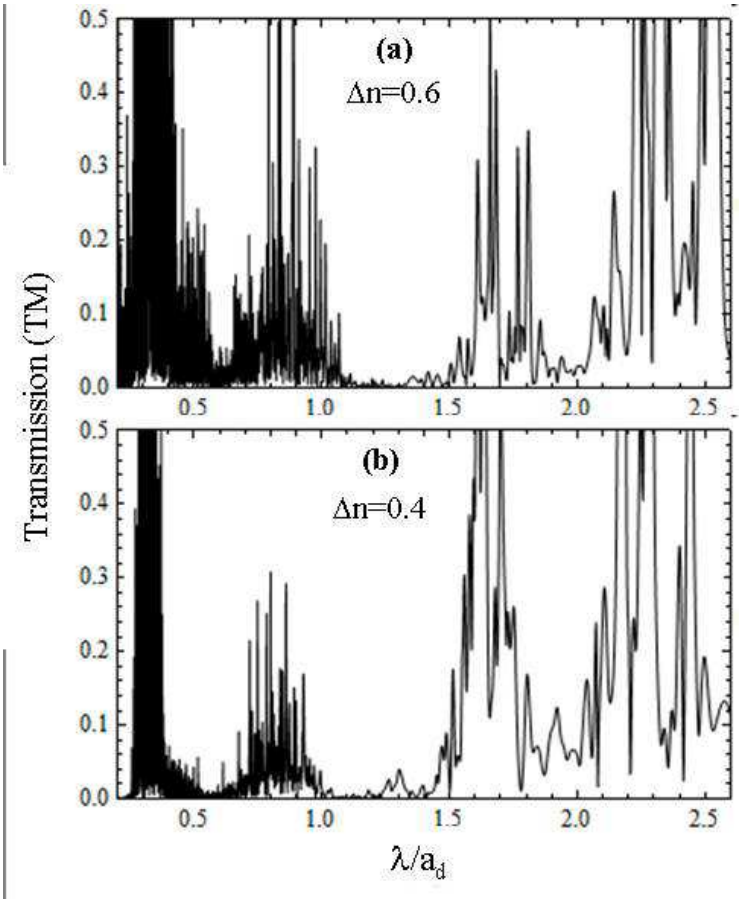

Figure 3.39: (a) Transmission spectrum (TE polarization) for the 8-fold(B) pattern with refractive index difference $\Delta n = 0.6$; (b) Transmission spectrum (TE polarization) for the 8-fold(B) pattern with $\Delta n = 0.4$.

Very interesting are the results related to the calculation of the transmission spec-

tra for the TE polarization. In Fig. 3.39-(a) and -(b), the transmission information in TE polarization related to the 8-fold(B) pattern, calculated supposing a refractive index difference $\Delta n = 0.6$ and $\Delta n = 0.4$, respectively, are shown. Two PBGs, independent from the propagation direction, were present, one for $\Delta n = 0.4$ with a relative width $\Delta\lambda/\lambda_m = 32\%$ at the mid-gap free space wavelength $\lambda_m = 1.25\mu m$ and the other for $\Delta n = 0.6$ with a relative width $\Delta\lambda/\lambda_m = 31\%$ at $\lambda_m = 1.30\mu m$: very short wavelengths in both cases compared to the other patterns. The peaks around $1.3\mu m$ were probably due the existence of localized modes. With the increasing of the refractive index difference only a shift in the mid-gap wavelength was observed, up to $2.25\mu m$ for $\Delta n = 1.6$. The 8-fold(A) pattern, on the other hand, did not present low index PBG for TE polarization (not shown here) as is also for the octagonal structure with the Ammann-Beenker tiling. I analyzed also the complementary dielectric structures of the 8-fold(A) and (B) patterns, that is circular rods of the low index material (air) embedded in the high index substrate. Also in this case no band-gap was observable for the low refractive index contrasts examined. Nevertheless, the simulations were performed only for TM polarization in this case.

The behavior of the 8-fold(B) pattern represents, in our opinion, a surprising result promising the implementation of reliable low index contrast PhQC devices in polymeric substrates. In fact, according to the TE transmission spectra for the 8-fold(B) pattern here presented, an average distance $a_d = 1.25\mu m$ between neighboring rods would be sufficient to induce a PBG at $\lambda_m = 1.55\mu m$. That being so, in spite of the resolution limitations of the SLM-CGH technique at the present time ($\sim 1\mu m$), the SLM-CGH technique could be actually employed to produce photonic quasicrystals for feasible and reliable applications. Moreover, generally speaking the scalability of the optical properties permits to use our quasiperiodic structures to study their interesting optical behavior by exploring the PBG characteristics in the infrared optical range. Currently, among the photonic crystals, only the periodic hexagonal crystal has shown an intersting low index bandgap with a threshold $\Delta n \simeq 0.3$, and having a PBG width of $\sim 5\%$ for $\Delta n \simeq 0.54$, but only for TM polarization. In Fig. 3.40 the TM (red) and TE (blue) band diagrams that I calculated with the FDTD algorithm supposing a LC-polymer hexagonal photonic crystal are shown. I imposed a difference of the refractive index of 0.54 between the low index rods ($r/a = 0.37$) embedded in a high index medium made of polymer. As it results from the inset (a) of this figure, the PBG opens around the normalized frequency $a/\lambda \simeq 0.5$, therefore a midgap wavelength operating at $1.55\mu m$ requires a lattice constant $a \sim 0.8\mu m$. Thus, the quasiperiodic structures here studied promise to be more efficient than periodic crystals.

3.3.2 Transmission Spectra for Pentagonal, Octagonal and Dodecagonal Quasicrystals

Let us discuss in detail the transmission spectra of several quasicrystals that are currently important candidates for the realization of PBG-based devices. In this

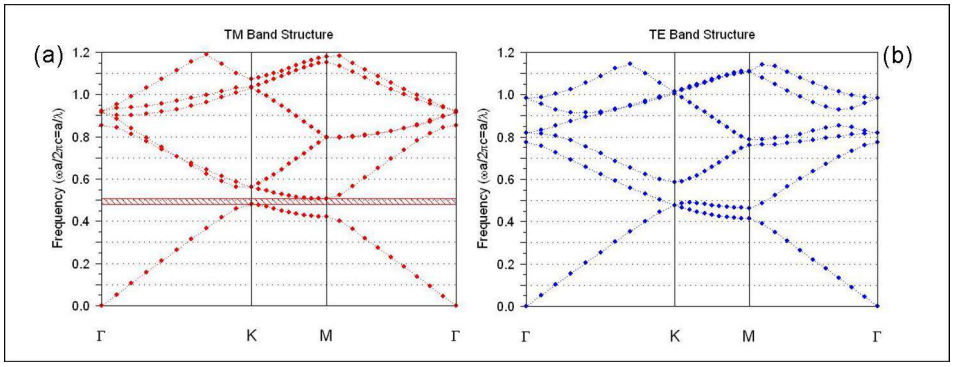

Figure 3.40: (a) TM (red curves) and (b) TE (blue curves) Band diagrams of 2D hexagonal crystal with refractive index difference $\Delta n = 0.54$, respectively.

section I will examine and compare the spectral information for low refractive index difference of the pentagonal, octagonal (Ammann-Beenker tiling), 8-fold(B) (that is the interference-based octagonal previously examined) and dodecagonal quasicrystals. The calculations have been performed as previously described if not differently specified.

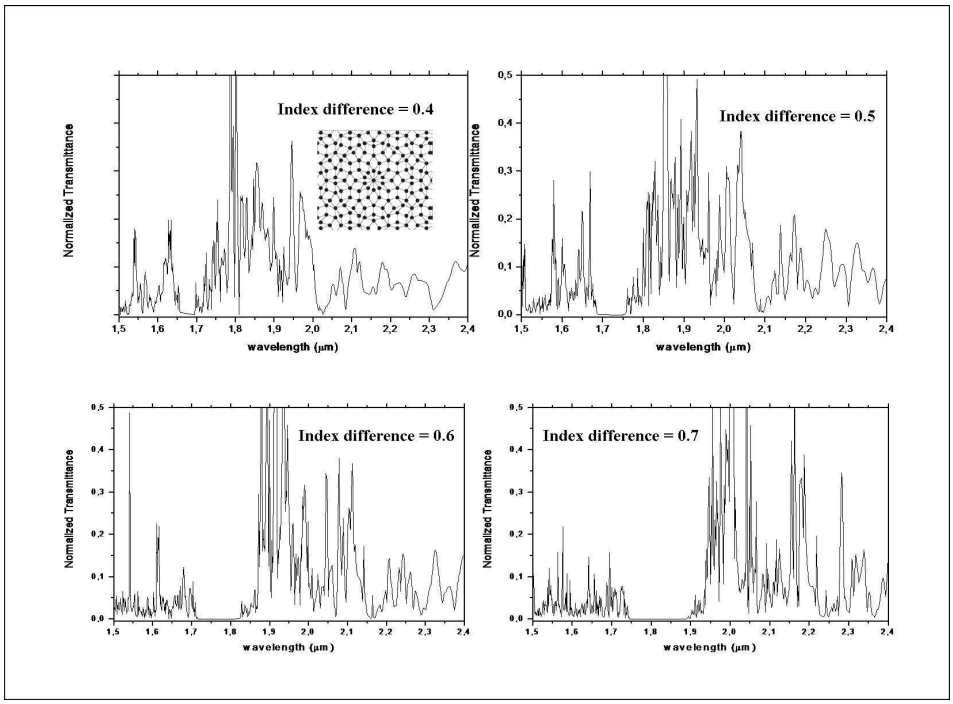

Figure 3.41: Transmission spectra for TM polarization for the Pentagonal quasicrystal with refractive index difference from $\Delta n = 0.4$ to $\Delta n = 0.7$.

Firstly, I want to introduce several interesting results that I found about the

fivefold and the 8-fold(B) structures. In Fig. 3.41 the transmission spectra for the fivefold quasicrystal, calculated supposing a time-pulse excitation propagating from the center of the pattern, are shown for refractive index differences in the range $\Delta n = (0.4 - 0.7)$. The inset in the left upper graph of the figure is a schematic representation of the quasicrystal structure obtained by placing the rods at the vertices of the tiling. As shown in the figure, the TM spectral gap near $1.7\mu m$ has a threshold value of the index contrast at $\Delta n = 0.4$. As shown in the left part of Fig. 3.42, the width increases for increasing values of the dielectric contrast and reaches a value of 10% and 13% for $\Delta n = 0.8$ and 0.9, respectively, at the miggap wavelength $\lambda_m \simeq 1.9\mu m$. On the right part of the same figure, the same TM transmission

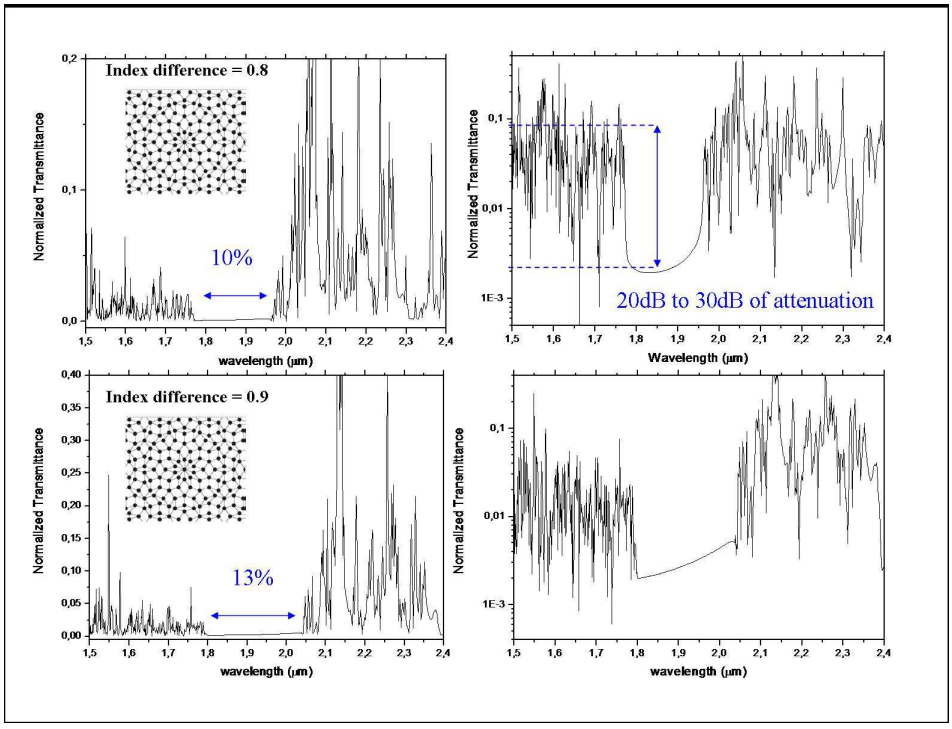

Figure 3.42: Transmission spectra for TM polarization for the Pentagonal quasicrystal with refractive index difference from $\Delta n = 0.4$ to $\Delta n = 0.7$.

spectra are reported in logarithmic scale to permit valuating the attenuation level in the spectral range of the gap, of the order of $20 \div 30dB$. For TE polarization I didn't find low contrast spectral gaps.

For the 8-fold(B) quasicrystal I studied the transmission spectra as function of the refractive contrast and as a function of the number of rods present in the structure so to verify the validity of the finite structure approximation. Moreover, the case of a non symmetric source position has also been treated, again for TM polarization. As it results from Fig. 3.43, the threshold value of the refractive index difference to open a PBG is 0.5 but with a negligible width. As summarized in the table reported in the right bottom part of the same figure, the PBG width increases

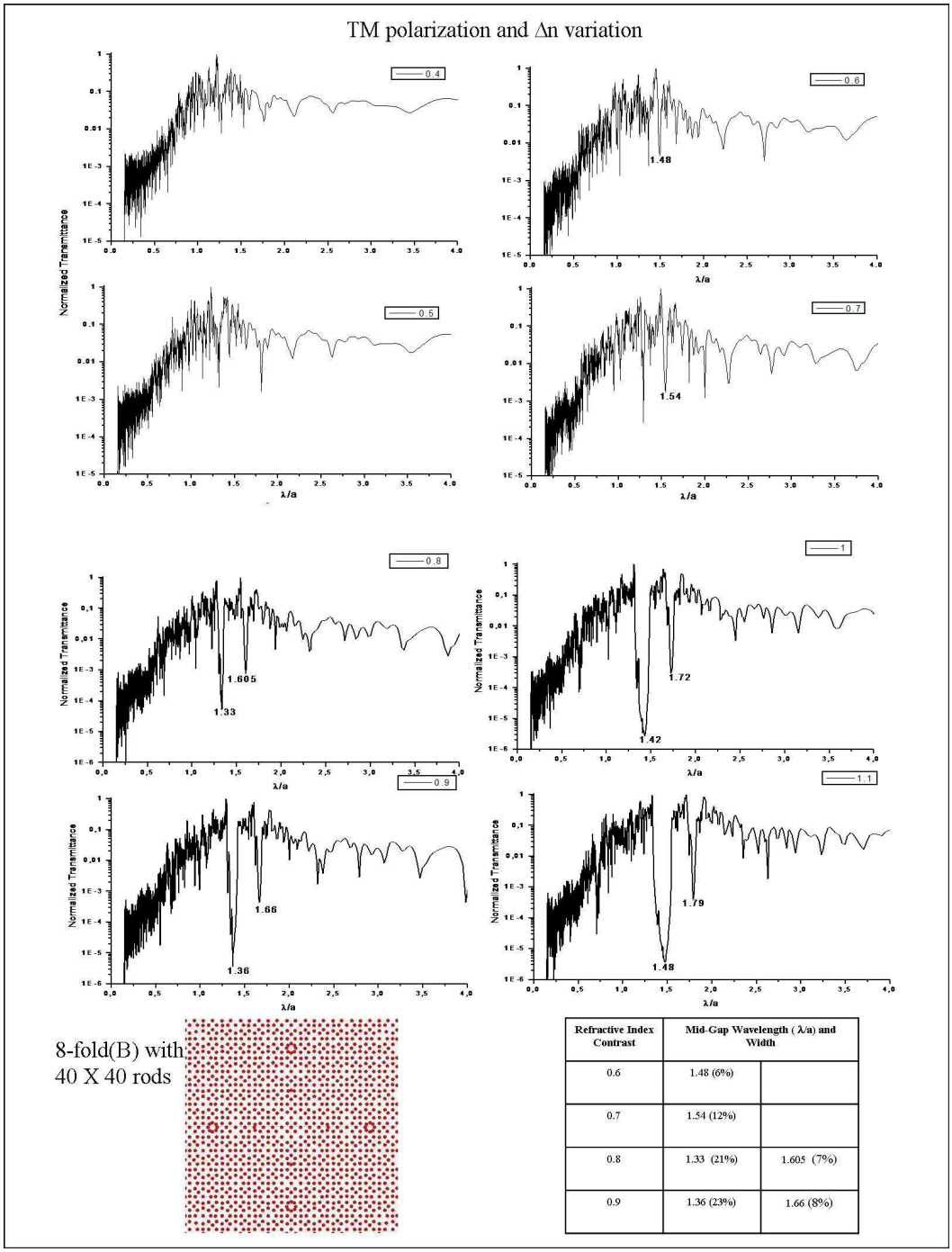

Refractive Index Contrast	Mid-Gap Wavelength (λ/a) and Width	
0.6	1.48 (6%)	
0.7	1.54 (12%)	
0.8	1.33 (21%)	1.605 (7%)
0.9	1.36 (23%)	1.66 (8%)

Figure 3.43: (Logarithmic) Transmission spectra for TM polarization for the 8-fold(B) quasicrystal with refractive index difference from $\Delta n = 0.4$ to $\Delta n = 1.1$; (bottom left) 40×40 rods design of the 8-fold(B) structure; (bottom right) Table resuming the principal data resulting from the transmission spectra reported in the figure.

to 12% for $\Delta n = 0.7$ and to 21% for $\Delta n = 0.8$. Therefore, very low contrast PBGs are not reliable for TM polarization, that is for $\Delta n \sim 0.2$, typical value found in the LC-polymer quasicrystals possessing a PDLC morphology. The PBG behavior in the case of TE polarization that I discussed in the previous section is currently the most interesting result for soft matter-based applications. From the simulations obtained translating the source position in a non symmetric point with respect to the rotational symmetry of the 8-fold pattern, the spectral gap dependence on the refractive contrast seemed to be not affected (for briefness not shown here). The only interesting aspect to be mentioned was a small change in the midgap wavelength of the PBGs, usually increasing with the refractive contrast and thus reducing the width to midgap ratio. Differently from the periodic crystals, the lack of translational symmetry in quasicrystals, in fact, yields to the existence of many inequivalent defect sites but also to different PBG characteristics related to inequivalent positions of the excitation source. This circumstance enlarges the field of probable photonic applications. Moreover, the PBG presence was not affected by decreasing the number of rods into the structure from 40×40 to 20×20 although also in this case I observed a shift towards higher values in the midgap wavelengths with a consequent decreasing of the PBG width. Therefore, unlike what have been observed in literature for periodic structures, the PBG characteristics are robust even with respect to the limited extensions of the quasicrystal area.

Let us now compare the results of the FDTD simulations between the fivefold Penrose, the Octagonal (Ammann Beenker tiling), the 8-fold(B) (interference quasicrystal) and the Dodecagonal (Stampfli inflation rule) quasicrystals. The simulations have been performed by comparing quasiperiodic structures having the same filling factor and the same value for the parameter r/a_d, as already described in the previous section. The principal data that resulted from the calculated transmission spectra are summarized in four tables shown for simplicity all in Fig.**??**. Each table refers to a specific quasicrystal structure and contains the normalized PBG widths and midgap wavelengths associated to the index contrasts supposed into the corresponding simulations. The corresponding transmission spectra are shown in Fig. 3.45 for a refractive index difference value equal to 0.4 (a), 0.5 (b) and 0.6 (c), respectively. To permit the comparison of the spectra and the related gaps, in each inset of the figure the curves corresponding to the various structures are collected together for each fixed index contrast: we have the fivefold Penrose (*Penro*-green curve), the Octagonal Geometric (*OctoG*-red curve) with Ammann Beenker tiling, the 8-fold(B) Interference-based (*P8int*-black curve) and the Dodecagonal (*Dodecag*-blue curve) structures. The tiling geometry of each quasicrystal is shown in the inset (d) of the same figure. It is worth noticing that the results here shown are for TM polarization, therefore at the present these transmission spectra cannot provide a comprehensive analysis of the properties of this kind of quasicrystals with the exception of the Octagonal and 8-fold(B) structures of which transmission information for TE polarization has been described in the previous section. Analogously to Fig. 3.45, the TM transmission spectra associated to the same structures and calculated for increasing values of the refractive index difference, in particular for

Penrose (5- or 10-fold)

Index Difference	Mid-gap Wavelength (λ/a)	Δλ/λ
0.4	-	-
0.5	1.43	0.04198
0.6	1.46	0.06403
0.7	1.52	0.1105
0.8	1.54	0.109
0.9	1.589	0.133
1.0	1.632	0.151

Dodecagonal (Stampfli inflation rule)

Index Difference	Mid-gap Wavelength (λ/a)	Δλ/λ
0.4	-	-
0.5	1.186	0.034
0.6	1.232	0.0725
0.7	1.28	0.102
0.8	1.329	0.136
0.9	1.382	0.153
1.0	1.43	0.172

Octagonal (Ammann-Beenker)

Index Difference	Mid-gap Wavelength (λ/a)	Δλ/λ
0.4	-	-
0.5	1.234	0.13
0.6	1.32	0.16
0.7	1.36	0.137
0.8	1.401	0.147
0.9	1.45	0.163
1.0	1.501	0.185

8-fold(B) (Interference Tiling)

Index Difference	Mid-gap Wavelength (λ/a)	Δλ/λ
0.4	-	-
0.5	-	-
0.6	1.49	0.04
0.7	1.53/1.2766	0.055/0.033
0.8	1.587/1.321	0.061/0.066
0.9	1.649/1.355	0.056/0.096
1.0	1.707/1.403	0.0566/0.124

Figure 3.44: Tables summarizing the results of the FDTD simulations performed on fivefold Penrose (left upper), the Octagonal (Ammann Beenker tiling) (left bottom), the 8-fold(B) (interference quasicrystal) (right bottom) and the Dodecagonal (Stampfli inflation rule) (right upper) quasicrystals: the data are related to the following figures.

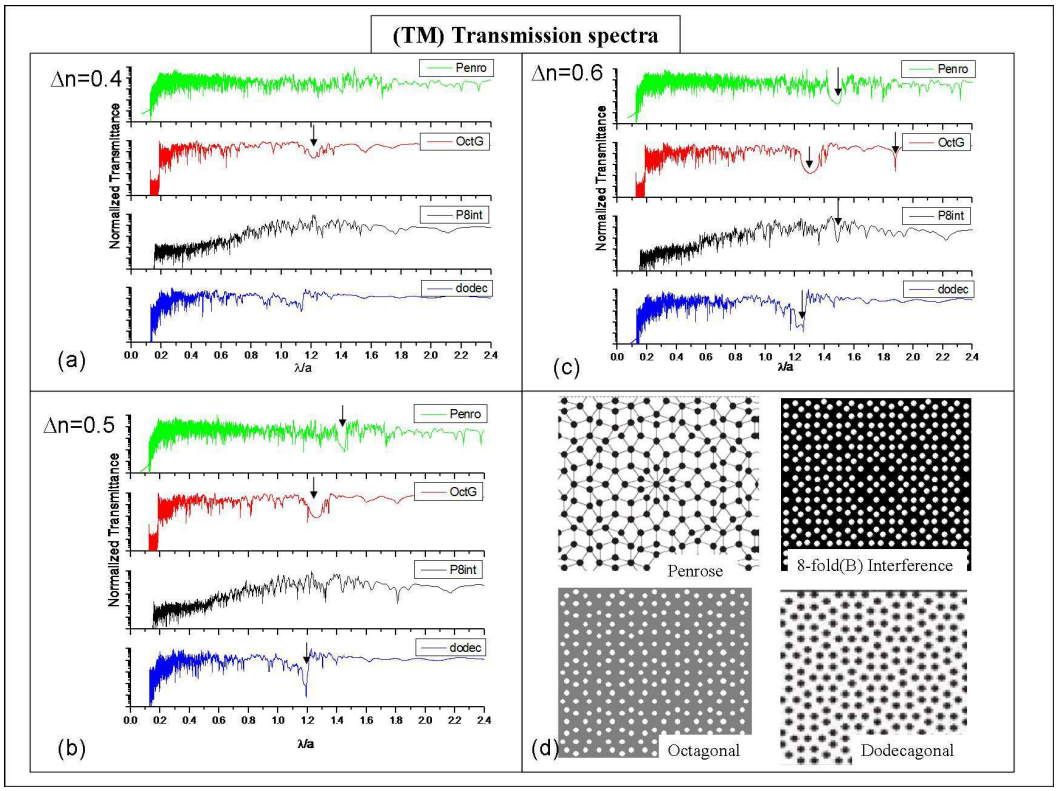

Figure 3.45: (a)-(c) insets, from the top to the bottom: TM transmission spectra of fivefold Penrose (*Penro*-green curve), Octagonal Geometric (*OctoG*-red curve) with Ammann Beenker tiling, 8-fold(B) (*P8int*-black curve) and the Dodecagonal (*Dodecag*-blue curve) quasicrystals in this order, for $\Delta n = 0.4$,0.5,0.6, respectively. (d) Inset: Penrose, Octagonal, 8-fold(B) Interference and Dodecagonal structures.

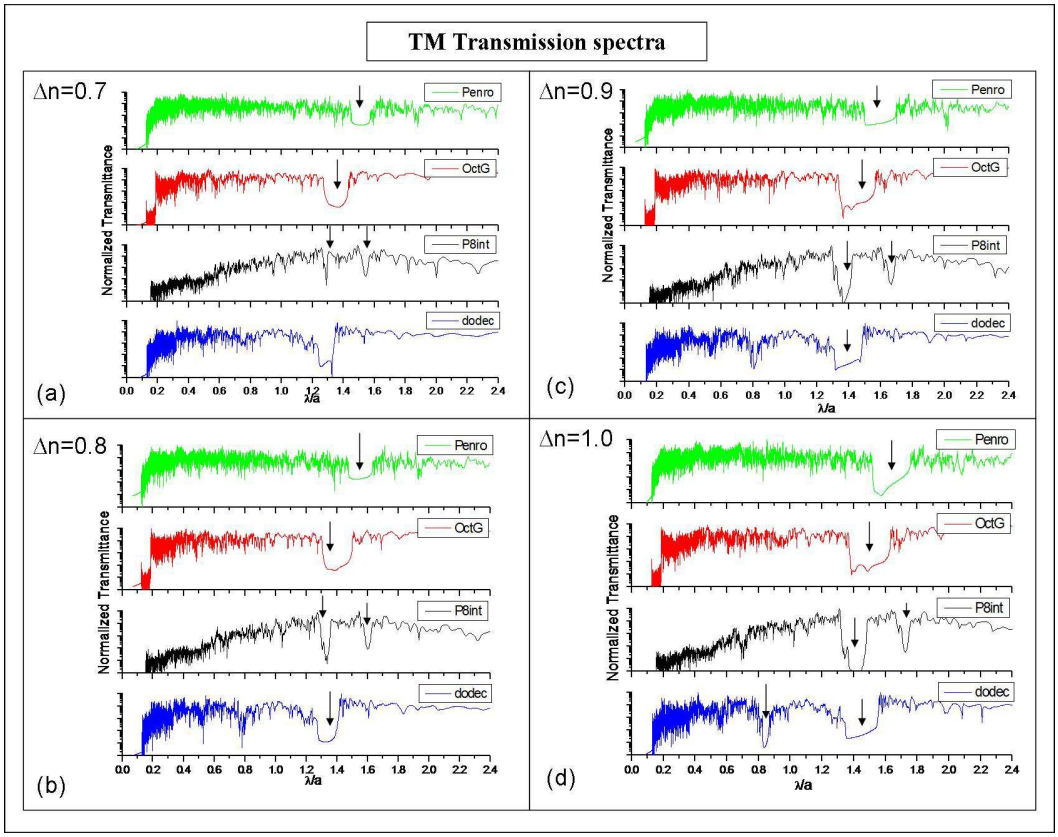

Figure 3.46: (a)-(d) insets, from the top to the bottom: TM transmission spectra of fivefold Penrose (*Penro*-green curve), Octagonal Geometric (*OctoG*-red curve) with Ammann Beenker tiling, 8-fold(B) (*P8int*-black curve) and the Dodecagonal (*Dodecag*-blue curve) quasicrystals in this order, for $\Delta n = 0.7$,0.8,0.9,1.0, respectively.

Δn = 0.7,0.8,0.9,1.0, are shown in Fig. 3.46, from (a) to (d), respectively. The results are very interesting. As it is possible to see from the tables of Fig. 3.44 and from the corresponding TM transmission curves of Figs. 3.45 and 3.46, higher rotational symmetries do not necessarily induce the opening of larger PBGs, at least in the case of low dielectric contrast here examined. The PBG properties of PhQCs seem to be specific of the structure depending not only on its particular rotational symmetry but also on the specific tiling geometry and on the consequent additional symmetries that may result in relation to the particular arrangement. As for instance, the Dodecagonal structure has a PBG of 3.4% for $\Delta n = 0.5$ whereas the Pentagonal and Octagonal quasicrystals have a PBG with $\Delta\lambda/\lambda_m \simeq 4.2\%$ and 13%, respectively, at the same refractive contrast. Although the 8-fold(B) pattern has shown a spectral gap with a relative width of $\sim 30\%$ for $\Delta n = 0.4$ for TE polarization, now for TM polarization it has a PBG of 4% for a threshold value $\Delta n = 0.6$. Although with a lower width, it shows two TM spectral gaps for increasing dielectric contrasts above $\Delta n = 0.6$ and up to a $\sim 12.4\%$ for $\Delta n = 1.0$. Although the results related to the Penrose, Octagonal and Dodecagonal quasicrystals are similar, the Octagonal structure seems to be the better candidate for soft matter-based photonic quasicrystals having large spectral gaps both for TE and TM polarization for low index differences. For TM polarization, in fact, the PBG width of the Octagonal pattern is in the range $(13\% - 18.5\%)$ for an index difference ranging between 0.3 and 1.0, as reported in details in the left bottom table of Fig. 3.44.

Chapter 4

Conclusions and Discussions

The technique of Spatial Light Modulation based on Computer-generated Holography has been successfully exploited to realize patterned samples made by a mixture of liquid crystal and polymeric composites. We expect that the SLM-based CGH technique may have a large impact on the production of complex photonic structures. We used Computer-Generated Holograms to drive a liquid crystal Spatial Light Modulator that permits to write arbitrary structures with simple and reliable optical setup. Highly reproducible patterns can be obtained over an area of hundreds of square millimeters with micrometric resolution and without drawbacks due to the long term stability of the holographic process.

- Our single-beam technique was developed with three different approaches (Fourier optics-based, direct imaging and interference-based) and allowed the realization of complex structures with micrometric resolution and with accurate control of the writing intensity distribution in the visible range. The irradiance pattern was, in fact, modified in real time by in-video addressing of the computer-generated holograms (CGHs), without the need for sophisticated mechanical control of the optical table and realignment of the optical elements.

- Regular patterned samples with good optical contrast were obtained, leading to Photonic Crystals (PhCs) structures with 1D, 2D, and 3D geometries. The arrangements have been verified with SEM images and optical and electro-optical characterization of the realized samples. The 1D volume phase gratings in the Bragg regime showed an interesting behavior possessing intermediate characteristics between the well known H-PDLC and POLICRYPS gratings. The diffraction efficiency measurements as a function of the angle of incidence and of the external applied voltage revealed a preferential alignment of the LC-molecules between the polymeric stripes and a peculiar polarization dependence. These circumstances highlighted that the gratings achieved were not H-PDLC nor POLICRYPS: they had the advantages of high diffraction efficiency (80%) and polarization dependence typical of POLICRYPS gratings but without their drawback of a vanishing efficiency for the s-polarization; moreover, they showed switching voltages similar to those observed in H-PDLC gratings. Furthermore, we realized a novel kind of grating possessing a periodic modulation both in the x and z-axis that showed efficiency characteristics never observed before and that probably may be used for particular optoelectronic devices.

- Regular but not periodic one- and two-dimensional structures were obtained, leading to Photonic Quasicrystals (PhQCs) of Penrose, Octagonal, Dodecagonal type. We were able to obtain with a single beam technique quasiperiodic Penrose-tiled structures with unprecedented rotational symmetry up to 17- and 23-fold and two-dimensional Thue-Morse structures too. To realize a 23-fold quasicrystal with the usual multi-beam holographic lithography, 23 interfering laser beams would have been necessary. These structures have been produced with the SLM-CGH technique thanks to its capability of writing arbitrary irradiance distribution with simple and reliable optical setup. In fact, robust and easily reproducible different pattern designs and tiling geometries can be achieved without mechanical motion and optical realignment, with complex arrangements and unprecedented rotational symmetries up to 17- and 23-fold. This opens the possibility of a full characterization of quite interesting aperiodic structures not achievable by multiple beam holography even in principle (like two-dimensional Thue-Morse) and that have been studied until now only theoretically [Moretti 2007]. The quality of our structures was demonstrated by the good agreement between the observed and calculated optical diffraction pattern. The characteristics of the structures were verified experimentally by measuring their diffraction efficiency as a function of the angle of incidence, incident polarization and applied voltage. The morphology that we found was typical of the PDLC structures and similar to the quasicrystals resulting from multi-beam holography.

- Moreover, samples with structures of defects were also produced with a single-step process. Several examples of point defects and linear defects have been showed.

- Theoretical FDTD studies of the transmission spectra and photonic properties of the fabricated structures have been discussed. The FDTD simulations demonstrated the importance of the choice of the geometric tiling in the fabrication process of the PhQCs. In fact, once the rotational symmetry is fixed, the unit-tile geometry deeply influences the characteristics of the photonic band-gap of the structures. Moreover, the PBG dependence on the rotational symmetry for low dielectric contrast quasicrystals has been discussed. The results that we found represent an important step towards the implementation of reliable photonic devices in soft materials. In conclusion, we showed, by FDTD simulations of the transmission spectra of several quasicrystals (Pentagonal, Octagonal, 8-fold Interference-based, Dodecagonal), that higher rotational symmetries do not necessarily induce the formation of larger PBGs, demonstrating the importance of an accurate control of the writing pattern to produce feasible photonic band-gap structures with low refractive index materials. Besides the Octagonal pattern with the Ammann-Beenker geometric tiling, the 8-fold(B) pattern of (see Sec. 3.3.1) was found very interesting among the interferential structures because it permits to obtain a large PBG for an index contrast as low as 0.4, as shown in Fig. 3.39.

- Our structures were written into polymeric liquid crystal films, so to permit switching by external fields [Gorkhali 2006], as experimentally demonstrated in this work. Although the refractive index contrast achievable with such a mixture, usually, is $\Delta n \sim 0.2-0.3$, the liquid crystal content can be removed to increase the index difference up to ~ 0.5. Different mixtures or materials can be used in order to increase the amplitude of the dielectric modulation. In fact, our holographic technique can be applied to any photosensitive material (e.g. with a larger index contrast), or to produce patterned masks and templates that can be used in lithography of hard materials [Mao 2006]. Moreover, we have demonstrated that photonic devices realized with low index contrast materials (e.g. polymers) could be feasible by exploiting proper geometries of the quasicrystal like for the 8-fold(B) structure that yields a PBG even in the case of very low dielectric contrast.

- The typical scale length of the structures realized in this work was in the range of 1-2μm. The scale length of the realized structures depended on the optical imaging system employed into the experimental holographic setup, which also affected the extension of the writing area. The achievable resolution, lastly, depends on the SLM pixel size and on the wavelength of the writing light. Using UV light and state-of-the-art SLM pixel size [Apter 2007], the limit in the spatial resolution could be improved by a factor of 3-4.

We are now studying different approaches to increase the resolution of the technique. We are working in order to obtain 2D quasicrystals with improved features not only in terms of spatial resolution but also in terms of better optical contrast by choosing a different material, so to match the demands for practical applications. Moreover, we are planning to achieve a complete characterization of the realized structures and of more complex structures, both with defects and with other kinds of photosensitive materials. Luminescence in holographically formed photonic band-gap structures might be an important research direction. We are working for selecting a dye suitable with our structures and other materials to increase the dielectric contrast. Further theoretical studies of the PhCs and PhQCs are also necessary, as for instance to explore the PBG properties of aperiodic structures, to search for opening of band gaps for decreasing index contrasts (increasing symmetry, tiling geometry, etc.) and to understand the localization and waveguiding properties in structures with defects.

In conclusion, the writing of dielectric modulations in soft matter composites using SLM and Computer-generated Holography is a real possibility. The feasibility of fabricating periodic and quasiperiodic crystals using SLM-CGH holography has been shown. An understanding of their utility as novel diffractive elements and photonic bandgap materials has just begun. The technique developed in this work offers interesting advantages with respect to the multiple-beam holography: it is a single-beam technique, it permits a wide choice of the light pattern designs, it avoids the necessity of a multi-beam optical setup and consequent mechanical control and optics realignment. We believe that the realized structures and, mainly, the employed technique can promote important interests in the development of soft

matter photonic devices due to the extreme flexibility and ease of production of our technique and to the well known tuning features of the LC component.

Bibliography

[Agi 1994] K. Agi and al. Electron. Lett., vol. 30, page 2166, 1994. 2

[Apter 2007] B. Apter, Y. David, I. Baal-Zedaka and U. Efron. *Experimental study and computer simulation of ultra-small-pixel liquid crystal device.* In Proceedings of the 11th Meeting on Optical Engineering and Science (Israel, Tel Aviv), 2007. 117, 145

[Arns 1998] J. A. Arns, W. S. Colburn and S. C. Barden. Proc. SPIE, vol. 3355, page 866, 1998. 28

[Berger 1997] V. Berger, O. Gauthier-Lafaye and E. Costard. *Fabrication of a 2D photonic band gap by a holographic method.* Electr. Lett., vol. 33, pages 425–426, 1997. 3, 57, 61

[Born 1980] M. Born and E. Wolf. Principles of optics. Pergamon, 1980. 23, 76

[Braun 2006] P. V. Braun, S. A. Rinne and F. Garcia-Santamaria. *Introducing Defects in 3D Photonic Crystals:State of the Art.* Adv. Mater., vol. 18, page 2665, 2006. 55, 56

[Bunning 2000] T. J. Bunning and al. Annu. Rev. Mater. Sci., vol. 30, page 83, 2000. 3, 44, 46

[Burkov 1991] S. E. Burkov. *Structure model of the Al-Cu-Co decagonal quasicrystal.* Phys. Rev. Lett., vol. 67, page 614, 1991. 59

[Busch 1999] K. Busch and S. John. Phys. Rev. Lett., vol. 83, page 967, 1999. 3

[Campbell 2000] M. Campbell, D. N. Sharp, M. T. Harrison, R. G. Denning and A. J. Turberfield. *Fabrication of photonic crystals for the visible spectrum by holographic lithography.* Nature, vol. 404, pages 53–56, 2000. 3, 57, 61

[Caputo 2004] R. Caputo, L. De Sio, A. Veltri, C. Umeton and A. V. Sukhov. Opt. Lett., vol. 29, page 1261, 2004. 52

[Caputo 2005] R. Caputo, C. Umeton, A. Veltri, A.Sukhov and N. Tabiryan. *patent number WO20055006065.* 2005. 5, 45, 49, 52

[Chan 1998] Y. S. Chan, C. T. Chan and Z. Y. Liu. *Photonic band gaps in two-dimensional photonic quasicrystals.* Phys. Rev. Lett., vol. 80, pages 956–959, 1998. 2, 58, 60, 129

[Chan 2005] T. Y. M. Chan, O. Toader and S. John. *Photonic band gap templating using optical interference lithography.* Phys. Rev. E, vol. 71, page 046605, 2005. 54

[Cheng 1999] S. S. M. Cheng, L. Li, C. T. Chan and Z. Q. Zhang. *Defect and transmission properties of two-dimensional quasiperiodic photonic band-gap systems.* Phys. Rev. B, vol. 59, pages 4091–4099, 1999. 2, 58, 59

[Close 1969] D. H. Close and al. Appl. Phys. Lett., vol. 14, page 159, 1969. 3

[Curtis 2002] J. E. Curtis, B. A. Koss and D. G. Grier. *Dynamic holographic optical tweezers.* Opt. Comm., vol. 207, page 169, 2002. 5

[DalNegro 2003] L. DalNegro and al. Phys. Rev. Lett., vol. 90, page 055501, 2003. 4

[DalNegro 2004] L. DalNegro, M. Stolfi, Y. Yi, J. Michel, X. Duan, L. C. Kimerling, J. LeBlanc and J. Haavisto. *Photon band gap properties and omnidirectional reflectance in Si/SiO2 Thue-Morse quasicrystals.* Appl. Phys. Lett., vol. 84, pages 5186–5188, 2004. 62

[Davis 1999] J. A. Davis, D. M. Cottrell, J. Campos, M. J. Yzuel and I. Moreno. *Encoding amplitude information onto phase-only filters.* Appl. Opt., vol. 38, pages 5004–5013, 1999. 81, 94

[DeGennes 1993] P. G. DeGennes and J. Prost. The physics of liquid crystals. Clarendon Press, Oxford, 1993. 8, 12, 19

[DeSarkar 2003] M. DeSarkar, N. L. Gill, J. B. Whitehead and J. P. Crawford. Macromolecules, vol. 36, page 630, 2003. 48

[Domash 2000] L. Domash, G. Crawford, A. Ashmead, R. Smith, M. Popovich and J. Storey. Proc. SPIE, vol. 1, page 4107, 2000. 28

[Eldada 2004] L. Eldada. Rev. Sci. Instrum., vol. 75, page 575, 2004. 2

[Elser 1986] V. Elser. *The diffraction pattern of projected structures.* Acta Crystallogr., vol. 42, page 36, 1986. 59

[Escuti 2003] M. J. Escuti, J. Qi and G. P. Crawford. Opt. Lett., vol. 28, page 522, 2003. 66

[Fujiwara 1990] T. Fujiwara and T.Ogawa. Quasicrystals. Springer Verlag, Berlin, 1990. 4

[Gauthier 2004] R. C. Gauthier and A. Ivanov. *Production of quasicrystal template patterns using a dual beam multiple exposure technique.* Opt. Express, vol. 12, pages 990–1003, 2004. 3, 62

[Gauthier 2005] R. C. Gauthier and K. Mnaymneh. *Photonic band gap properties of 12-fold quasi-crystal determined through FDTD analysis.* Opt. Express, vol. 13, pages 1985–1998, 2005. 59, 129

[Gaylord 1985] T. K. Gaylord and M. G. Moharam. Proc. IEEE, vol. 73, page 894, 1985. 2, 26, 30, 42

[Gellermann 1994] W. Gellermann, M. Kohmoto, B. Sutherland and P. C. Taylor. Phys. Rev. Lett., vol. 72, page 633, 1994. 62

[Goodman 1996] J. W. Goodman. Introduction to fourier optics. New York: McGraw-Hill, 1996. 5, 28, 74, 77, 79, 88

[Gorkhali 2005] S. P. Gorkhali, J. Qi and G. P. Crawford. *Electrically switchable mesoscale Penrose quasicrystal structure.* Appl. Phys. Lett., vol. 86, pages 011110/1–3, 2005. 3, 61, 62, 68

[Gorkhali 2006] S. P. Gorkhali, J. Qi and G. P. Crawford. *Switchable quasicrystal structures with five-, seven-, and ninefold symmetries.* J. Opt. Soc. Am. B, vol. 23, pages 149–158, 2006. 3, 62, 112, 118, 145

[Grier 1998] D. G. Grier. Nature, vol. 393, page 621, 1998. 5, 73

[Grier 2003] D. G. Grier. *A revolution in optical manipulation.* Nature, vol. 424, page 810, 2003. 5, 74, 114

[Haist 1997] T. Haist, M. Schönleber and H. J. Tiziani. *Computer-generated holograms from 3D-objects written on twisted-nematic liquid crystal displays.* Opt. Comm., vol. 140, pages 299–308, 1997. 73, 81, 84, 93

[Hariharan 1984] P. Hariharan. Optical holography, principles, techniques and applications. Cambridge University Press, 1984. 28, 30, 74, 77

[Hase 2002] M. Hase, H. Miyazaki, M. Egashira, N. Sninya, K. M. Kojima and S. Uchida. *Isotropic photonic band gap and anisotropic structures in transmission spectra of two-dimensional fivefold and eightfold symmetric quasiperiodic photonic crystals.* Phys. Rev. B, vol. 66, pages 214205/1–7, 2002. 59, 129

[Hiett 2003] B. P. Hiett, D. H. Beckett, S. J. Cox, J. M. Generowicz, M Molinari and K. S. Thomas. *Photonic band gaps in 12-fold symmetric quasicrystals.* J. Materials Science, vol. 14, pages 413–416, 2003. 125

[Jesacher 2008] A. Jesacher, C. Maurer, A. Schwaighofer, S. Bernet and M. Ritsch-Marte. *Near-perfect hologram reconstruction with a spatial light modulator.* Opt. Express, vol. 16, page 2597, 2008. 81

[Jin 1999] C. Jin, B. Cheng, B. Man, Z. Li, D. Zhang, S. Ban and B. Sun. *Band gap and wave guiding effect in a quasiperiodic photonic crystal.* Appl. Phys. Lett., vol. 75, pages 1848–1850, 1999. 2, 58, 59

[Jin 2000] C. Jin, B. Cheng, B. Man, Z. Li and D. Zhang. *Twodimensional dodecagonal and decagonal quasiperiodic photonic crystals in the microwave region.* Phys. Rev. B, vol. 61, page 10762, 2000. 59

[Joannopoulos 1995] J. D. Joannopoulos, R. D. Meade and J. N. Winn. Photonic crystals molding the flow of light. Princeton University Press, 1995. 54, 55, 57

[Kaliteevski 2001] M. A. Kaliteevski, S. Brand, R. A. Abram, T. F. Krauss, P. Millar and R. M. De LaRue. *Diffraction and transmission of light in low-refractive index Penrose-tiled photonic quasicrystals.* J. Phys.: Condens. Matter, vol. 13, pages 10459–10470, 2001. 72

[Kang 2001] D. Kang, J. E. Maclennan, N. A. Clark, A. A. Zakhidov and R. H. Baughman. Phys. Rev. Lett., vol. 86, page 4052, 2001. 3

[Karimi 2007] E. Karimi, G. Zito, B. Piccirillo, L. Marrucci and E. Santamato. *Hypergeometric-Gaussian modes.* Opt. Lett., vol. 32, page 3053, 2007. 73

[Kogelnik 1969] H. Kogelnik. Bell Syst. Tech. J., vol. 48, page 2909, 1969. 32, 38, 39, 42

[Kogelnik 1972] H. Kogelnik and C. V. Shank. J. Appl. Phys., vol. 43, page 2327, 1972. 30

[Kohmoto 1987] M. Kohmoto, B. Sutherland and K. Iguchi. Phys. Rev. Lett., vol. 58, page 2436, 1987. 62

[Kolar 1994] M. Kolar. *High-resolution X-ray-diffraction spectra of Thue-Morse GaAs-AlAs heterostructures.* Phys. Rev. Lett., vol. 73, page 1307, 1994. 4, 62, 101

[Lee 2004] G. Lee, S. H. Song, C. H. Oh and P. S. Kim. *Arbitrary structuring of two-dimensional photonic crystals by use of phase-only Fourier gratings.* Opt. Lett., vol. 29, pages 2539–2541, 2004. 74

[Lee 2006] H. Y. Lee and G. Y. Nam. *Realization of ultrawide omnidirectional photonic band gap in multiple one-dimensional photonic crystals.* J. Appl. Phys., vol. 100, pages 083501/1–5, 2006. 4

[Lei 2007] H. Lei, J. Chen, G. Nouet, S. Feng, Q. Gong and X. Jiang. *Photonic band gap structures in the Thue-Morse lattice.* Phys. Rev B, vol. 75, pages 205109/1–10, 2007. 4

[Levine 1984] D. Levine and P.J. Steinhartdt. *Quasicrystals: a new class of ordered structures.* Phys. Rev. Lett., vol. 53, pages 2477–2480, 1984. 2, 58, 125

[Liesener 2000] J. Liesener, M. Reicherter, T. Haist and H. J. Tiziani. *Multi-functional optical tweezers using computer-generated holograms written on a liquid crystal display.* Opt. Comm., vol. 185, pages 77–82, 2000. 5, 73

[Macià 2006] E. Macià. *The role of aperiodic order in science and technology.* Rep. Prog. Phys., vol. 69, pages 397–441, 2006. 4, 62, 101, 102

[Mackay 1981] A. L. Mackay and D. N. Quinquangula. *On the pentagonal snowflake.* Sov. Phys. Crystallogr., vol. 26, page 517, 1981. 59

[Mao 2006] W. Mao, G. Liang, H. Zou, R. Zhang, H. Wang and Z. Zeng. *Design and fabrication of two-dimensional holographic photonic quasi crystals with high-order symmetries.* J. Opt. Soc. Am. B, vol. 23, pages 2046–2050, 2006. 62, 126, 145

[Matsui 2002] T. Matsui, R. Ozaki and K. Funamoto et al. Appl. Phys. Lett., vol. 81, page 3741, 2002. 2

[Mekis 1996] A. Mekis and al. Phys. Rev. Lett., vol. 77, page 3787, 1996. 2

[Montemezzani 1997] G. Montemezzani and M. Zgonik. Phys. Rev. E, vol. 55, page 1035, 1997. 43

[Moretti 2007] L. Moretti and V. Mocella. *Two-dimensional photonic aperiodic crystals based on Thue-Morse sequence.* Opt. Express, vol. 15, pages 15314–15323, 2007. 4, 62, 101, 117, 144

[Morthier 1997] G. Morthier and P. Vankwikelberge. Handbook of distributed feedback laser diodes. Artech House Publishers, Boston, 1997. 26, 30

[Natarajan 2003] L. V. Natarajan, C. K. Shepherd, D. M. Brandelik, R. L. Sutherland, S. Chandra, V. P. Tondiglia, D. Tomlin and T. J. Bunning. Chem. Mater., vol. 15, page 2477, 2003. 49

[Notomi 2004] M. Notomi, H. Suzuki, T. Tamamura and K. Edagawa. Phys. Rev. Lett., vol. 92, pages 123906 (1–4), 2004. 4

[Oxborrow 1993] M. Oxborrow and C. Henley. *Complete photonic bandgaps in 12-fold symmetric quasicrystals.* Phys. Rev. B, vol. 48, page 6966, 1993. 125

[Pogue 2000] R. T. Pogue, L. V. Natarajan, S. A. Siwecki, V. P. Tondiglia, R. L. Sutherland and T. J. Bunning. Polymer, vol. 41, page 733, 2000. 48

[Reicherter 1999] M. Reicherter, T. Haist, E. U. Wagemann and H. J. Tiziani. *Optical particle trapping with computer-generated holograms written on a liquid crystal display.* Opt. Lett., vol. 24, page 608, 1999. 5, 73

[Reshetnyak 1996] V. Y. Reshetnyak and al. J. Phys. D: Appl. Phys., vol. 29, pages 2459–2465, 1996. 26

[Romero-Vivas 2005] J. Romero-Vivas, D. N. Chigrin, A. V. Lavrinenko and C. M. Sotomayor Torres. *Resonant add-drop filter based on a photonic quasicrystal.* Opt. Express, vol. 13, pages 826–835, 2005. 126, 127

[Sakhno 2004] O. Sakhno, S. Slussarenko and J. Stumpe. *POLIPHEM: new type of nanoscale polymer-LC-switchable photonic devices.* Organic Holographic Materials and Applications II-Proceedings of the SPIE, vol. 5521, pages 38–45, 2004. 45, 49, 52, 53

[Serbin 2006] J. Serbin and M. Gu. *Experimental Evidence for Superprism Effects in Three-Dimensional Polymer Photonic Crystals.* Adv. Mater., vol. 18, pages 221–224, 2006. 53

[Shechtman 1984] D. Shechtman, I. Blech, D. Gratias, and J. W. Chan. *Metallic phase with long-range orientational order and no translational symmetry.* Phys. Rev. Lett., vol. 53, page 1951, 1984. 58

[Sigalas 1997] M. M. Sigalas and al. Microw. Opt. Technol. Lett., vol. 15, page 153, 1997. 2

[Simoni 1997] F. Simoni. Non linear optical properties of liquid crystals and polymer dispersed liquid crystals. World Scientific, River Edge, NJ, 1997. 24, 44

[Sinclair 2004] G. Sinclair, J. Leach, P. Jordan, G. Gibson, E. Yao, Z. J. Laczik, M. J. Padgett and J. Courtial. *Interactive application in holographic optical tweezers of a multi-plane Gerchberg-Saxton algorithm for three-dimensional light shaping.* Opt. Express, vol. 12, page 1665, 2004. 73, 81

[Socolar 1989] J. E. S. Socolar. *Simple octagonal and dodecagonal quasicrystals.* Phys. Rev. B, vol. 39, pages 10519–10551, 1989. 126

[Soifer 2002] V. A. Soifer. Methods for computer design of diffractive optical elements. New York: John Wiley and Sons, Inc., 2002. 74, 77, 79, 82

[Stadnik 1999] Z. M. Stadnik. Physical properties of quasicrystals. New York: Springer, 1999. 2, 58

[Steinhardt 1987] P.J. Steinhardt and S. Ostlund. The physics of quasicrystals. River Edge, NJ: Word Scientific, 1987. 2, 58

[Stephens 1986] P. W. Stephens and A. I. Goldman. *Sharp diffraction maxima from an icosahedral glass.* Phys. Rev. Lett., vol. 56, page 1168, 1986. 58

[Strangi 2005] G. Strangi, V. Barna and R. Caputo et al. Phys Rev. Lett., vol. 94, page 063903, 2005. 2

[Suck 2002] J. B. Suck, M. Schreiber and P. Haussler. Quasicrystals. Springer, Berlin, 2002. 60

[Sullivan 2000] D. M. Sullivan. Electromagnetic simulation using the fdtd method. Wiley-IEEE Press, New York, 2000. 129

[Sutherland 1993] R. L. Sutherland, L .V. Natarajan, V. P. Tondiglia and T. J. Bunning. *Bragg gratings in an acrylate polymer consisting of periodic polymer-dispersed liquid-crystal planes.* Chem. Mater., vol. 5, pages 1533–1538, 1993. 3, 24, 44

[Sutherland 1994] R. L. Sutherland, L .V. Natarajan, V. P. Tondiglia, T. J. Bunning and W. W. Adams. Appl. Phys. Lett., vol. 64, page 1074, 1994. 5

[Veltri 2004] A. Veltri and al. Appl. Phys. Lett., vol. 84, page 3492, 2004. 44

[Verlag 2009] Verlag. Photonic crystals theory, applications and fabrication. Wiley Series in Pure and Applied Optics. Wiley, New York, 2009. 54

[Wang 2003] X. Wang, C. Y. Ng, W. Y. Tam, C. T. Chan and P. Sheng. *Large-area two-dimensional mesoscale quasicrystals.* Adv. Mater., vol. 15, pages 1526–1528, 2003. 3, 59, 61, 68

[Wang 2006] X. Wang, J. Xu, J. C. W. Lee, Y. K. Pang, W. Y. Tam, C. T. Chan and P. Sheng. *Realization of optical periodic quasicrystals using holographic lithography.* Appl. Phys. Lett., vol. 88, pages 051901/1–3, 2006. 3, 62, 68

[Yablonovitch 1987] E. Yablonovitch. Phys. Rev. Lett., vol. 58, page 2059, 1987. 1, 54

[Yang 2006] Y. Yang, S. Zhang and G. P. Wang. *Fabrication of two-dimensional metallodielectric quasicrystals by single-beam holography.* Appl. Phys. Lett., vol. 88, pages 251104/1–3, 2006. 3, 61, 123

[Yoshino 1999] K. Yoshino, Y. Shimoda, Y. Kawagishi, K. Nakayama and M. Ozaki. Appl. Phys. Lett., vol. 75, page 932, 1999. 3

[Zhang 1999a] D. Zhang and al. Appl. Phys. Lett., vol. 75, page 1848, 1999. 2

[Zhang 1999b] D. Zhang and al. Phys. Rev. B, vol. 59, page 4091, 1999. 2

[Zhang 2001] X. Zhang, Z. Q. Zhang and C. T. Chan. *Absolute photonic band gaps in 12-fold symmetric photonic quasicrystals.* Phys. Rev. B, vol. 63, pages 081105/1–4, 2001. 2, 58

[Zhou 2007] G. Zhou and M. Gu. *Photonic band gaps and planar cavity of two-dimensional eigthfold symmetric void-channel photonic quasicrystal.* Appl. Phys. Lett., vol. 90, pages 201111/1–3, 2007. 62, 126

[Zito 2007] G. Zito, B. Piccirillo, E. Santamato, A. Marino, V. Tkachenko and G. Abbate. *Computer-generated holographic gratings in soft matter.* Mol. Cryst. Liq. Cryst., vol. 465, pages 371–378, 2007. 4, 73

[Zito 2008] G. Zito, B. Piccirillo, E. Santamato, A. Marino, V. Tkachenko and G. Abbate. *Two-dimensional photonic quasicrystals by single beam computer-generated holography.* Opt. Express, vol. 16, pages 5164–5170, 2008. 4, 73, 101

[Zoorob 2000] M. E. Zoorob, M. D. B. Charlton, G. J. Parker, J. J. Baumberg and M. C. Netti. *Complete photonic bandgaps in 12-fold symmetric quasicrystals.* Nature, vol. 404, pages 740–743, 2000. 2, 59, 60, 125